Microglia and Myelin:

Improved Tools and Molecular Interactions

by

Tobias Kaiser

Submitted to the Department of Brain and Cognitive Sciences

in partial fulfillment of the requirements for the degree of

PhD in Brain and Cognitive Sciences

at the

MASSACHUSETTS INSTITUTE OF TECHNOLOGY

September 2021

Author: . . . . . .

Department of Brain and Cognitive Sciences

September, 2021

Certified by: . . . . . .

Dr. Guoping Feng

Poitras Professor of Neuroscience

Thesis Supervisor

Accepted by: . . . . . .

Dr. Rebecca Saxe

Associate Head, Department of Brain and Cognitive Sciences

Microglia and Myelin: Improved Tools and Molecular Interactions

by

Tobias Kaiser

Submitted to the Department of Brain and Cognitive Sciences

on September 10, 2021, in partial fulfillment of the requirements for the degree of

PhD in Brain and Cognitive Sciences

Abstract

Myelination of axons evolved in vertebrates to promote signal transduction and the development of a compact and energy-efficient nervous system. Myelin development and homeostasis are critical for normal function and impairment of myelin is associated with sensory, motor, and cognitive dysfunction. While it has long been understood that oligodendrocytes produce myelin in the CNS, more recent studies also implicate additional cell types including microglia as providers of important molecular cues in myelination. Studies dissecting these cues have made great strides, yet the functions of many candidate molecular mediators remain incompletely defined, at least in part due to the scarcity of suitable tools. The goal of my thesis was threefold: (1) creating and supplying the research community with much needed improved genetic tools to study the role of microglia, (2) developing analysis tools to facilitate the analysis of white-matter ultrastructure, and (3) defining the role of a candidate molecular mediator, IgG, as well as its receptor, in white-matter development. In Chapter 1, I report the generation and characterization of novel transgenic mouse lines for the labeling and the inducible genetic manipulation of microglia. Harnessing the microglia-specific *Tmem119* locus and CRISPR/Cas, I engineered knock-in mice expressing EGFP or CreERT2 and show that these lines are highly specific in discerning microglia from other closely related myeloid cells. Extending this work, in Chapter 2, I present evidence for the generation of a highly efficient and specific constitutively active Cre line leveraging the *Fcrls* locus. Most notably, flow cytometric analysis shows that this line completely spares monocytes and other white blood cells. Complementing *Tmem119-EGFP* and *Tmem119-CreERT2* mice that have already been adopted by hundreds of labs*, Fcrls-Cre* mice will enable genetic studies of microglia with improved specificity. In Chapter 3, I report the development and characterization of MyelTracer, an easy-to-install software suite made available to the research community for the quantification of myelin *g*-ratio, a key metric in studies of myelin morphology. Finally, in Chapter 4, I present evidence for the occurrence of maternally derived IgG on microglia in the postnatal brain. Using a genetic mouse model to study its functional relevance, I show that brains of mice lacking IgG postnatally harbor fewer myelinating oligodendrocytes and thinner axons in the corpus callosum. Further, using both newly generated conditional *Fcer1g* (part of IgG receptor) and existing constitutive *Fcer1g* knockout models, I show that the effect of IgG is not mediated through the canonical IgG-Fc receptor pathway. Independent of Fc receptors, IgG appears to be required for the function of a subset of microglia that occurs in white-matter tracts postnatally and is required for normal white-matter development. Overall, the work presented in this thesis resulted in the generation of several much-needed tools for the research community, and it reveals molecular insights into the role of IgG in the developing brain.

Thesis Supervisor: Dr. Guoping Feng
Title: Poitras Professor of Neuroscience

Contents

INTRODUCTION **8**

CHAPTER 1: DEVELOPMENT OF TRANSGENIC MICE TO LABEL AND MANIPULATE MICROGLIA **29**

1.1 ABSTRACT 30
1.2 INTRODUCTION 31
1.3 RESULTS 33
1.4 DISCUSSION 49

CHAPTER 2: DEVELOPMENT OF A CONSTITUTIVELY ACTIVE CRE LINE FOR THE MANIPULATION OF MICROGLIA **54**

2.1 ABSTRACT 55
2.2 INTRODUCTION 56
2.3 RESULTS 58
2.4 DISCUSSION 69

CHAPTER 3: DEVELOPMENT OF AN EASY-TO-USE SOFTWARE FOR THE QUANTIFICATION OF MYELIN *G*-RATIO **73**

3.1 ABSTRACT 74
3.2 INTRODUCTION 75
3.3 RESULTS 78
3.4 DISCUSSION 88

CHAPTER 4: PROBING THE ROLE OF IGG AND MICROGLIAL FCER1G IN WHITE-MATTER DEVELOPMENT **91**

4.1 ABSTRACT 92
4.2 INTRODUCTION 93
4.3 RESULTS 95
4.4 DISCUSSION 126

CONCLUSIONS, LIMITATIONS, AND FUTURE DIRECTIONS **133**

MATERIALS AND METHODS **138**

REFERENCES **159**

Acknowledgements

This thesis is the result of great teamwork with many friends and colleagues, guided by exceptional mentors, fueled by the joy of discovering and engineering things, and anchored in a foundation nurtured by many individuals over the years.

I am truly grateful to Guoping for taking me on as a visiting student and for backing my desire to continue my work as a graduate student at MIT. When looking at Guoping as a scientist and mentor, I feel inspired in so many ways: 1) he is incredibly welcoming and makes everyone feel at home as part of the lab family. Recognizing that people seek a sense of belonging after coming from across all over the US and the world, Guoping opens his home to everyone on Thanksgiving each year, which have been a wonderful get-togethers to form stronger friendships. On other occasions, he has invited me and others to go skiing with him and his son on Sundays. No matter which activity, he always makes it feel like there are no barriers and everyone belongs to one big family. 2) Guoping is incredibly curious. Looking at his contributions, it is apparent that there is an unwavering and incredibly logical pursuit of new therapeutics in autism, yet he is also always willing to venture out to test more outside-the-box ideas. If he thinks something is interesting and worthwhile pursuing, he will go after it and make it happen. 3) Guoping is the most supportive mentor I have ever met, while also always being extremely honest. In countless instances, he has asked what he can do for me to bring the projects to the next stage rather than tell me what he needs me to do. And throughout my time in his lab, I always felt like he was looking out for me. In an instance I recall well, I approached him to get his okay for becoming a graduate resident advisor on campus. He laid out the reasons why he thought it might not be the best idea but listened to my reasons for wanting to do it. Subsequently, he went out of his way to provide the crucial support without which I could have not done it. I know it would have been much easier for him to just not provide that exceptional extra support, but that's not who he is – he deeply cares and wants to help people succeed given the choices they make for themselves. Thank you for that, Guoping.

Along the way, many mentors helped me get to this point. First and foremost, I would like to thank my thesis committee members Troy Littleton, Mriganka Sur, and Gloria Choi for their invaluable feedback during the past years. I would also like to thank my undergraduate mentor Said Hashemolhosseini at the University of Nuremberg without whom I would have never made it to MIT. Countless times, Said sat with me on the bench side-by-side to teach me how to pipet accurately, how to dissect tissues, and how to culture cells. Most importantly he taught me a lot about the scientific method. He also never hesitated to throw his weight around to support my plans and even made the introduction to Guoping. Similarly, I loved learning from Teja Groemer who taught me how to push the last 5% on a project and Thomas Pucadyil who literally turned my rotation report draft from black font into 100% pure red font, aka tracked edits, only to spend many additional hours going over his edits with me in detail and thus making me a better scientific writer. At MIT, my experience would have not been the same if it weren't for Yang Zhou who was my postdoctoral mentor upon my arrival. Working with Yang was insanely fun, no matter how late at night. He's both a stickler about the experiment and a super funny guy, and whatever he does, he does to perfection. Yang is just an incredible mentor and I feel excited for all the lucky trainees who will be working with him in his lab. Along with Yang, Patrícia Monteiro taught me a lot of electrophysiology and instilled her detail-oriented working style into me. In the Feng lab, a very special thing is the willingness of senior researchers to take time out of their day and share their expertise. Specifically, I would like to acknowledge Boaz Barak, Jonathan Wilde, Tomomi Aida,

Menglong Zhang, Martin Wienisch, Dongqing Wang, Ryan Kast, and Sasha Krol. A special thanks goes to Minqing Jiang who has been a wonderful collaborator on my projects. Minqing's perseverance and openness to engage in a good scientific debate has always pushed me to think harder, and I'll sorely miss our excursions to the electron microscopy core facility. In addition to mentors, I thank all my wonderful colleagues in the Feng lab for being so helpful every single day. I couldn't have done it without you all.

During all these years, I didn't only get to enjoy learning from my mentors, but I also had the great privilege to take on mentees and teach. One of the truly special things at MIT is the UROP program and working with my students Madison, Liang, Ohyoon, and Harrison was an extremely fulfilling experience. Collaborating with them on a variety of projects and seeing them grow was one of my favorite parts of grad school and I'm really looking forward to following their exciting careers in science and medicine.

The most fulfilling parts of my life are often the friendships and connections I form, and I was fortunate to make great friends during the past few years at MIT. From Gijs and Thomas who I met just after arriving, to Patrícia, David, Paresh, Matt, Mike, Jon, Joe, Nikki, and Vamsi, life wouldn't be the same without you guys. I also cherish all the friends from the sailing club, Masskiting kitesurfing community, and the students of Next House who I met during my time as a GRA – thank you all.

Despite doing biomedical research and thinking about new therapeutics, it's often easy to forget our own health. Toward the end of this thesis research, I was painfully reminded of how fragile our health can be and how essential good health is to really anything we're doing when I experienced complications from surgery on a shattered heel. I want to thank my physician friends David, Claudius, Howard, Mora, Richard, and Tom for keeping a close eye on me and for providing invaluable advice. Without you guys I could have not finished the thesis.

I'd like to thank my family, including my parents, grandparents, my brother, and Silvinha who provided support and encouragement during this process. Finally, I thank Lilin, my partner, for being inspiring and kind, for giving me strength to keep going when I felt down, and for always believing in what I do.

Introduction

Myelin in the CNS of Vertebrates

Myelination of axons and resulting white-matter tracts evolved in vertebrates as a significant step for a compact and energy-efficient nervous system (Nave, 2010). Insulating myelin sheaths around axons enable saltatory propagation of action potentials along axons, which results in high conduction velocity and millisecond precision in otherwise slow thin axons as well as reduced ATP consumption due to the limitation of action potentials and ion currents to only about 0.5% of axonal surface. As such, it is not surprising that the brain relies on intact myelin and defects in myelination result in severe motor-sensory and cognitive dysfunction.

Myelin is a multilayered sheath consisting of about two thirds lipids and one third proteins (Cammer and Norton, 1976). To produce this sheath, oligodendrocytes extend their membranes and spirally wrap them around axons (Geren and Raskind, 1953). This process is highly regulated by axon-oligodendroglia interactions, but also signaling between oligodendroglia and other glia. In the following, I will briefly review the developmental time course of myelination and molecular composition of myelin in mice, as the model species for this study. I will further touch upon impairments of myelin and how different glia play a role in myelination before expanding on the significance of microglia in myelination. For microglia, expression of proteins that may play a role in myelination will be discussed.

Developmental Time Course of Myelination and Myelin Composition in Mice

Oligodendrocytes are the myelin producing cells in the CNS. During development, subventricular cells in the brain and spinal cord initially generate committed bipolar $NG2^{+}$

oligodendrocyte precursor cells (OPCs), which further divide and spread throughout the brain. Once at their target location, OPCs differentiate into postmitotic, multipolar pre-myelinating oligodendrocytes that express the proteins cyclic-nucleotide phosphodiesterase (CNP) and myelin-associated glycoprotein (MAG). Subsequently, premyelinating oligodendrocytes receive cues from their environment and mature further. At this stage, they express classic isoforms of myelin basic protein (MBP) and proteolipid protein (PLP), and myelinate axons (Emery, 2010; Harauz and Boggs, 2013). In the following, the developmental onset of expression and molecular insights regarding this process and the molecular mediators will be discussed.

In the mouse, myelin is largely produced postnatally in a caudal to cranial gradient, starting in the spinal cord and brain stem. Based on studies using in-situ hybridization and MBP-reporter mice, mature olgiodendrocytes produce MBP and PLP as early as postnatal day 3 (P3) in the medulla and pons. By P6 and P9, MBP-expressing cells begin to appear in the cerebellum and corpus callosum, respectively (Shiota et al., 1989; Foran and Peterson, 1992; Mathisen et al., 1993). According to Shioto and colleagues, the number of PLP-expressing oligodendrocytes plateaus in the cerebellum and the forebrain at P18 and P30, respectively, reflecting the gradual maturation of myelination along the caudo-rostral gradient.

Besides myelin protein and transcript expression, myelin maturation can be assessed with electron microscopy. Vincze and colleagues examined the corpus callosum at different time points and found first ultrastructural signs of myelination around postnatal day 10 (Vincze et al., 2008). By P14, oligodendrocytes had formed more myelin sheaths that were loosely packed and from P14 onwards, oligodendrocytes increased the number of myelin sheaths. At the latest time point examined, P28, production of myelin sheaths had still not reached maturation, as thick and loosely packed sheaths coexisted. This appears to be slightly different for other regions. In the cerebellum,

ultrastructural evidence indicates that many fibers are already wrapped with myelin in this region at P11 (Zonouzi et al., 2015), which is in line with the earlier expression of PLP and MBP.

Mature Oligodendrocytes produce several proteins that are critical for the formation of myelin. The function of many of these proteins that have been identified with proteomics is unknown. However, MBP, PLP, MAG, and MOG, which are the most abundant and best-known myelin proteins are well characterized. MBP is cytoplasmic and PLP is a tetraspan transmembrane protein. Together they are essential for myelin compaction. The functional significance of PLP is demonstrated by findings of progressive myelin degeneration in PLP null mice. MBP, in contrast, appears to be important for adhesion to cytosolic surfaces and initial myelination, as shiverer mice lacking MBP almost completely lack myelin, and display incomplete compaction of residual myelin and reduced axon calibers (Moscarello, 1997). MAG is a single transmembrane protein that also appears to regulate axon size, yet via a different mechanism, as MAG-deficient mice display reduced axon calibers while being fully myelinated. The role of MOG is currently unknown, and MOG-deficient mice myelinate the brain normally. Some evidence indicates that MOG might be involved in axonal sprouting. Another important oligodendrocyte-specific protein is CNP. Like PLP, CNP deletion does not interfere with myelin formation, but results in degeneration of the axon after apparently normal initial development (Nave, 2010).

Disorders of Impaired Myelin and Implications of Different Glia in Myelination

Several disorders characterized by significant white-matter pathology have been described including multiple sclerosis (MS), leukodystrophies, and Nasu-Hakola disorder. Generally, the pathology of these disorders does not only involve oligodendrocytes, but interactions of oligodendrocytes with immune cells, axons, and other glia.

The best-known disorder involving myelin is multiple sclerosis (MS). In MS, autoimmune processes involving autoreactive $CD4^+$ and infiltrating activated $CD8^+$ cells cause demyelinating lesions in the white matter that develop into focal edemas, which impair axon conductance. Over time, this relapsing-remitting stage of MS characterized by focal destruction of myelin sheaths and oligodendrocytes turns into an advanced phase of progressive MS. At this advanced stage, excessive demyelination and sodium channel reorganization in the axon perturb the axonal energy balance to a degree that causes destruction of the axon and long-term disability (Trapp and Nave, 2008; Trapp and Stys, 2009).

A disorder affecting myelin through oligodendrocytes directly is the leukodystrophy Palizaeus-Merzbacher disease (PMD), a hypomyelinating disorder, which covers manifestations from pure spastic paraplegia to early lethality (Garbern, 2007). In PMD, PLP1 mutations result in misfolding of the protein, unfolded protein response, and excessive oligodendrocyte apoptosis.

Further clinical evidence from two other leukodystrophies shows that astrocytes are important for myelination. First, mutations in the oligodendroglial gap junction protein Connexin47 (Cx47), which forms gap junction with astrocytic connexins, result in the developmental disorder hypomyelinating leukodystrophy 2 (HLD2). Second, mutations in the astrocyte protein glial fibrillary acidic protein (GFAP) cause Alexander's disease (Brenner et al., 2001). In mice, GFAP deletion results in poor vascularization of the white matter, blood-brain barrier defects, and myelin abnormalities (Liedtke et al., 1996).

Microglia are clinically implicated in white-matter disorders through hereditary diffuse leukoencephalopathy with spheroids (HDLS) with spheroids and Nasu-Hakola disease. HDLS is caused by mutations in the tyrosine-kinase domain of CSF-1R, which is predominantly expressed by microglia in the brain. Through yet incompletely understood mechanisms, these CSF-1R

mutations cause gliosis, myelin loss, autofluorescent lipid-laden macrophages, axonal spheroids, and morphological abnormalities in neurons (Rademakers et al., 2012). Nasu-Hakola disease is caused by mutations in either Triggering receptor expressed in myeloid cells 2 (Trem2) or its accessory protein TYRO protein tyrosine kinase binding protein TYROBP, formerly known as DAP12 (Paloneva et al., 2000, 2002). In the brain, both Trem2 and DAP12 are exclusively expressed in myeloid lineage cells such as microglia (Paloneva et al., 2002; Zhang et al., 2014; Vanlandewijck et al., 2018). Clinically, the disorder is characterized by psychiatric symptoms encompassing memory impairment, loss of social inhibitions, and frigidity, starting in the fourth decade, which progressively resemble those of Alzheimer's disease at later stages. Currently, it is not fully understood how Trem2 and TYROBP mechanistically relate to the severe destruction of white matter observed in the disorder. One probably scenario involves impaired lipid-sensing through microglial Trem2 (Wang et al., 2015) and reduced Trem2-mediated phagocytosis (Kleinberger et al., 2014; Poliani et al., 2015) of myelin and oligodendrocytes as an important mechanism in myelin maintenance.

Together, these genetic data and molecular studies from MS, Palizaeus-Merzbacher disease, hypomyelinating leukodystrophy 2, Alexander's disease, hereditary diffuse leukoencephalopathy, and Nasu-Hakola disease implicate both cell-autonomous mechanisms and cell-cell interactions with other glia in myelin development and maintenance. In the following section, I will elaborate more on insights regarding microglia involvement in myelination.

Microglia in Myelination and White-matter Tract Development

The genetic mutations underlying hereditary diffuse leukeencephalopathy with spheroids (HDLS) and Nasu-Hakola disease strongly implicate microglia in these diseases characterized by

severe white-matter abnormalities. These and other findings from microglia activation in MS lesions as well as significant enrichment of microglia at white-matter tracts during development prompted a wave of recent preclinical research into the function of microglia in myelination. The following paragraph will briefly summarize the main findings and transition to microglial candidate genes that might be required for myelination, which currently remain a knowledge gap.

During development, the brain significantly reorganizes its white-matter tracts. Some of the most striking evidence for this stems from early studies in kittens, rodents and non-human primates, where several labs conducted tracer, electrophysiological, and electron microscopy studies showing axon elimination in the corpus callosum shortly before myelination. Using tracers, these labs found that several contralateral regions were labeled in newborn animals, but not adults. In line with this, stereotactic counting in electron microscopy show that a remarkable 70% of callosal axons in cats and monkeys that are present in newborns are eliminated by adulthood (Koppel and Innocenti, 1983; LaMantia and Rakic, 1990). Further examination showed that the elimination of callosal axons coincides with the appearance of transitory macrophages (also called gitter cells and ameboid microglia) in the white matter that are filled with axonal material (Innocenti et al., 1983). More than 30 years later, Prinz and colleagues experimentally ablated these activated, phagocytic microglia in mice genetically or by administering a drug that selectively depletes microglia during this period of callosal axon elimination and myelin formation (Hagemeyer et al., 2017). Mice lacking microglia during the first postnatal week showed significantly reduced numbers of oligodendrocyte progenitor cells (OPCs) and fewer mature oligodendrocytes in the corpus callosum at postnatal day 20. Interestingly, at this stage, OPC numbers were normal in both the cerebellar and callosal white matter, and only mature oligodendrocytes were impaired. On the molecular level, mice lacking microglia during the early

postnatal period displayed reduced expression of major myelin protein on the transcript and protein level at P20. In another study, Pont-Lezica and coworkers eliminated total microglia by using PU.1 knockout mice to study the role of microglia in corpus callosum tract formation (Pont-Lezica et al., 2014). Upon depletion of microglia, defasciculation of the dorsal tract of the corpus callosum was apparent. Together, these two studies demonstrate the requirement of microglia for normal corpus callosum development.

One of the mechanisms through which microglia regulate myelination is secretion of trophic factors such as IGF1, TGM2 and Activin-A (Miron et al., 2013; Wlodarczyk et al., 2017; Giera et al., 2018). IGF1 is required for proper myelination and microglia are the major IGF1-producing cell type in the brain (Beck et al., 1995; Chesik et al., 2008; Zhang et al., 2014; Saunders et al., 2018; Vanlandewijck et al., 2018). Amongst microglia, a subset of CD11c-positive microglia dramatically expands during the first week of development in white-matter tracts, where they produce IGF1 (Wlodarczyk et al., 2014, 2017). IGF1 derived from these cells is required for myelination, as selective experimental depletion of IGF1 in CD11c+ cells results in reduced myelin transcript expression and thinner myelin sheaths at postnatal day 21.

Another secreted microglial molecule that mediates myelination is transglutaminase-2, short TG2 (Giera et al., 2018). Microglia produce TG2, which induces oligodendrocyte precursor cells (OPCs) proliferation upon binding to its receptor ADGR1. Mice lacking TG2 display reduced numbers of PLP-positive oligodendrocytes at P14 and P28 and fewer myelinated axons in the corpus callosum at P28, showing that TG2 is required for normal myelination. In addition to its role in developmental myelinogensis, TG2 appears to be a potent stimulator of myelination in adulthood, as TG2 administration improves remyelination in two mouse models of demyelination.

A third factor microglia release to influence myelination is activin-A (Miron et al., 2013). Microglia that display a regenerative phenotype several days after experimentally induced white-matter lesions secrete activin-A, which binds to its receptor on OPCs. Upon binding, activin-A enhances oligodendrocyte differentiation *in vitro* and *ex vivo* in organotypic cerebellar slice cultures. Together, these findings demonstrate that microglial activin-A has myelinogenic potential.

The factors mentioned above provide some examples of how microglia play a role in myelination, yet the precise involvement of microglia in myelination remains incompletely defined and there is a significant need to better understand their molecular mediators. Additional microglial candidate molecules in myelination are Fc-receptors (FcRs). According to RNA sequencing data, FcRs are amongst the most highly expressed genes in microglia (Zhang et al., 2014; Saunders et al., 2018; Vanlandewijck et al., 2018; Hammond et al., 2019; Li et al., 2019) and deletion of *Fcer1g*, which encodes a required signaling molecule common to all activating FcRs, results in significant impairment of myelination (Nakahara et al., 2003).

Though there are several excellent general reviews of FcRs and their ligand Immunoglobulin G (IgG) (Nimmerjahn and Ravetch, 2008; Vidarsson et al., 2014), each focus largely on peripheral cells and processes at the adult stage. The following sections briefly review immunoglobulins and their maternofetal transport, as well as Fc-receptors and their expression in microglia.

Immunoglobulin (IgG), Maternofetal IgG Transport, and IgG in the Brain

Immunoglobulins are a class of soluble proteins produced by B-cells. Most broadly, immunoglobulins can be classified according to the constant region (Fc) of their heavy chain into

IgM (mu chain), IgA (alpha chain), IgD (delta chain), IgE (epsilon chain), and IgG (gamma chain), which can be further sub-classified into IgG1, IgG2a, IgG2b and IgG3. IgM is the first immunoglobulin produced by mature B-cells, which switch the IgM heavy chain constant region to another heavy chain subtype when activated by antigen (Nimmerjahn and Ravetch, 2010). This switch evolved to allow for different functional downstream consequences including cytotoxicity, phagocytosis, and release of inflammatory mediators (Ravetch and Bolland, 2001). Upstream, the switching to a particular subclass is influenced by several factors, especially the cytokine environment. Interleukin 4 (IL-4) polarizes B-cells towards IgG1 and IgE, TGF-beta induces IgG2b and IgA subtypes, Interferon gamma (IFNg) induces IgG2a, IgG2b and IgG3 (Finkelman et al., 1990). Besides the cytokine environment, the nature of the antigen induces specific IgG subclasses. Protein antigens stimulate thymus-dependent responses characterized by IgG1, IgG2a, and IgG2b, whereas carbohydrate antigens induce thymus-independent responses mediated by IgG3.

During development, there is an early burst of IgG and IgM synthesis in the spleen between 10-18 weeks of gestation in humans (Holt and Jones, 2000). Following this initial burst of fetal IgG, the fetus does essentially not produce any IgG, but levels of maternally-derived IgG first slowly and then rapidly increase up to 22 weeks and birth, respectively (Holt and Jones, 2000). This active IgG transport is mediated via the neonatal Fc-receptor (FcRn) that shuttles IgG from the maternal circulation across syncythiotrophoblast cells to fetal capillaries in the placenta (Roopenian and Akilesh, 2007). Similarly, mice also transport large amounts of IgG to their offspring through an active transport mechanism that increases its rate between 11 and 15 days of gestation (Morphis and Gitlin, 1970). In mice and other rodents however, FcRn mostly mediates

intestinal uptake of IgG, which occurs postnatally upon ingestion of milk (Roopenian and Akilesh, 2007).

Once released by B-cells in mature animals or taken up from maternal sources in pre- and postnatal mice, serum IgG circulates throughout the body. To date, the question whether IgGs penetrate the brain remains a matter of debate. Much of the early work used dye-based methods as a proxy of blood-brain barrier permeability for large molecules like IgG. These dyes bind to albumin in the circulation and thus reflect the penetration of albumin to the brain, which makes these methods essentially agnostic to potential selective IgG transport mechanisms. More recent studies employing injections IgG-conjugates to the pregnant dam and infrared imaging of the tagged IgG suggest that IgG penetration to the developing brain sharply drops around embryonic days 16.5-17.5 (Braniste et al., 2014; Kowal et al., 2015). Beyond these studies centered on blood-brain barrier permeability to IgG, several studies directly investigated IgG occurrence in the brain. In developing mice and rats, IgG localizes to cells in the cortical subplate region, retina, and cerebellar white matter at E18 and the first postnatal days (Fairén et al., 1992; Upender et al., 1997). Furthermore, Weiner and colleagues detected the IgG light chain via immunoblotting and immunohistochemistry at embryonic day 14, 16, as well as postnatal day 1, and showed that it is derived from the pregnant dam (Weiner and Chun, 1997). At the adult stage, IgG appears to occur in the brain at significantly lower levels, where it localizes to microglia (Upender et al., 1997; Hazama et al., 2005). These IgGs might be derived from the periphery or local production in the meninges and choroid plexus (Hazama et al., 2005). Together, these studies demonstrate maternofetal transport of IgG and penetration of IgG to the developing and possibly adult brain. In either case, the target protein or carbohydrate antigen of IgGs and their function remain unknown.

Fc-receptors

Reviewing Fc-receptors in-depth is beyond the scope of this survey and done excellently elsewhere (Nimmerjahn and Ravetch, 2008). Instead, this section will briefly review Fc-receptor biology and focus on insights from cell-profiling studies on Fc-receptor expression in microglia.

Fc-receptors are expressed on cells of the innate immune system and derive their name from their ability to bind to the constant fragment (Fc) of immunoglobulins. As such, they bridge the adaptive and innate immune system and mediate cellular responses encompassing cytokine secretion, phagocytosis, and cellular cytotoxicity. In mice, there are three activating Fc-receptors (Fcgr1, Fcgr3, and Fcgr4), one inhibiting Fc-receptor (Fcgr2b), and the neonatal Fc-receptor (FcRn) discussed above (Nimmerjahn and Ravetch, 2005; Schwab and Nimmerjahn, 2013). All activating Fc-receptors consist of an extracellular ligand-binding alpha chain and a dimer of signal-transducing intracellular gamma chains with immunoreceptor tyrosine-based activation motif (ITAM). In contrast, the inhibitory Fcgr2b only consist of an alpha chain, which is both ligand-binding and signal-transducing due to its immunoreceptor tyrosine-based inhibition motif (ITIM). Fcgr1 is the only high affinity receptor activated by monomeric IgG, whereas Fcgr3, Fcgr4 and Fcgr2b are activated through cross-linking by IgG-immune complexes. Furthermore, different FcRs display different affinities for IgGs of the different subclasses, which results in different functional outcomes involving different degrees of activation and inhibition represented in the A/I ratio. For instance, IgG2a binds to Fcgr1 and Fcgr4 with high affinity and is the most activating IgG with an A/I ratio of 70. IgG2b binds preferentially to the activating receptor Fcgr4 with an A/I ratio of 7. This lower A/I ratio makes IgG2b function highly dependent on the expression and relative activation of the inhibitory receptor Fcgr2b. A third member of the IgG subclass, IgG1 depends on Fcgr3 and exhibits a low A/I ratio of 0.1 (Nimmerjahn and Ravetch, 2005). In

summary, depending on the receptor activating, the different IgGs display different strength of activation with IgG2a being the strongest followed by IgG2b and IgG1 (Clynes and Ravetch, 1995).

Microglia highly express all FcRs based on several cell-profiling studies (Zhang et al., 2014; Bennett et al., 2016; Saunders et al., 2018; Hammond et al., 2019; Li et al., 2019). Zhang and colleagues sequenced enzymatically dissociated and CD45-sorted microglia from brains at postnatal day 7 and found high expression of FcR genes (Zhang et al., 2014). Bennett and colleagues took a similar approach, but dounce-homogenized and sorted tissue (CD45lo CD11b^{+} Tmem119^{+}) from different ages to assess gene expression along development (Bennett et al., 2016). Fcgr1 is expressed throughout development with an increase of expression as of P7 in Tmem119-positive microglia. Similarly, the inhibitory receptor Fcgr2b is expressed across ages, but its expression increases as of P14. According to their data, Fcgr3 is expressed throughout development and Fcgr4 peaks at P7 in Tmem119^{+} microglia. Together these data indicate that activating FcRs might be relatively abundant at early developmental time points. In the data from Saunders and colleagues generated from single-cell sequencing, FcRs are highly expressed with Fcgr3 being the most abundant, followed by Fcgr2b, Fcgr1, and Fcgr4.

The role of the FcRs in microglia is currently still unknown. Nakahara and colleagues examined FcR expression in the brain with immunohistochemistry using an antibody called 2.4G2 that recognizes Fcgr2 and Fcgr3, possibly also Fcgr1 and found expression in white matter areas during development (Nakahara et al., 2003). To test its role in myelination, they genetically deleted Fcer1g, the common gamma chain for all activating FcRs, which disabled Fcgr1, Fcgr3, and Fcgr4 and caused defects in myelin protein expression, oligodendrocyte numbers, and myelin ultrastructure. While the authors find that OPCs express *Fcer1g in vitro,* there is little evidence

that oligodendrocytes express *Fcer1g* and it seems more likely that this phenotype is at least in part, if not entirely, mediated through microglia that highly express *Fcer1g*.

Studying the Role of Microglia in Health and Disease Using Cre and CreERT2 Mouse Lines

Studying the role of microglial *Fcer1g* or other candidate genes in myelination and other physiological or pathophysiological processes largely hinges on the Cre/loxP system. Both constitutively active Cre lines and tamoxifen-inducible CreERT2 lines can be used for this purpose. Currently, several constitutively active Cre lines are available including *LyZ2-Cre, Tie2-Cre, HoxB8-Cre, Vav-Cre, Csf1r-iCre, Cx3cr1-Cre (Jung), Cx3cr1-CreM*, and *Cx3cr1-CCre/Sall1-N-Cre*, which display different strengths and weaknesses (Table 1, Georgiades et al., 2002; Chen et al., 2010; Tang et al., 2010; Luo et al., 2013; Yona et al., 2013; Perdiguero et al., 2015; Orthgiess et al., 2016; Wong et al., 2017, 2017; De et al., 2018; Haimon et al., 2018; Culemann et al., 2019; Grüneboom et al., 2019; Liu et al., 2019a; Zhao et al., 2019; Kim et al., 2021).

Lyz2 is broadly expressed in microglia and monocytes (Hammond et al., 2019), but also neutrophils, peritoneal macrophages, alveolar macrophages, Ly6Chi monocytes, and epithelial cells (ImmGen.org). Using homologous recombination, Clausen and coworkers replaced the coding sequence of *Lyz2* with Cre to create the *Lyz2-Cre* line. This line displays low to moderate recombination activity in microglia, moderate activity in white blood cells and high activity in neurons (Clausen et al., 1999; Orthgiess et al., 2016; Wong et al., 2017).

Tie2-Cre was generated by a bacterial artificial chromosome (BAC) approach (Kisanuki et al., 2001). While *Tie2* (*Tek*) is not expressed by adult microglia (Hammond et al., 2019), erythromyeloid precursor cells (EMPs), bone marrow hematopoietic stem cells, NK cells, innate

lymphoid cells, endothelial cells and lymphatic endothelial cells express Tek (ImmGen.org). *Tie2-Cre* recombines floxed alleles in microglia, as well as T-cells, B-cells and granulocytes, and endothelial cells (Tang et al., 2010; Perdiguero et al., 2015). This line is suitable for microglia targeting when endothelial cells and white blood cells are not a concern.

HoxB8 is neither expressed by microglia nor by peripheral immune cell subsets (Hammond et al., 2019, ImmGen.org). However, a subset of progenitors during the second wave of yolk sac hematopoiesis transiently expresses this gene (De et al., 2018). *HoxB8-Cre*, which was generated by inserting *IRES-Cre* into the *HoxB8* 3' UTR by homologous recombination, targets this population, but also T-cells, B-cell, monocytes, and interneurons in the spinal cord (Chen et al., 2010; De et al., 2018). Overall, this line is suitable only for the study of the *HoxB8* subset of microglia.

Vav-Cre is a BAC-transgenic Cre line based on the Vav gene (Georgiades et al., 2002), which is sparsely expressed in microglia, as well as several subsets of peripheral immune cells, including EMPs (Hammond et al., 2019, ImmGen.org). Consistently, Cre effectively recombines floxed sequences in microglia and white blood cell subsets. Other major cell types have not been assessed.

Another BAC-transgenic line, *Csf1r-iCre* is based on broad *Csf1r* expression in microglia subsets. In addition to microglia, the *Csf1r* gene is endogenously expressed in neutrophils, macrophage subsets, and Ly6C^{hi} monocytes. Accordingly, *Csf1r-iCre* is highly active in microglia, granulocytes, T-cells, and neurons (Luo et al., 2013; Perdiguero et al., 2015; Plein et al., 2018). However, due to the recombination in neurons, this line is rarely used to target microglia.

Cx3cr1 is a gene expressed broadly by different microglia subsets (Hammond et al., 2019). In the periphery, Ly6Chi monocytes, NK cells, and T-cells also harbor Cx3cr1 transcripts

(ImmGen.org). Several lines targeting this locus are currently available. Jung and coworkers created a *Cx3cr1-Cre* line by replacing the endogenous coding sequence with Cre (Yona et al., 2013). This line effectively targets recombines floxed sequences in microglia. However, it also displays activity in monocyte precursors, monocytes, dendritic precursors, and most notably, neurons (Yona et al., 2013; Haimon et al., 2018). A second line, Cx3cr1-CreM (M for MMRRC) was created by the GENSAT project using a bacterial artificial chromosome (Gong et al., 2010). This line displays high Cre efficiency in microglia and other peripheral macrophage subsets (Culemann et al., 2019; Grüneboom et al., 2019; Liu et al., 2019a). Further peripheral expression includes white-blood cells, however, neurons were spared by this line (Liu et al., 2019a). Thirdly, taking advantage of a lack of co-expression of *Sall1* and *Cx3cr1* in peripheral subsets (ImmGen.org), Jung and colleagues created a *Cx3cr1-CCre / Sall1-NCre* split-Cre line by inserting *2A-CCre/NCre* peptides into the 3' UTR of the respective genes (Kim et al., 2021). This line is highly specific with no expression in any peripheral subsets. However, efficiency of recombination is very low in these split-Cre mice when the N- and C-terminal Cre alleles are heterozygous. Only homozygous configuration in both loci enables high Cre activity in microglia, which overall limits the utility of this line to fate mapping rather than functional studies.

Together, the available Cre lines enabled significant advances in the field. At the same time, some lines display limited utility due to low efficiency or significant undesired activity in neurons or white blood cell subsets. The latter is particularly an issue in studies of risk genes for Alzheimer's disease, multiple sclerosis, or stroke amongst others, which are diseases involving monocyte infiltration (Henderson et al., 2009; Ritzel et al., 2015; Shang et al., 2016).

Table 1: Currently available constitutively active Cre lines

	LyZ2-Cre	Tie2-Cre	HoxB8-Cre	Vav-Cre	Csf1r-iCre	Cx3cr1-Cre (Jung)	Cx3cr1-CreM	Cx3cr1/Sall1 Split Cre
Bulk RNAseq of Immune populations (ImmGen)	Neutrophils, Peritoneal Mϕ, Alveolar Mϕ, Ly6Chi monocytes, Epithelial cells	BM HSCs, NK, ILC, Endothelial cells, Lymphatic endothelial cells	None	Broad across subsets	Neutrophils, peripheral Mϕ subsets, Ly6Chi monocytes	Ly6Chi monocytes, NK cells, T-cells	Ly6Chi monocytes, NK cells, T-cells	None for combination
Microglia scRNAseq (Hammond et al)	Broad, high in monocytes/ BAM	Not expressed	Not expressed	Sparse	Broad	Broad	Broad	Sparse (Sall1), broad (Cx3cr1)
Design	Knock-in, Cre (LyZ2 expression not preserved)	BAC, Cre	Knock-in, IRES-Cre	BAC, Cre	BAC, iCre	Knock-in replacing endogenous gene, Cre	BAC, Cre	Knock-in, 2A-Cre (slightly reduced endogenous levels)
Efficiency in Microglia	Low	Moderate-High	Subset	High	High	High	High	Low (13% in heterozygous, 88% in homozygous)
Develop-mental expression	Not assessed	Early (Yolk sac EMPs)	Early	Early	Early	Early	Not assessed	Early
Choroid plexus Mϕ	Not assessed	Not assessed	Yes	Not assessed	Not assessed	Yes	Yes	No
Peri-vascular Mϕ	Not assessed	Not assessed	Yes	Not assessed	Not assessed	Yes	Yes	No
Meningeal Mϕ	Not assessed	Not assessed	Yes	Not assessed	Not assessed	Yes	Yes	No
White blood cells	Yes	T-cells, B-cells, granulocytes	T-Cells, B-cells, monocytes	Yes	Granulocytes, T cells	Ly6Clo, Ly6hi, monocyte precursors, dendritic precursors	Not assessed	No
Other major cell types	Neurons	Endothelial cells, adult HSC	Interneurons (spinal cord)	Not assessed	Neurons	Neurons	No	No
Kidney Mϕ	Yes	Yes	Yes	Yes	Yes	Yes	Yes	Not assessed
Liver Mϕ	Yes	Yes	Yes	Yes	Yes	Yes	Yes	No
Spleen Mϕ	Yes	Yes	Yes	Yes	Yes	Yes	Yes	No
Intestinal Mϕ	Yes	Yes	Yes	Yes	Yes	Yes	Yes	Not assessed
References	(Orthgiess et al., 2016; Wong et al., 2017)	(Tang et al., 2010; Perdiguero et al., 2015)	(Chen et al., 2010; De et al., 2018)	(Georgiades et al., 2002; Wong et al., 2017)	(Luo et al., 2013; Perdiguero et al., 2015; Plein et al., 2018)	(Yona et al., 2013; Haimon et al., 2018)	(Culemann et al., 2019; Grüneboom et al., 2019; Zhao et al., 2019)	(Kim et al., 2021)

In constitutively active Cre lines, recombined alleles in monocytes result either from ongoing expression of Cre from the target locus or transient expression of Cre during development.

In contrast, the inducible variant, CreERT2, has been widely used to circumvent recombination of floxed alleles in monocytes during adulthood through early induction and experimental delay allowing turnover of monocytes (Goldmann et al., 2016). The currently available CreERT2 lines include *Cx3cr1-CreERT2, HexB-CreERT2, Tmem119-CreERT2,* and *P2ry12-CreERT2* (Table 2, Yona et al., 2013; Kaiser and Feng, 2019; Masuda et al., 2020; McKinsey et al., 2020).

Two lines of *Cx3cr1-CreERT2* mice have been generated to date, which are widely used to recombine floxed alleles in microglia. One line, *Cx3cr1-CreERT2*^{Jung} was developed by the Jung lab through knock-in of *CreERT2* into the coding region of *Cx3cr1*, thus driving expression from the endogenous locus while disrupting *Cx3cr1* expression (Yona et al., 2013). A second line was generated by Gan and coworkers who knocked *CreERT2-IRES-EYFP* into the start codon of *Cx3cr1* located in exon 2 (Parkhurst et al., 2013). While the initial studies showed high efficiency and specificity, later studies of these inducible lines revealed both leakiness in absence of tamoxifen and low-moderate off-target expression, especially in neurons (Parkhurst et al., 2013; Yona et al., 2013; Haimon et al., 2018; Zhao et al., 2019). In addition to undesired expression in neurons, *Cx3cr1-CreERT2* mice display Cre activity in border-associated macrophages and 20-90% of monocytes, as well as peripheral macrophages (Masuda et al., 2020). The *Cx3cr1-CreERT2* lines are useful for the study of microglia in health and disease, with the caveats that distinction from other myeloid cells is not possible and that some degree of leakage and off-target activity occurs.

HexB-CreERT2 was recently developed by Prinz and colleagues with the aim of targeting microglia in disease models that require the target locus to be unaffected by downregulation due to disease mechanisms as seen for many homeostatic microglia genes (Masuda et al., 2020). Specifically, the line was generated by inserting the *T2A-CreERT2* sequence into the stop codon

of *HexB*, which largely preserves endogenous expression. Initial studies characterizing this line indicate decent efficiency at 50-100% depending on the floxed allele and tamoxifen dosing paradigm with the caveat that studies were conducted using mice homozygous at the *CreERT2* and the Rosa reporter locus, which may overestimate the efficiency seen in typical conditional knockout experiments. With respect to specificity, *HexB-CreERT2* only target 10-20% of perivascular and meningeal macrophages. Choroid plexus macrophages were not analyzed but should display CreERT2 activity based on scRNA sequencing studies (Li et al., 2019). Peripherally, *HexB-CreERT2* mice recombine floxed alleles in 20-70% of monocytes and 100% of Ly6G-expressing neutrophils, but spare macrophages in kidney, liver, and spleen when tamoxifen is given early postnatally in a YFP reporter line. Further, using this paradigm, *HexB-CreERT2* mice appear to display activity in hepatocytes. This line excels in disease contexts and when peripheral macrophage subsets must be avoided.

A third line, *Tmem119-CreERT2*, was created by inserting *P2A-CreERT2* into the stop codon of the microglia-specific gene *Tmem119* (Chapter 1, Bennett et al., 2016; Kaiser and Feng, 2019) Using the Ai14 tdTomato reporter, *Tmem119-CreERT2* mice were shown to be highly efficient at recombining floxed alleles in microglia, while sparing border-associated macrophages and monocytes. Different microglia subsets were not studied in detail, however, some subsets such as proliferative region-associated microglia observed during early development may not be efficiently targeted based on scRNA sequencing studies (Li et al., 2019). With respect to off-target tissues, Tmem119-CreERT2 displays activity in leptomeningeal cells. This line excels when distinction of microglia from monocytes and other border associated macrophages is essential and off-target effects in leptomeningeal cells are acceptable.

P2ry12-CreERT2 was recently developed by Arnold and coworkers by knocking *P2A-CreERT2* into the stop codon of *P2ry12*, thus preserving the expression of the gene, at least on the protein level (McKinsey et al., 2020). This line recombines floxed alleles efficiently in microglia, whereas it almost completely avoids border-associated macrophages with only about 20% of choroid plexus and 25% of dural macrophages being targeted. Further, *P2ry12-CreERT2* does not display activity in monocytes and only minor activity in intestinal, heart, and lung macrophages. In the spleen and liver, a slightly higher proportion of macrophages is targeted, although the fraction is still low. Using tamoxifen administration during embryonic development, the authors also showed that *P2ry12-CreERT2* can recombine floxed sequences during early development. This line excels for targeting of microglia when monocytes and other macrophage subsets are a concern. An additional plus is that suitability for studies during early development has been demonstrated.

Together, the available CreERT2 lines for microglia have and will continue to enable studies into the function of microglia in health in disease. A shared advantage of these lines is that the time of induction can be chosen such that some off-target tissues can be avoided. At the same time, by design, the available lines collectively share the drawback that they require tamoxifen administration, which is disadvantageous for studies of sex-specific effects, early embryonic and postnatal development, and for labs with limited access to the required equipment and space. Given these limitations and the limitations of the current constitutively active Cre lines discussed above, an improved constitutively active Cre line would critically facilitate studies into the role of microglia in different contexts.

Table 2: Currently available inducible CreERT2 lines

	HexB-CreERT2	P2ry12-CreERT2	Cx3cr1-CreERT2	Tmem119-CreERT2
Bulk RNAseq of Immune populations (ImmGen)	Peripheral macrophage subsets, monocytes, B and T-cell subsets (low)	T-cells, dendritic cells, peripheral macrophage subsets	Ly6Chi monocytes, NK cells, T-cells	Peripheral macrophage subsets (low)
Microglia scRNAseq (Hammond et al)	Broad	Broad, lower in axon-tract microglia	Broad	Broad, lower in axon-tract microglia
Design	Knock-in (T2A-CreERT2, preserving endogenous expression)	Knock-in (P2A-CreER, endogenous expression slightly reduced)	Knock-in (not preserving endogenous expression)	Knock-in (P2A-CreERT2, preserving endogenous expression)
Efficiency in Microglia	Variable (50-100% depending on floxed allele and TAM dosage), assessed using HexB-CreERT2/CreERT2 homozygous mice	High (80-95%)	High (~99%)	High (~99%)
Leakiness (no Tamoxifen)	Slightly	None	Moderate	None
Developmental expression	Not assessed	Early	Early	Early, but lower in some subsets
Choroid Plexus Mϕ	Not assessed	21%	High	No
Perivascular Mϕ	10-20%	No	80-90%	No
Meningeal Mϕ	10-20%	25% in Dura mater, none in Pia mater	70%	No
White blood cells	100% Ly6G, 20% Ly6Chi, 70% Ly6Clo (Ai14 reporter), lower in YFP reporter	No	20% Ly6Chi, 90% Ly6Clo, none in Ly6G neutrophils	~3%
Other major cell types	Hepatocytes depending on TAM timing	No	Not expressed	Leptomeningeal cells
Kidney Mϕ	Depending on TAM timing	No	Macrophages	Not assessed
Liver Mϕ	None	Macrophages	Macrophages	Not assessed
Spleen Mϕ	Low-moderate	27% Macrophages	Macrophages	Not assessed
Intestine Mϕ	Not assessed	5% Macrophages	Macrophages	Not assessed
Lung Mϕ	Not assessed	5% Macrophages	Macrophages	Not assessed
Heart Mϕ	Not assessed	10% Macrophages	Macrophages	Not assessed
References	(Masuda et al., 2020)	(McKinsey et al., 2020)	(Parkhurst et al., 2013; Yona et al., 2013; Masuda et al., 2020; McKinsey et al., 2020)	(Kaiser and Feng, 2019)

Fcrls - a Microglia-Specific Gene Suitable for Targeting

Fc receptor- like S, scavenger receptor (*Fcrls*) is a 509-amino-acid protein encoded by the Fcrls-201 transcript of 2273 base pairs in mice. This transcript is located on the reverse strand of chromosome 3 covering a 12.8kb region. *Fcrls-201* comprises 8 exons with the ATG start on exon 1 and the TGA stop on exon 8. In addition to *Fcrls-201*, there is an annotation of *Fcrls-202*, a truncated transcript that includes a cryptic 5' exon, however, this annotated transcript would lack

a stop codon to create functional protein and appears not to be expressed in RNA sequencing datasets from sorted microglia (Kaiser and Feng, unpublished data).

There are several datasets indicating that *Fcrls* is a suitable target locus for the generation of a microglia Cre line. Bulk RNA sequencing of FACS- or immunopanning-enriched cell types revealed that only microglia express *Fcrls* in the brain (Zhang et al., 2014). Similarly, Butovsky and colleagues found *Fcrls* to be the most enriched gene in gene and protein profiling studies after isolating $CD11b^{+}CD45^{lo}$ microglia from the CNS and $CD11b^{+}Ly6C^{+}$ monocytes from the spleen (Butovsky et al., 2014). Further substantiating this, the absence in *Fcrls* in monocytes and other peripheral immune cell subsets is also mirrored in data collected at the ImmGen database (ImmGen.org). More recently, single cell RNA sequencing studies demonstrated that *Fcrls* is expressed across all microglia subsets (Hammond et al., 2019; Li et al., 2019). With respect to its temporal expression profile, Mass and coworkers showed that *Fcrls* is expressed during early embryonic development in the brain (Mass et al., 2016). Together, the cell-type specific and temporal profiling studies indicate that *Fcrls* is a suitable target locus for the generation of a constitutively active Cre line, with particular focus on the absence of expression in monocytes and other white blood cells.

1 Development of Transgenic Mice to Label and Manipulate Microglia

I generated the Tmem119-EGFP and Tmem119-CreERT2 mice, developed and executed genotyping and qPCR assays, conducted microglia morphology studies, immunofluorescence staining, and flow cytometry assays. Special thanks to Dongqing Wang for contributing to tamoxifen administration, Nicholas Sanders for colony maintenance, and Ohyoon Kwon for contributing to the morphology analysis.

This chapter was previously published by Tobias Kaiser and Guoping Feng in eNeuro: 1 August 2019, 6 (4) ENEURO.0448-18.2019; DOI: https://doi.org/10.1523/ENEURO.0448-18.2019.

1.1 Abstract

Microglia are specialized brain-resident macrophages with important functions in health and disease. To improve our understanding of these cells, the research community needs genetic tools to identify and control them in a manner that distinguishes them from closely related cell-types. I have targeted the recently discovered microglia-specific *Tmem119* gene to generate knock-in mice expressing EGFP (JAX#031823) or CreERT2 (JAX#031820) for the identification and manipulation of microglia, respectively. Genetic characterization of the locus and qPCR-based analysis demonstrate correct positioning of the transgenes and intact expression of endogenous *Tmem119* in the knock-in mouse models. Immunofluorescence analysis further shows that parenchymal microglia, but not other brain macrophages, are completely and faithfully labeled in the EGFP-line at different time points of development. Flow cytometry indicates highly selective expression of EGFP in $CD11b^{+}CD45lo$ microglia. Similarly, immunofluorescence and flow cytometry analyses using a Cre-dependent reporter mouse line demonstrate activity of CreERT2 primarily in microglia upon tamoxifen administration with the caveat of activity in leptomeningeal cells. Finally, flow cytometric analyses reveal absence of EGFP expression and minimal activity of CreERT2 in blood monocytes of the *Tmem119-EGFP* and *Tmem119-CreERT2* lines, respectively. These new transgenic lines extend the microglia toolbox by providing the currently most specific genetic labeling and also highly precise control over these cells in the myeloid compartment of mice.

1.2 Introduction

Microglia are specialized brain-resident macrophages that comprise 5 to 12% of the glial cells in the adult mouse brain (Lawson et al., 1990). Under physiological conditions, phagocytic and secretory activity of these glia support neurogenesis, development of neuronal connectivity, and survival of neurons (Stevens et al., 2007; Sierra et al., 2010; Paolicelli et al., 2011; Schafer et al., 2012; Ueno et al., 2013; Weinhard et al., 2018). Complementing these homeostatic functions, microglia react to perturbations, which has been shown in the context of vascular injury, multiple sclerosis lesions, and neurodegeneration (Itagaki et al., 1989; Davalos et al., 2005; Ransohoff, 2016; Aguzzi and Zhu, 2017; Keren-Shaul et al., 2017; Mathys et al., 2017; O'Loughlin et al., 2018). In the future, many of these processes and their potential for therapeutic targeting will be further examined, and understanding of both homeostatic and disease-related contributions of microglia will critically depend on means to specifically identify and control them. Several mouse lines are currently available for either fluorescent labeling or Cre-expression that harness the loci of putative microglia signature genes *Tie2, Runx1, Csf1r, Aif1, Lyz2, Itgam, Sall1,* or *CX3cr1* (Clausen et al., 1999; Sasmono et al., 2003; Ferron and Vacher, 2005; Hirasawa et al., 2005; Samokhvalov et al., 2007; Ginhoux et al., 2010; Parkhurst et al., 2013; Yona et al., 2013; Buttgereit et al., 2016). Collectively, these mouse lines have been instrumental in gaining insights on microglia. However, furthering our understanding of microglia using the currently available lines is complicated by the fact that it is difficult to distinguish microglia from other closely related peripheral and central cell types such as blood monocytes as well as perivascular, choroid plexus, and meningeal macrophages (Wieghofer and Prinz, 2016; Haimon et al., 2018).

Recent advances in RNA sequencing and other cell profiling technologies have enabled the discovery of cell type-specific signature genes (Butovsky et al., 2014). Amongst these,

transmembrane protein 119 (*Tmem119*) is highly and exclusively expressed in microglia in the brains of mice and humans(Bennett et al., 2016; Satoh et al., 2016). While TMEM119-specific antibodies are already widely used as a gold standard for immunohistochemical methods, faithful fluorescent reporter lines and inducible Cre-lines that allow *in vivo* observation and manipulation are currently not available. Here, we report the generation and characterization of knock-in mouse lines *Tmem119-EGFP* (JAX#031823) and *Tmem119-CreERT2* (JAX#031820), where microglia express EGFP and CreERT2, respectively, while preserving endogenous *Tmem119* expression. We demonstrate that EGFP is expressed throughout the brain and that the tag is confined to microglia only, without significantly labeling other brain macrophages. We further provide evidence that the inducible Cre is primarily active in microglia by crossing to the conditional fluorescent reporter mouse line Ai14. In these mice, we also observe activity in leptomeningeal cells that line the surface of the brain and penetrate deep into the brain ensheathing some large blood vessels. Finally, we demonstrate minimal to absent transgene expression in monocytes of the mice. These publicly available mouse lines provide valuable tools for the functional study of bona fide microglia.

1.3 Results

1.3.1 Generation and genetic confirmation of Tmem119-EGFP and Tmem119-CreERT2 knock-in lines

Access to highly specific fluorescent reporter lines for imaging and Cre-driver lines for functional manipulation is critical in our quest for understanding the roles of microglia in health and disease. Previously generated lines efficiently target microglia, but also other cells of the monophagocytic system (Wieghofer and Prinz, 2016). Amongst a group of more recently discovered microglia-specific genes, we chose targeting the *Tmem119* gene to generate such mouse lines (Bennett et al., 2016). Specifically, we opted for a transgenic approach that harnesses the *Tmem119* locus to drive expression, while preserving endogenous *Tmem119* expression. We designed a CRISPR/Cas9 strategy to insert EGFP or CreERT2, preceded by ribosome-skipping peptide porcine teschovirus-1 polyprotein (P2A), into the stop codon of murine *Tmem119* (Figure 1A). Two founder lines were established for Tmem119-EGFP and 5 for Tmem119-CreERT2.

To determine whether the donor DNA was inserted correctly, a PCR-based approach was used with primers spanning each junction. For both of the lines generated, specific 5' and 3' junction PCR products were obtained, while no bands were observed with DNA from wildtype animals (Figure 1B). This indicates specific insertion of the transgenes into the *Tmem119* locus. To further examine scarless integration at the junctions, PCR products from the CreERT2 line were subject to Sanger sequencing covering the junctions. Both 5' and 3' sequencing traces show endogenous bases corresponding to the WT sequence in intron 1 and the 3' UTR (Figure 1C, D). Additional sequencing confirmed absence of mutations across the entire targeted allele in both lines. Together, these results confirm the generation of *Tmem119-EGFP* and *Tmem119-CreERT2* lines.

While the function of endogenous *Tmem119* is currently unknown, both its temporally distinct pattern and high expression level suggest functional importance of this gene (Bennett et al., 2016). We thus designed a knock-in approach with the objective of leaving endogenous expression intact. To test whether *Tmem119* expression is unaffected, we quantified *Tmem119* transcript levels in the *Tmem119-EGFP* line by qPCR. Examination of *Tmem119* expression in WT and *Tmem119-EGFP*$^{+/-}$ mice revealed that transcript levels are comparable between genotypes (Figure 1E, WT median 0.9717, n=4, EGFP$^{+/-}$ median 0.9306, n=6, p= 0.5667). We further examined TMEM119 protein expression using immunofluorescence and found no difference between wildtype and *Tmem119-EGFP*$^{+/-}$ knock-in mice (Figure 1F-G, WT median 0.9835, n=4, EGFP$^{+/-}$ median 1.117, n=4, p=0.20) Together, these data support the conclusion that *Tmem119* knock-in mice were generated with precision.

To further test whether the genetic engineering could affect the properties of microglia, we examined basic morphological features of reconstructed immunostained microglia in wildtype and *Tmem119-EGFP*$^{+/-}$ knock-in mice (Figure 1H-I). Using this approach, we determined that the cell body area (Figure 1J, WT median 50.67 μm^2, EGFP$^{+/-}$ median 46.82 μm^2, n=12 microglia from 4 mice per genotype, p=0.3429), number of processes (Figure 1K, WT median 6.167, EGFP$^{+/-}$ median 5.667, n=12 microglia from 4 mice per genotype, p=0.4571), convex hull area (Figure 1L, WT median 2413 μm^2, EGFP$^{+/-}$ median 1871 μm^2, n=12 microglia from 4 mice per genotype, p=0.4857), and total process length (Figure 1M, WT median 351.2 μm, EGFP$^{+/-}$ median 419.6 μm, n=12 microglia from 4 mice per genotype, p=0.3428) are comparable between microglia from control and knock-in mice. These data suggest that the genetic modification does not affect basic microglial properties.

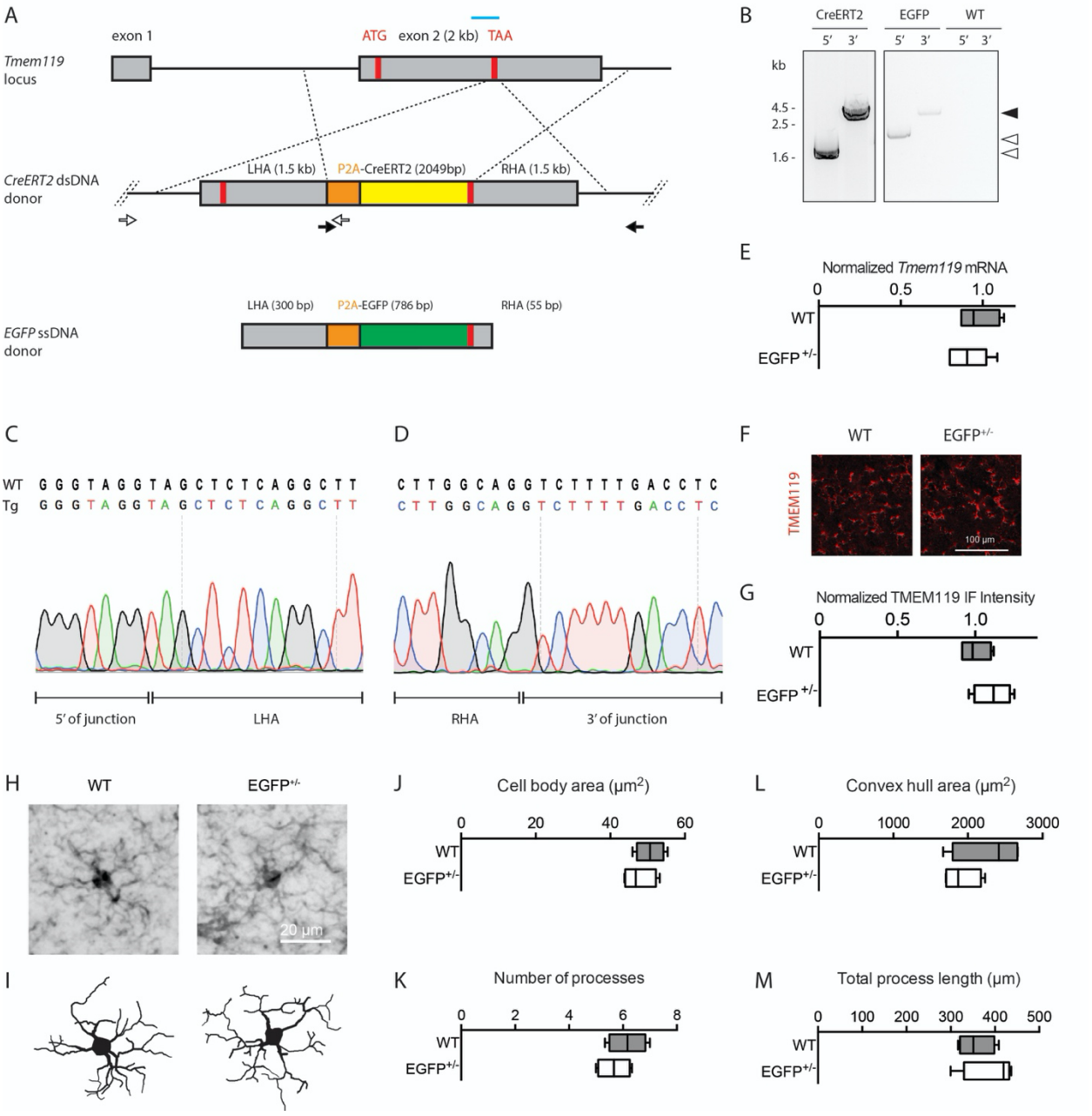

Figure 1: Generation and validation of *Tmem119-EGFP and Tmem119-CreERT2* knock-in lines. A, Experimental strategy using a guide RNA (blue bar) to introduce a double-strand break at the *Tmem119* stop codon in mouse zygotes and an injection mixture containing *EGFP* ssDNA template with short homology arms of 55-300 bp or *CreERT2* dsDNA template with long 1.5 kb homology arms. Each knock-in is designed to cause in-frame insertion of P2A peptide followed by *EGFP* or *CreERT2* and a stop codon. Not drawn to scale. **B**, Confirmation of insertion by amplification of fragments spanning the 5' and 3' junctions using sets of primers binding inside the template and outside the homology arms (open and closed arrows in A with arrowheads indicating corresponding products). **C and D**, Sanger sequencing across the 5' and 3' junction of the CreERT2 line and comparison to wildtype (WT) sequence indicate seamless insertion in the transgenic mice (Tg). **E**, qPCR analysis of gene expression for *Tmem119* in wildtype

controls and *Tmem119-EGFP*$^{+/-}$ knock-in animals. N=4 WT, N=6 *Tmem119-EGFP*$^{+/-}$ mice. **F,** Representative TMEM119 immunoreactivity in wildtype controls and *Tmem119-EGFP*$^{+/-}$ knock-in animals. **G,** Relative intensity of TMEM119 immunostaining signal. N=4 WT, N=4 *Tmem119-EGFP*$^{+/-}$ mice. **H and I,** Representative IBA-immunostained microglia and corresponding neurolucida traces in WT and *Tmem119-EGFP*$^{+/-}$ knock-in mice. **J-M,** Quantified cell body area, number of processes, convex hull area, and total process length of microglia in WT and *Tmem119-EGFP*$^{+/-}$ knock-in mice. N= 12 microglia from 4 mice per genotype. ssDNA, single strand DNA; dsDNA, double strand DNA; TAA (red bar), stop codon; Kb, kilo bases.

1.3.2 EGFP is faithfully expressed in microglia

Microglia populate the parenchyma in virtually all regions across the brain. To determine the extent of EGFP expression in the newly generated *Tmem119-EGFP* line, we used confocal microscopy on brain slices. Native EGFP fluorescence and antibody-enhanced signal were visible across the brain in sagittal brain sections prepared from postnatal day 25 (P25) *Tmem119-EGFP+/-* mice (Figure 2A). To further assess whether EGFP is expressed in microglia, immunofluorescence labeling of the endogenous microglia proteins IBA1 and TMEM119 was employed. High power confocal microscopy shows that EGFP-positive cells in the parenchyma are IBA1 and TMEM119-positive (Figure 2B-E). Completion and fidelity of expression were further assessed quantitatively in several brain regions. We found that 96.1 ± 2.0 % of the EGFP-expressing cells in the somatosensory cortex are IBA-1 expressing microglia and 98.2 ± 3.3 % of IBA1-positive cells in this region are labeled by EGFP (Table 3). In the striatum, 99.2 ± 2.1 % of the cells labeled with EGFP were IBA1-expressing and 97.2 ± 1.8 % of IBA1-positive cells displayed EGFP fluorescence. Labeling of microglia in the thalamus and hippocampus was 98.5 ± 0.8 % and 98.9 ± 1.9 % complete and 96.9 ± 2.3 % and 98.5 ± 3.5 % specific, respectively. To further confirm EGFP expression in microglia across the brain, we used the *Tmem119-EGFP* line in flow cytometry (Figure 2F-N). We gated for single, live cells (Figure 2F-I) and detected EGFP^{+} cells among CD45^{+} cells (Figure J-M). We determined that all CD11b^{+}CD45lo microglia (Figure 2K)

expressed EGFP (Figure 2N). In addition, to more comprehensively assess specificity of EGFP expression, we immunostained oligodendrocytes, neurons, and astrocytes. We found no evidence for expression of EGFP in these major CNS celltypes (Figure 2O-Q). Together, these data indicate highly complete and specific labeling of parenchymal microglia in the *Tmem119-EGFP* reporter line.

Table 3: Quantification of EGFP labeled microglia in Tmem119-EGFP mice.

Brain Region	Completeness ($EGFP^+Iba^+/Iba^+$)	Fidelity ($EGFP^+Iba^+/EGFP^+$)
Somatosensory cortex	98.2 ± 3.3 %	96.1 ± 2.0 %
Striatum	97.2 ± 1.8 %	99.2 ± 2.1 %
Thalamus	96.9 ± 2.3 %	98.5 ± 0.8 %
Hippocampus	98.5 ± 3.5 %	98.9 ± 1.9 %

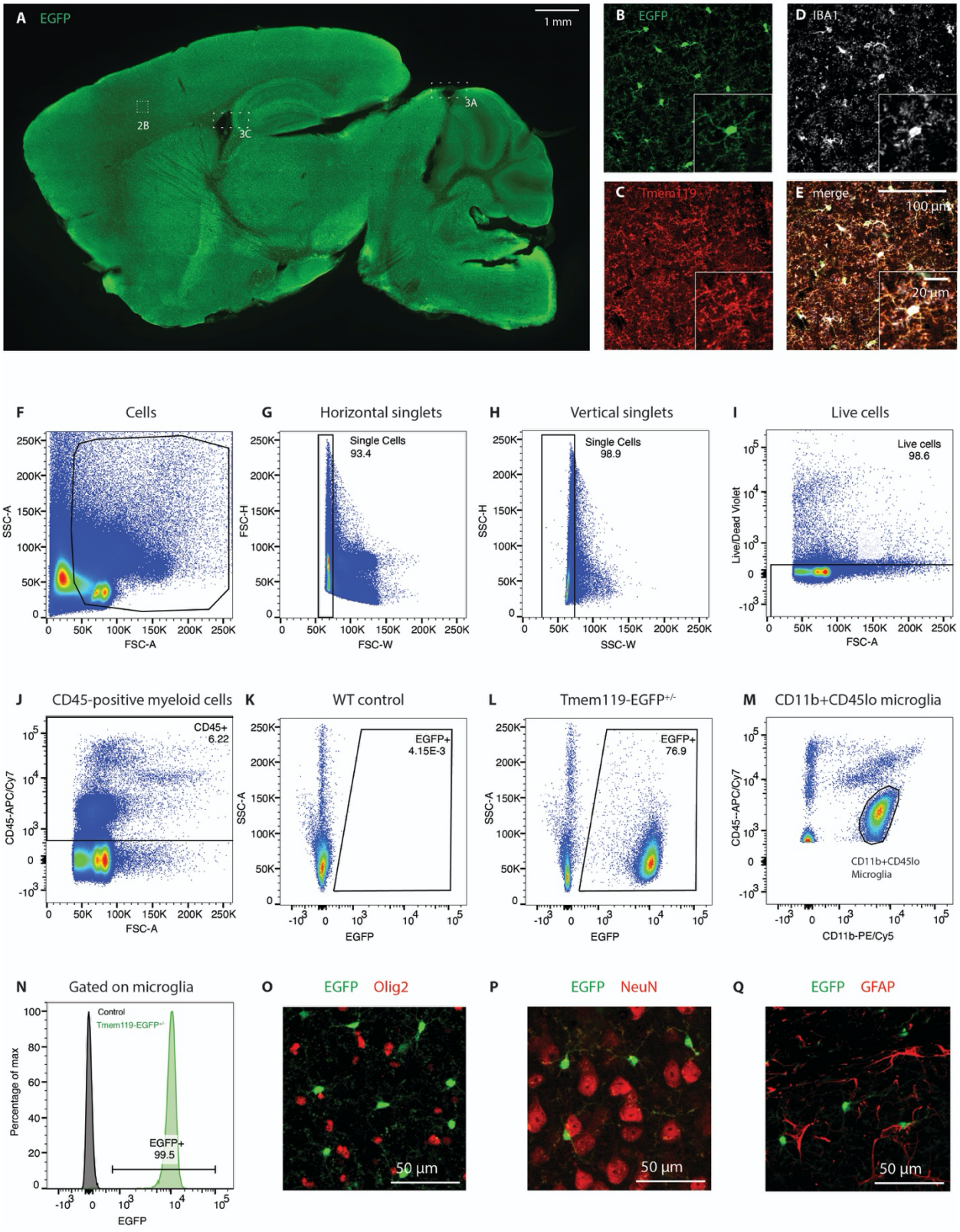

Figure 2: EGFP labels microglia in all regions across the brain. **A**, Representative epifluorescence image of a sagittal section of a P25 *Tmem119-EGFP*$^{+/-}$ mouse stained with an anti-GFP antibody for improved signal-to-noise

ratio (data for one of three mice shown). **B-E**, High-power confocal micrographs of native EGFP fluorescence (B, green) in TMEM119 (C, red) and IBA1 (D, white) microglia in the cortical region outlined in A. FIJI-calculated composite image showing all three labels (E). Boxes 3A and 3B cross-reference areas shown in figure 3.**F-J,** Flow cytometry analysis showing gating for of single, live, CD45-positive cells (one of three independent experiments shown). Numbers in or adjacent to outlined areas indicate percent cells in each gate. **K and L,** Representative density blots showing EGFP expression in WT and *Tmem119-EGFP*$^{+/-}$ mice (pre-gated on CD45^{+} cells). **M,** Representative density plot showing CD11b^{+}CD45lo cells corresponding to microglia (pre-gated on CD45^{+} cells). **N,** Histogram showing fraction of CD11b^{+}CD45lo microglia expressing EGFP. **O-R**, Representative immunostaining for oligodendrocytes (O, Olig2, red), neurons (P, NeuN, red), and astrocytes (Q, GFAP, red) in EGFP-expressing *Tmem119-EGFP*$^{+/-}$ mice. One of three independent experiments shown.

All microglia express IBA1, but not all IBA1-expressing cells are parenchymal macrophages. In fact, non-parenchymal macrophages such as meningeal, perivascular, and choroid plexus macrophages express the myeloid- and macrophage marker IBA1 (Prinz and Priller, 2014). To determine whether EGFP is expressed in these non-parenchymal macrophages, we examined EGFP immunofluorescence in IBA1-expressing cells in the meninges and choroid plexus, which can be readily discerned by their morphology and IBA1 immunoreactivity. High power confocal images from both regions, including adjacent parenchyma, show that, while parenchymal microglia express the EGFP label, neither IBA1-positive meningeal (Figure 3A, B) nor choroid plexus macrophages express EGFP (Figure 3C, D).

In contrast to the clear anatomical location of choroid plexus and meningeal macrophages, sites of perivascular macrophages are not easily discernible anatomically. To examine whether perivascular macrophages are labeled in the *Tmem119-EGFP* line, we stained for CD163, a well-characterized marker for perivascular macrophages (Kim et al., 2006). CD163 readily identified perivascular macrophages, which did not express EGFP (Figure 3E-F). Adjacent microglia were clearly labeled with EGFP.

To further assess the specificity of EGFP expression in microglia beyond anatomical location-based immunofluorescence analysis, we used flow cytometry (Figure 3G-I). Examining $CD45^{+}EGFP^{+}$ cells, we determined that 99.6% are $CD11b^{+}CD45$lo cells corresponding to microglia (Figure 3H). We further detected that 153 of 2212 $CD11b^{+}CD45$int/hi cells (6.9%) corresponding to non-microglial cells express EGFP (Figure 3G-I). Together, these data indicate the capacity of the *Tmem119-EGFP* line to distinguish parenchymal microglia from other brain macrophages with good selectivity.

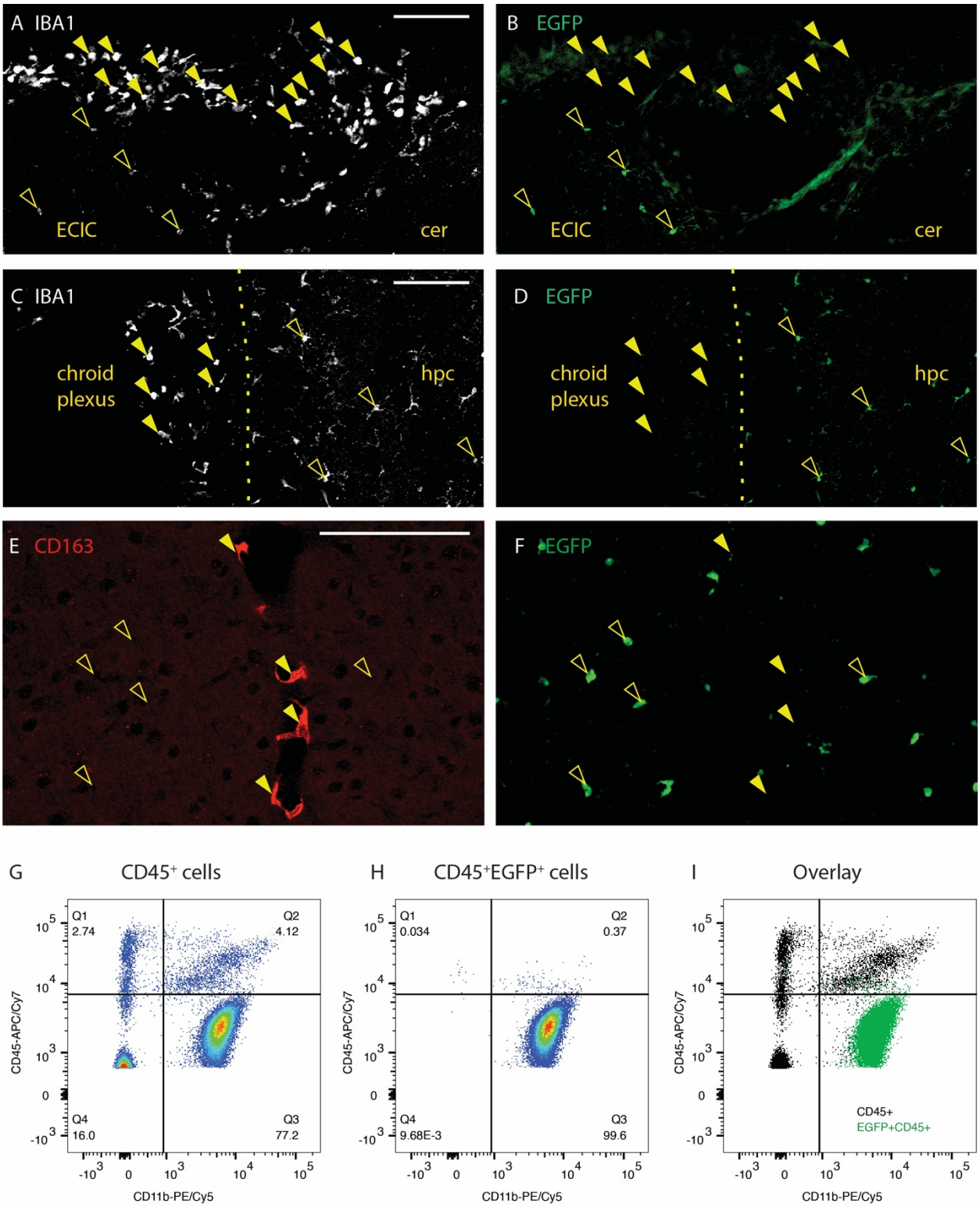

Figure 3: EGFP discerns parenchymal microglia from other brain macrophages. A, IBA1 labels meningeal macrophages and parenchymal microglia from the region indicate with a dashed box in figure 2A. **B**, EGFP labels only parenchymal macrophages (open arrowheads), but not meningeal IBA1-positive macrophages (closed

arrowheads). Diffuse fluorescence is associated with pia. ECIC, external cortex of inferior colliculus; Cer, cerebellum. Scale bar 100 μm. **C and D**, Choroid plexus IBA1$^+$ macrophages (closed arrowheads) from the region boxed in figure 2A are not labeled with EGFP, while adjacent parenchymal microglia are (open arrowheads). Hpc, hippocampus. Scale bar 100 μm. **E and F**, Perivascular CD163-expressing macrophages (E, red, closed arrowheads) are not labeled with EGFP (F, green, open arrowheads). Scale bar 100 μm. **G-I**, Flow cytometry analysis of CD11b and CD45 expression in pre-gated single live CD45$^+$ cells and EGFP-expressing CD45$^+$ cells of *Tmem119-EGFP*$^{+/-}$ mice shown as density plots (G, CD45$^+$ and H CD45$^+$ EGFP$^+$) and overlay (I, black CD45$^+$, green CD45$^+$ EGFP$^+$). One of three independent experiments (N ≥ 3 mice per group) shown. Numbers in or adjacent to outlined areas indicate percent cells in each gate.

1.3.3 EGFP is expressed in microglia of Tmem119-EGFP mice at early postnatal stages

Microglia populate the brain during early embryonic development (Ginhoux et al., 2010). *Tmem119* mRNA is expressed throughout microglial development, but antibody-based methods currently consistently label TMEM119 only as of later postnatal stages, typically postnatal day 14 (P14) and later (Bennett et al., 2016). This makes it difficult to identify and discern microglia from monocytes at earlier time points. To determine whether the *Tmem119-EGFP* line would specifically label microglia at early postnatal stages, we carried out immunofluorescence microscopy at postnatal days 1, 3, and 6. EGFP expression in IBA1-positive cells was readily observed in several regions examined, suggesting translation of *Tmem119-P2A-EGFP* transcript at this stage (Figure 4A-L). Surprisingly, we also found EGFP expression associated with blood vessels of P1 mice (Figure 4A-C), but not P3 or later, indicating that the transcript is also processed in cells of the intracerebral microvascular compartment at this stage. Together, these data indicate utility of the *Tmem119-EGFP* line for early developmental studies of microglia.

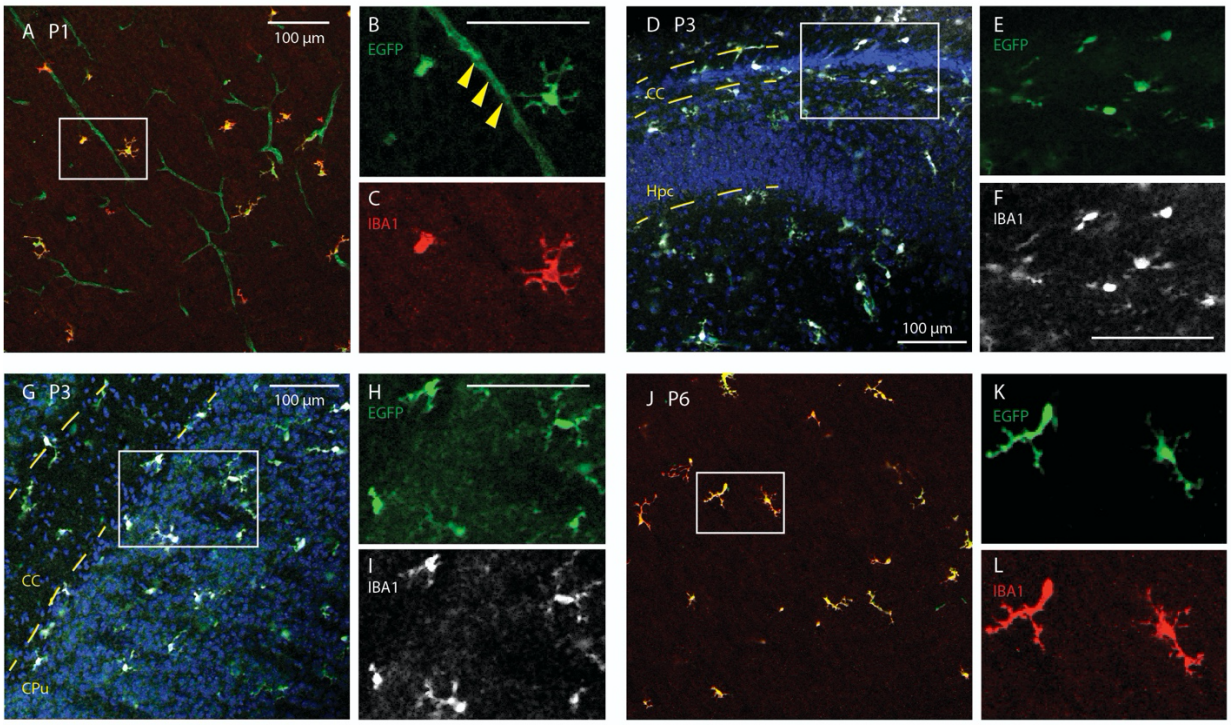

Figure 4: *Tmem119-EGFP* mice label microglia at early postnatal stages. Sagittal slices from postnatal day 1, 3 and 6 (P1, P3, P6) mice were stained against IBA1. **A-C**, High power confocal images of the somatosensory cortex show EGFP expression in IBA-positive cells and blood vessels at P1 (solid arrowheads in magnified panel). **D-F**, Confocal micrographs around the forceps major of corpus callosum (CC) and hippocampus (Hpc) show EGFP-labeled, IBA1-positive microglia at P3. **G-I**, Confocal micrographs of the striatum (CPu) and corpus callosum (CC) show EGFP labeling of IBA-positive cells at P3. **J-L**, Confocal micrographs of the P6 cortex reveal EGFP-expression in IBA-immunostained cells. Error bars 100 µm.

1.3.4 Cre activity is specifically inducible in microglia of Tmem119-CreERT2 mice

Cre activity in CreERT2 fusion protein is induced by the estrogen receptor antagonist tamoxifen and can be assessed in the presence of a reporter construct. To assess whether *Tmem119-CreERT2* mice display Cre activity in parenchymal microglia upon induction, we crossed *Tmem119-CreERT2* mice to the Ai14 reporter line (Madisen et al., 2010), which expresses tdTomato in the presence of Cre (Figure 5A). We administered tamoxifen daily for 3, 5, or 10 days to adult mice and 3 days to postnatal day 2 (P2) pups, and compared recombination efficiency and

fidelity for these different paradigms (Figure 5A). The mice were sacrificed 9-10 days after the last dose and subjected to immunofluorescence staining. High power images from confocal microscopy showed tdTomato-labeling of IBA1-expressing microglia in mice that received tamoxifen (Figure 5B-D) and absence of tdTomato expression without tamoxifen (Figure 5E-G). Confocal micrographs also indicated absence of tdTomato expression in other major cell types of the CNS, such as oligodendrocytes, neurons, and astrocytes (Figure 5H-J). Assessment of the completeness of labeling as the ratio of tdTomato^{+}IBA1^{+}- double positive microglia (tdT^{+}IBA1^{+}) to all parenchymal microglia (IBA1^{+}) revealed very high efficiency of recombination (Figure 5K). Similarly, we examined the fidelity of labeling which represents the fraction of actual parenchymal microglia (tdT^{+}IBA1^{+}) amongst all tdTomato-labeled cells (tdT^{+}) in different parenchymal regions, and found high specificity close to 100 percent (Figure 5L). Of note, increasing the days of tamoxifen administered to mice appeared to increase the fraction of microglia undergoing recombination. At the same time, prolonged administration of tamoxifen correlated with slightly reduced fidelity (Figure 5K-L). We further sought to assess the specificity of tdTomato expression using flow cytometry. Among a total of 1690 CD11b^{+}CD45int/hi cells in the CNS, 33 were positive for tdTomato, indicating minimal, yet nonzero, expression in non-microglial myeloid cells.

The flow cytometry data revealed that recombination was largely, but not 100 percent specific. Furthermore, when examining the sections, we noticed some tdTomato fluorescence that did not appear to be associated with parenchymal microglia. To explore the nature of this ectopic fluorescence in this dosing paradigm, we imaged cells in the choroid plexus (Figure 5N-P) as well as cells in the cortex, which were immunostained for the endothelial cell marker CD31 (Figure 5Q-S). In the choroid plexus, there was very weak tdTomato fluorescence and most IBA1-positive

macrophages did not express tdTomato (Figure 5N-P). In the cortex, high power confocal micrographs showed that the tdTomato and the CD31-immunolabeling signal were largely separate, with some tdTomato overlap with larger CD31-positive blood vessels (Figure 5Q-S). Furthermore, tdTomato fluorescence was present on the pia in IBA1-negative cells (Figure 5T-V) and absent from CD163-expressing perivascular macrophages (Figure 5W-Z). Together, these data indicate that the *Tmem119-CreERT2* line can be used to conditionally control gene expression in adult and early postnatal microglia with good specificity.

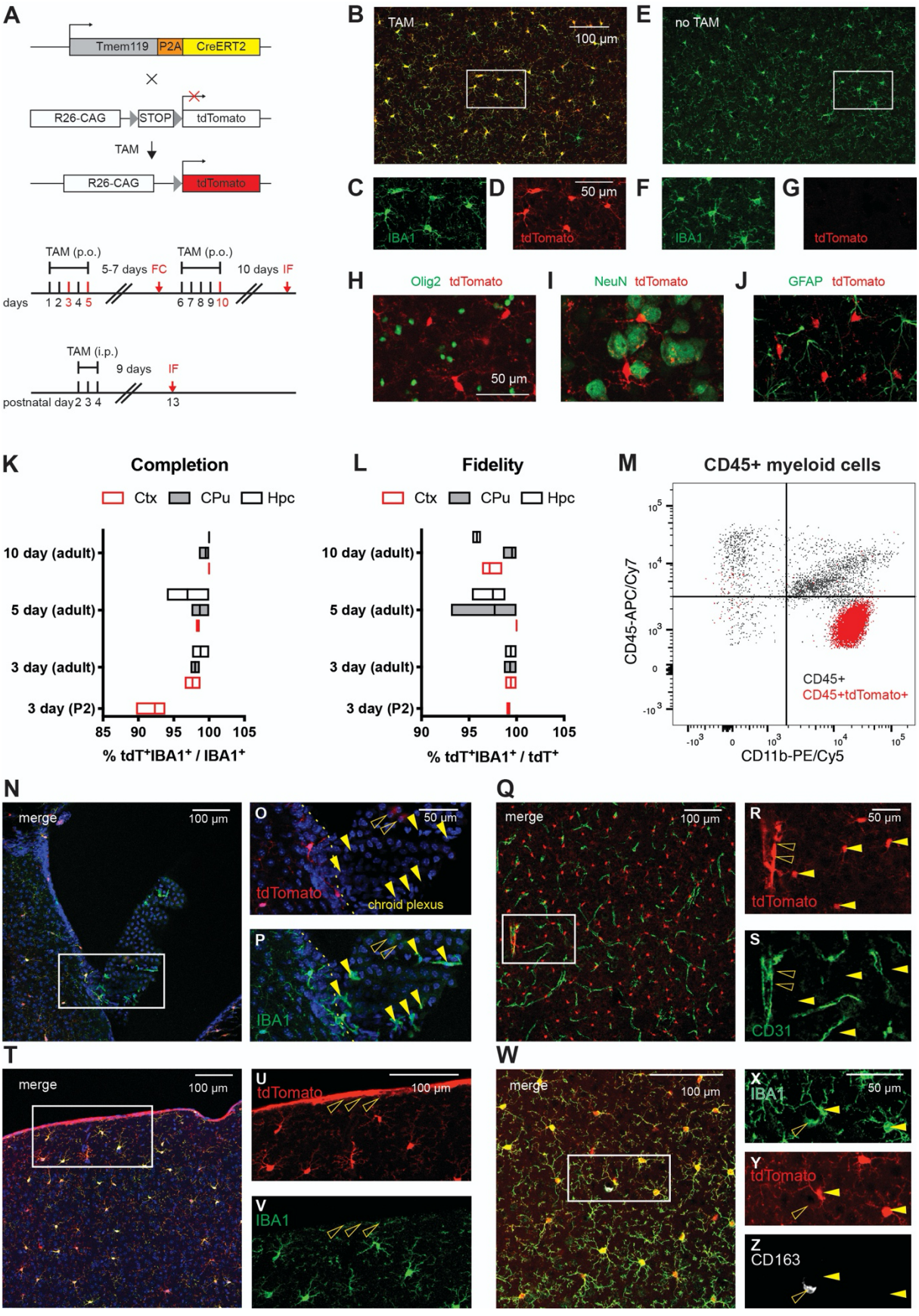
A
Tmem119
P2A
CreERT2
R26-CAG
STOP
tdTomato
TAM
R26-CAG
tdTomato
TAM (p.o.)
5-7 days FC
TAM (p.o.)
10 days IF
days 1 2 3 4 5
6 7 8 9 10
TAM (i.p.)
9 days
IF
postnatal day 2 3 4
13
B
TAM
100 µm
E
no TAM
C
IBA1
D
50 µm
tdTomato
F
IBA1
G
tdTomato
H
Olig2 tdTomato
50 µm
I
NeuN tdTomato
J
GFAP tdTomato
K
Completion
Ctx CPu Hpc
10 day (adult)
5 day (adult)
3 day (adult)
3 day (P2)
85 90 95 100 105
% tdT+IBA1+ / IBA1+
L
Fidelity
Ctx CPu Hpc
10 day (adult)
5 day (adult)
3 day (adult)
3 day (P2)
90 95 100 105
% tdT+IBA1+ / tdT+
M
CD45+ myeloid cells
CD45-APC/Cy7
CD11b-PE/Cy5
CD45+
CD45+tdTomato+
N
merge
100 µm
O
50 µm
tdTomato
choroid plexus
P
IBA1
Q
merge
100 µm
R
50 µm
tdTomato
S
CD31
T
merge
100 µm
U
tdTomato
100 µm
V
IBA1
W
merge
100 µm
X
IBA1
50 µm
Y
tdTomato
Z
CD163

Figure 5: *Tmem119-CreERT2* mice effectively recombine a conditional allele in microglia. A, *Tmem119-CreERT2* mice were crossed to *Ai14(RCL-tdT)-D* mice and tamoxifen (TAM) was administered to induce tdTomato expression. Different sets of adult mice received tamoxifen per os (p.o) for 3, 5 or 10 days and a set of neonatal mice received TAM for 3 days intraperitoneally (i.p). The mice were sacrificed for flowcytometry (FC) 7 days after the 3-day dosing paradigm or for immunofluorescence (IF) 9 or more days after dosing. **B-D**, Representative confocal micrograph showing tdTomato expression in IBA-positive microglia upon tamoxifen administration. **E-G**, Absence of tdTomato expression in untreated animals. **H-J**, Representative immunostaining for oligodendrocytes (H, Olig2, green), neurons (I, NeuN, green), and astrocytes (J, GFAP, green) in tdTomato-expressing microglia of *Tmem119-CreERT2*$^{+/-}$; *Ai14(RCL-tdT)-D*$^{+/-}$ mice. One of three independent experiments shown. **K and L,** Percentage completion **(K)** and fidelity **(L)** of the labeling in different brain regions for the different dosing schemes. Hpc = Hippocampus. CPu = Caudate-Putamen. Ctx = Cortex. N=2 mice for 3 days, 3 mice each for 5 and 10 days of TAM in adults, and 3 mice for 3 days administration at P2 = postnatal day 2. Floating bars = min to max, line at mean. **M,** Flow cytometry analysis of CD11b and CD45 expression in pre-gated single live CD45^{+} cells and tdTomato-expressing CD45^{+} cells of *Tmem119-CreERT2*$^{+/-}$; *Ai14(RCL-tdT)-D*$^{+/-}$ mice shown as overlay (I, black CD45^{+}, red CD45^{+} tdTomato^{+}). One of two representative experiments (N=3 mice). **N-O**, Confocal micrograph of the choroid plexus and adjacent parenchyma. **Q-S**, Confocal micrograph of CD31-immunostained blood vessels (green) shows tdTomato^{+} microglia (arrowheads) and tdTomato expression in a large blood vessel (open arrowhead). **T-V**, Confocal micrograph showing tdTomato expression in cortical microglia and cells of the pia (open arrowheads). **W-Z**, Confocal micrograph showing CD163- (white) and IBA1-expressing (green) macrophages. The open arrowhead indicates a tdTomato^{-}CD163^{+}IBA1^{+} perivascular macrophage. Closed arrowheads parenchymal microglia. One of three independent experiments shown (N=3 mice).

1.3.5 Characterization of transgene expression in monocytes from Tmem119 knock-in mice

Monocytes infiltrate the brain and contribute to pathology in a number of brain disorders. Currently widely used transgenic microglia lines also target monocytes in addition to microglia and cannot readily distinguish the two cell types, thus hampering unequivocal attribution of microglia function in these disorders. To assess the utility of *Tmem119* knock-in mice for investigating microglia in models of CNS disorders, we isolated blood monocytes and examined transgene expression (Figure 6A). Using flow cytometry on white blood cells isolated from control or *Tmem119-EGFP*$^{+/-}$ mice, we did not detect any EGFP-expression (Figure 6B-C). To further determine whether *Tmem119-CreERT2*$^{+/-}$; *Ai14*$^{+/-}$ mice display recombination in monocytes, we

administered tamoxifen and sacrificed the mice for analysis 7 days after the last dose (Figure 6D). Using flow cytometry on white blood cells, we found that about 3 percent of $CD45^+$ cells expressed tdTomato (Figure 6E-F). This suggests that there is a low level of CreERT2 activity in monocytes of the *Tmem119-CreERT* mice. Together, these data indicate high applicability of *Tmem119-EGFP* mice and good applicability of *Tmem119-CreERT2* mice to the study of brain disorders with potential monocyte contribution.

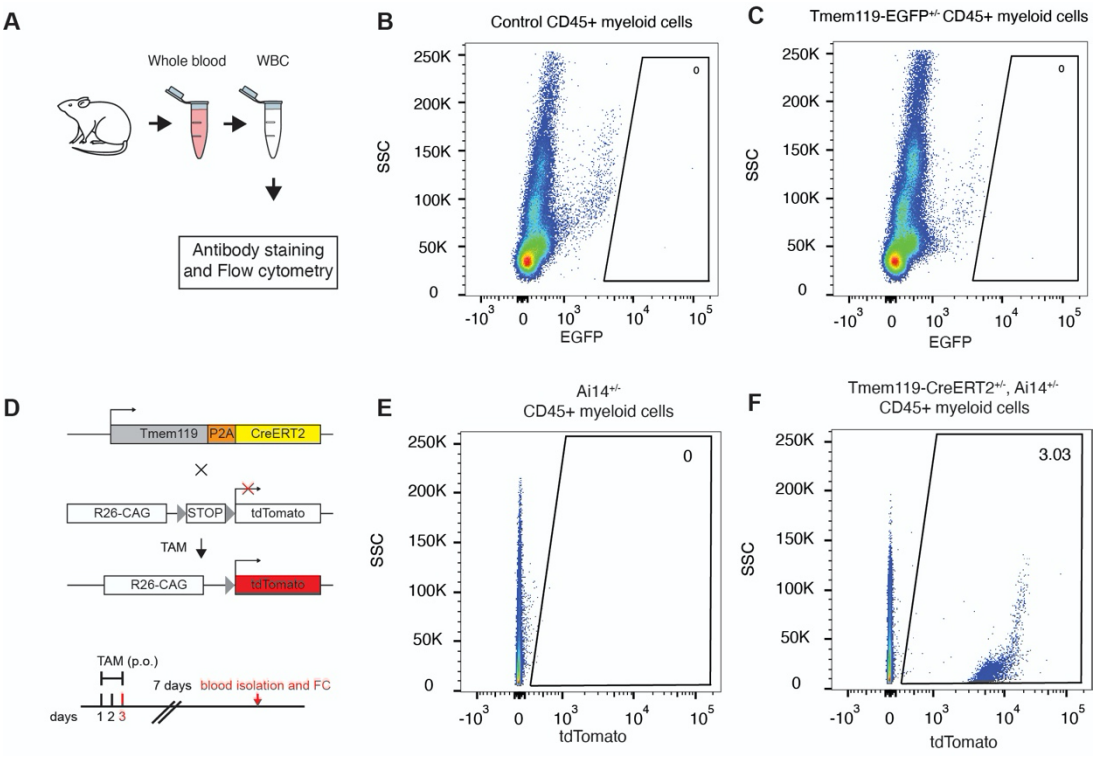

Figure 6: Blood monocyte profiling in Tmem119 knock-in mice

A, Experimental approach for flow cytometry of monocytes isolated from whole blood. **B and C,** Representative flow cytometry analysis of EGFP expression in pre-gated single live $CD45^+$ cells in wildtype control (B) and *Tmem119-EGFP*$^{+/-}$ mice (C). One of three experiments is shown (N=3 mice). Numbers in or adjacent to outlined areas indicate percent cells in each gate. **D,** Adult mice of *Tmem119-CreERT2*$^{+/-}$*; Ai14(RCL-tdT)-D*$^{+/-}$ mice received tamoxifen (TAM) per os (p.o) for 3 days. The mice were sacrificed 7 days after the last dose for flow cytometry (FC). **E and F,** Representative flow cytometry analysis of tdTomato expression in pre-gated single live $CD45^+$ cells in *Ai14(RCL-tdT)-D*$^{+/-}$ (E) and *Tmem119-CreERT2*$^{+/-}$*; Ai14(RCL-tdT)-D*$^{+/-}$ mice (F). One of two independent experiments is shown (N=3 mice).

1.4 Discussion

In this study, we addressed the critical need for transgenic mouse lines that specifically label or control microglia, but not other closely related cell types with overlapping signature gene expression (Bennett et al., 2016; Wieghofer and Prinz, 2016; Haimon et al., 2018). We targeted the recently identified microglia-specific *Tmem119* gene to knock in *EGFP* or *CreERT2*. Multiple analyses confirm correct insertion of the transgenes, intact expression of endogenous *Tmem119*, and normal basic morphology of microglia in the knock-in mice. Using immunofluorescence and flow cytometry approaches, we demonstrate that EGFP is expressed in microglia, but not other cells of the monophagocytic system defined anatomically and by signature protein expression. Flow cytometry further shows that EGFP is almost exclusively expressed in $CD11b^{+}CD45lo$ cells corresponding to microglia. We further provide evidence for early postnatal expression of EGFP and activity of CreERT2 in microglia upon tamoxifen administration. In addition, we show that blood monocytes do not express EGFP and display minimal activity of CreERT2. Together, our findings indicate proper generation of the two mouse lines, which are now readily available through a public repository (JAX#031823 for *Tmem119-EGFP* and JAX#031820 for *Tmem119-CreERT2*).

TMEM119 is a single transmembrane protein that is highly expressed in microglia in the brains of humans and mice (Bennett et al., 2016; Satoh et al., 2016). In this study, we opted to refrain from knocking *Tmem119* out through insertion of *EGFP* or *CreERT2* into the *Tmem119* ORF and instead chose to preserve expression by using a polycistronic knock-in approach with ribosomal skipping peptide P2A (Figure 1A). This was primarily motivated by the high expression levels of *Tmem119*, conservation of expression in microglia across species, and potential

developmental regulation patterns, all of which suggest the importance of this gene. Disruption of important genes in microglia could lead to confounding haploinsufficiency phenotypes, as previously shown for other transgenic microglia lines (Lee et al., 2010; Rogers et al., 2011). Our data rule out such potential confounding effects by showing intact *Tmem119* mRNA and protein expression (Figure 1E-G), as well as normal basic morphology of microglia in the knock-in mice (Figure 1H-M).

Examination of EGFP expression and co-expression analysis with TMEM119, IBA1, and CD163 revealed that EGFP labels only parenchymal microglia (Figures 2 and 3). Identification of these cells was possible by direct observation of EGFP fluorescence as well as by analysis of immunostaining-enhanced tissue sections, supporting the conclusion that EGFP expression levels are robust. Flow cytometry analysis further showed expression of EGFP in virtually all $CD11b^{+}CD45lo$ microglia (Figure 2N) and a minor fraction of 6.9 percent (153/2212) of $CD11b^{+}CD45int/hi$ cells (Figure 3G-I). This reflects that *Tmem119* expression is highly selective, but not completely restricted to microglia, which has been observed in recent single-cell sequencing studies (Li et al., 2019). An interesting observation was the expression of EGFP at early postnatal time points in microglia (P1, P3, and P6), but also endothelial cells of blood vessels at P1 (Figure 4). This is interesting for two reasons. First, it suggests that *Tmem119* is initially expressed in microglia and endothelial cells and only becomes a specific microglia marker during early postnatal development, presumably by selective up- and downregulation of expression in microglia and endothelial cells, respectively. Second, translational processing of *Tmem119* transcript appears to stand in opposition to a previous report showing that, while RNA sequencing detects *Tmem119* mRNA throughout development, immunostaining only identifies TMEM119 protein at later postnatal stages (Bennett et al., 2016). Although our data also do not directly show

TMEM119 protein expression at early stages, ribosomal processing of the transcript is at least indirectly implied by the presence of EGFP protein, suggesting TMEM119 protein might be expressed but undetected due to expression level, protein stability, differential posttranslational modification, or methodological limitations in immunostaining and flow cytometry. Together, these data indicate that *Tmem119* knock-in mice may enable the study of microglia and endothelial cells until postnatal day (P1) and microglia specifically after P3 and later.

Our experiments using *Tmem119-CreERT2*$^{+/-}$ Ai14(RCL-tdT)$^{+/-}$ mice show tdTomato expression in IBA1-expressing microglia, indicating that this line is suitable for Cre-dependent manipulation of genes and transgene expression in microglia without affecting other major neuronal or glial cell types in the CNS (Figure 5). In this particular experiment, we observed very high, dose-dependent recombination efficiencies close to 100 percent with a trend for slight reduction of the generally high specificity with increasing tamoxifen dosage (Figure 5K, L). The recombination efficiency observed across all doses compares well with other published models, such as the *Cx3cr1* mouse line (Goldmann et al., 2013), and might even permit shorter dosing paradigms dependent on the assay and relevant conditional allele. We further examined tissues other than parenchymal microglia and observed that recombination was largely yet not completely absent in choroid plexus macrophages (5N-P). This is consistent with reported endogenous TMEM119 expression and other reports in the literature, suggesting other brain macrophages may express microglia-specific genes at very low levels (Bennett et al., 2016; Goldmann et al., 2016; Mildner et al., 2017), which might be sufficient to cause occasional all-or-none recombination events. In addition, our data showed tdTomato expression in a few larger blood vessels and IBA1-negative cells in the pia (Figure 5Q-V). While we did not determine the precise cellular origin of this signal, our data from CD31-immunostaining exclude endothelial cells of the intracerebral

microvasculature (Figure 5Q-S). Together with the spatial extent of tdTomato expression and recent single cell RNA sequencing data of vascular cells, our observations point to leptomeningeal cells and their projections that penetrate deep into the brain ensheathing large blood vessels and the choroid plexus stroma (Decimo et al., 2012; Vanlandewijck et al., 2018). Together, these data render the *Tmem119-CreERT2* line a highly useful tool for the conditional study of microglia, while also suggesting potential application for leptomeningeal cells.

Examination of EGFP and tdTomato expression in blood monocytes of *Tmem119-EGFP* and *Tmem119-CreERT2; Ai14* mice revealed complete absence and minimal expression, respectively (Figure 6). While, the lack of EGFP expression in blood monocytes of the *Tmem119-EGFP* knock-in mice was expected based on previous observations, tdTomato expression in 3% blood monocytes of the *Tmem119-CreERT2; Ai14* mice was rather surprising. Similar to other brain macrophages discussed above, blood monocytes may express *Tmem119* at very low, almost undetectable levels, which may nonetheless be sufficient to cause occasional all-or-none Cre recombination events. Together, these data render the *Tmem119* knock-in lines powerful tools to investigate microglia in health and disease without significant confounds from monocyte contribution.

During the past decade, available microglia lines have been instrumental in advancing our understanding of microglia. These lines remain powerful tools to study microglia function. At the same time, it is widely acknowledged that ontogenetic differences, as well as differences in localization and microenvironment between parenchymal microglia and their closely related cells from the monophagocytic system warrant more discerning observation and manipulation (Bennett

et al., 2016; Wieghofer and Prinz, 2016; Haimon et al., 2018). Recently developed antibodies for TMEM119 immunostaining are one tool that has been adopted quickly to identify parenchymal microglia. As TMEM119 is a transmembrane protein localizing to processes, immunostaining for this protein is particularly powerful to study morphology of microglia. To identify discrete microglia, however, relatively diffuse staining patterns of membrane-bound TMEM119 present a challenge (Figure 2B). In this case, the more discretely identifiable cytosolic distribution of EGFP in the *Tmem119-EGFP* line might be of great value. In addition, the robustness of the EGFP signal in the *Tmem119-EGFP* line may enable cell sorting without the need for antibodies, possibly even at early developmental stages before the onset of TMEM119 appearance on the membrane, as well as *in vivo* imaging approaches. Furthermore, the absence of EGFP fluorescence in blood monocytes renders this line uniquely useful for the study of microglia in brain disorders that involve monocyte infiltration. The *Tmem119-CreERT2* line will significantly facilitate conditional control of gene expression selectively in microglia, especially in cases when monocytes, but not leptomeningeal cells, could likely confound interpretations. Compared to constitutive Cre lines, which cumulatively recombine throughout development and thus deny temporal control, the *CreERT2* line will allow precise control of gene expression to examine the role of microglia in temporally restricted developmental processes. In this capacity, dose-dependency of CREERT2 and potentially resulting mosaic expression of recombined alleles using low doses may allow the study of candidate genes in adjacent microglia populations sharing the same microenvironment. Beyond the application of *Tmem119*-knockin and other currently available mouse lines, genetic approaches such as targeting other microglia-signature genes, engineering highly specific artificial promoters and regulatory regions, and using intersectional split-Cre approaches hold great promise to produce even more specific tools to study microglia in the future.

2 Development of a Constitutively Active Cre Line for the Manipulation of Microglia

I generated *Fcrls-Cre* mice, designed and executed genotyping assays, as well as immunofluorescence staining, and flow cytometry assays of brain, peripheral organs, and white blood cells. Liang Li sliced peripheral organs and contributed to immunofluorescence staining. Nicholas Sanders assisted with mouse colony maintenance.

2.1 Abstract

Microglia carry out important functions as the resident macrophages of the brain. To study their role in health and disease, the research community needs tools to genetically modify them in a manner that distinguishes them from closely related cell-types, such as monocytes. While two currently available tamoxifen-inducible CreERT2 lines are able to achieve this, improved constitutively active Cre lines are much needed for studies where tamoxifen administration is contraindicated. In this study, I leverage the microglia-specific *Fcrls* gene to generate mice expressing constitutively active Cre. Genetic characterization of the targeted locus reveals correct positioning of the transgene in several founder animals. Immunofluorescence analysis of *Fcrls-Cre* mice crossed to a reporter demonstrates that parenchymal microglia express Cre, even at early embryonic time points. Further, analysis of organs shows that only low to modest numbers of peripheral macrophages display Cre activity. Finally, flow cytometric analysis demonstrates that virtually no white blood cell subsets display Cre activity in *Fcrls-Cre* mice, whereas a large fraction of cells within these subsets expresses Cre in the currently best available Cre line, *Cx3cr1-CreM* (MMRRC). This new transgenic line is an important addition to the microglia toolbox by providing the currently most specific constitutively active Cre line for studies where tamoxifen administration is contraindicated.

2.2 Introduction

Microglia are the resident macrophages of the brain (Lawson et al., 1990). Functionally, their phagocytic and secretory activities play a role in neurogenesis, development of neuronal connectivity, myelin maintenance, and survival of neurons (Stevens et al., 2007; Sierra et al., 2010; Paolicelli et al., 2011; Schafer et al., 2012; Ueno et al., 2013; Hagemeyer et al., 2017; Wlodarczyk et al., 2017; Weinhard et al., 2018). In addition, microglia react to perturbations such as vascular injury, multiple sclerosis lesions, and neurodegeneration (Itagaki et al., 1989; Davalos et al., 2005; Ransohoff, 2016; Aguzzi and Zhu, 2017; Keren-Shaul et al., 2017; Mathys et al., 2017; O'Loughlin et al., 2018). Dissecting the role of microglia in these processes hinges on mouse lines to conditionally delete genes in microglia. Currently, several transgenic lines are available that allow constitutive (Cre) or inducible (CreERT2) deletion of floxed sequences. For Cre lines, loci harnessed include *Tie2, Csf1r, Lyz2, Cx3cr1, Cx3cr1/Sall1* (Clausen et al., 1999; Kisanuki et al., 2001 p.2; Ferron and Vacher, 2005; Kim et al., 2006; Samokhvalov et al., 2007; Yona et al., 2013; Orthgiess et al., 2016 p.2). For CreERT2, the currently most faithful lines target *Tmem119, HexB, P2ry12*, or *Cx3cr1* (Parkhurst et al., 2013; Yona et al., 2013; Kaiser and Feng, 2019; Masuda et al., 2020; McKinsey et al., 2020). When using these lines to study microglia, there are two major considerations. One, current constitutively active Cre lines often recombine floxed alleles in additional major non-myeloid cell types, as well as unwanted myeloid cells, such as monocytes (Orthgiess et al., 2016; Haimon et al., 2018; Masuda et al., 2020). Two, the high fidelity CreERT2 lines require tamoxifen administration, which is a relative contraindication for developmental studies, studies of sex-specific effects and laboratories with limited access or facilities. Thus, a constitutively active Cre line that distinguishes microglia from other closely related peripheral and

central myeloid cells such as blood monocytes as well as peripheral macrophages would be a much wanted addition to the toolbox (Wieghofer and Prinz, 2016; Haimon et al., 2018).

Recently, profiling of genes enriched in microglia over other myeloid cells revealed several candidate genes for the generation of new Cre lines (Butovsky et al., 2014). Amongst these, Fc receptor- like S, scavenger receptor (*Fcrls*) is expressed across all microglia subsets based on single cell RNA sequencing studies (Hammond et al., 2019; Li et al., 2019). Adding to this, bulk RNA sequencing along development shows that *Fcrls* expression commences early during embryonic development (Mass et al., 2016). In contrast, *Fcrls* is not expressed monocytes and other peripheral immune cell subsets based on data collected at the ImmGen database (ImmGen.org). Together, these data render *Fcrls* a suitable target locus for the generation of a specific Cre line. Here, I report the generation and characterization of an *Fcrls-P2A-Cre* knock-in mouse line, where microglia express Cre. Using a cross to the Ai14 tdTomato reporter, I demonstrate that the mice display Cre activity in all microglia as early as E12.5, the earliest time analyzed. I further show that Cre is inactive in oligodendrocytes and neurons, and only modestly active in 10-20% of macrophages in peripheral organs. Most strikingly, studies of white blood cell subsets show that Fcrls-Cre is virtually inactive across all subsets, whereas the currently best available constitutively active Cre line, Cx1cr1-CreM, recombines floxed sequences at high rates. This new mouse line will soon be publicly available and expand the microglia toolbox by adding the currently most specific constitutively active Cre line.

2.3 Results

2.3.1 Generation of an *Fcrls-2A-Cre* Knock-in Mouse Using CRISPR/Cas9

Cre-driver lines and conditional alleles are critical in the quest for understanding the roles of microglia in health and disease. Several lines utilizing Cre or its inducible form CreERT2 were previously generated and are now widely used in research (Wieghofer and Prinz, 2016). However, the currently available mouse lines collectively have some drawbacks in two ways. First, tamoxifen must be administrated to CreERT2 lines, which is undesirable for the study of early development, sexually dimorphic biology, difficult to recombine floxed alleles requiring high Cre concentration, or laboratories with limited tamoxifen or hazmat facility access. Second, existing constitutively active Cre lines recombine floxed alleles in monocyte, which is a major confounding factor depending on the biology. Given these drawbacks, availability of a sensitive and specific Cre line would facilitate microglia research. Amongst a group of recently discovered microglia-specific genes, *Tmem119* was initially chosen to generate a *Tmem119-2A-Cre* mouse line (Bennett et al., 2016; Kaiser and Feng, 2019). This mouse line, however, displayed widespread Cre activity in endothelial cells (Kaiser and Feng, unpublished findings). It was therefore not further developed. Instead, *Fcrls* was chosen for knock-in of Cre due to its high expression across all microglia subsets and complete absence of expression in monocytes (Hammond et al., 2019), ImmGen.org). To generate *Fcrls-2A-Cre* mice, a double-strand DNA targeting vector containing *2A-Cre*, 1.5 kb homology arms, and an additional PAM point-mutation was created and injected into mouse Zygotes together with three pre-screened crRNAs (Figure 7). This design inserts *2A-Cre-STOP* into the STOP codon of *Fcrls*, resulting in a single transcript that encodes both *Fcrls* and *Cre* by means of ribosomal skipping. Zyogtes were implanted into surrogates, which resulted in 14 live births. To determine which of the 14 live births harbor 2A-Cre correctly inserted at the

Fcrls locus, primer pairs were chosen with binding sites outside the homology arms and inside the transgene to generate amplicon uniquely present in mice with correct knock-in (Figure 7A). Four of the 14 mice allowed generation of this amplicon, indicating that the 2A-Cre sequence was correctly placed (Figure 7B). These bands were extracted and Sanger sequenced to verify intactness of the genomic sequence (Figure 7C). Besides insertion of 2A-Cre-STOP and the disruption of the STOP codon preceding this sequence, the only change was the PAM mutation in the 3'UTR, which was inserted on the targeting vector to avoid CRISPR/Cas-mediated cutting of the targeting vector (Figure 7C). Two of the four founder animals, namely 11814 and 11820 were crossed to C57BL/6J to generate F1 animals, and genomic sequences in F1 animals were again confirmed by Sanger sequencing. Together, these data show that Fcrls-2A-Cre, hereafter referred to as *Fcrls-Cre* for simplicity, mice were successfully generated.

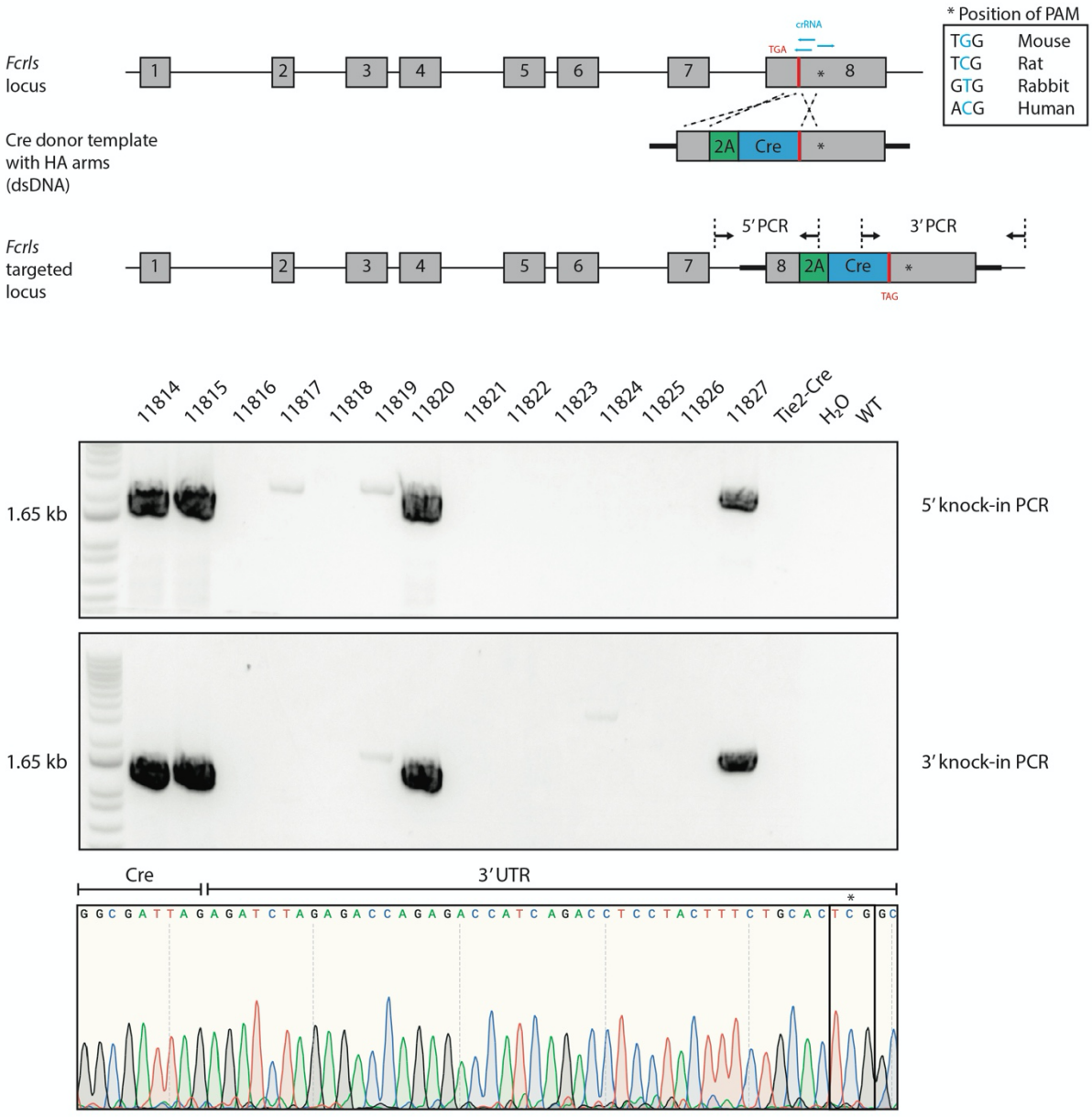

Figure 7 Generation of an Fcrls-2A-Cre Knock-in Mouse Using CRISPR/Cas9.

A, Knock-in approach to insert a 2A-Cre cassette into the stop codon of *Fcrls* in exon 8. Three crRNAs were selected to introduce double strand breaks at the stop codon and in the 3' UTR. The 3' UTR was selected such that mutation of the NGG PAM alters a non-conserved nucleotide (inset box). PCR primers to check for correct insertion are indicated as arrows. **B-C**, Representative agarose gel electrophoresis image of the indicated 5' and 3' PCR amplicons across several live births after zygote injection (11814-11827). **D**, Sanger sequencing trace of 3' amplicon showing the G->C mutation in the founder animals.

2.3.2 *Fcrls-Cre* mice Recombine Floxed DNA in Microglia Effectively and Specifically

Fcrls-Cre mice were successfully created based on genomic analysis. To probe the activity of Cre recombinase across tissues and cell types, *Fcrls-Cre* mice were crossed to Ai14 tdTomato mice, which report recombination with tdTomato fluorescence (Madisen et al., 2010, Figure 8A). *Fcrls-Cre; Ai14* mice were perfused at postnatal day 7 and prepared for immunofluorescence staining of several regions (Figure 8B). High power confocal micrographs in the cortex showed that parenchymal IBA1-positive microglia expressed tdTomato (Figure 8C-E). In the same micrograph, it is also apparent that IBA1-expressing myeloid cells in the meninges express tdTomato (Figure 8C-E). Similarly, confocal micrographs in the corpus callosum show that all microglia there, including highly ameboid microglia that presumably belong to the axon tract-associated subset of microglia express tdTomato (Figure 8F-H). Adjacent to these microglia, tdTomato expression can be seen in IBA1-expressing choroid plexus macrophages (Figure 8F-H). In the cerebellum, both IBA1-expressing microglia located in the white-matter and gray-matter express tdTomato (Figure 8I-K). Finally, in the spinal cord, parenchymal IBA1-positive microglia express tdTomato, whereas myeloid cells in the pia appear to be tdTomato-negative (Figure 7L-N). These confocal micrographs were quantified as the completion (fraction of $IBA1^+$ parenchymal microglia expressing tdTomato) and fidelity (fraction of $tdTomato^+$ cells being parenchymal $IBA1^+$ microglia). It was found that parenchymal microglia were completely labeled and all labeled cells in the parenchyma were microglia (Figure 8O, P). To further examine the specificity and rule out any expression in non-myeloid cell types, slices were stained against OLIG2 (oligodendrocyte lineage cells) and NEUN (neurons). Confocal micrographs revealed that neither $OLIG2^+$ nor $NEUN^+$ cells expressed tdTomato (Figure 8Q-W). Together, these data show that Fcrls-Cre mice recombine floxed DNA sequences with high efficiency and specificity in microglia. The data demonstrate that while no non-myeloid cells in the brain express Cre, border-associated macrophages in the meninges and choroid plexus do.

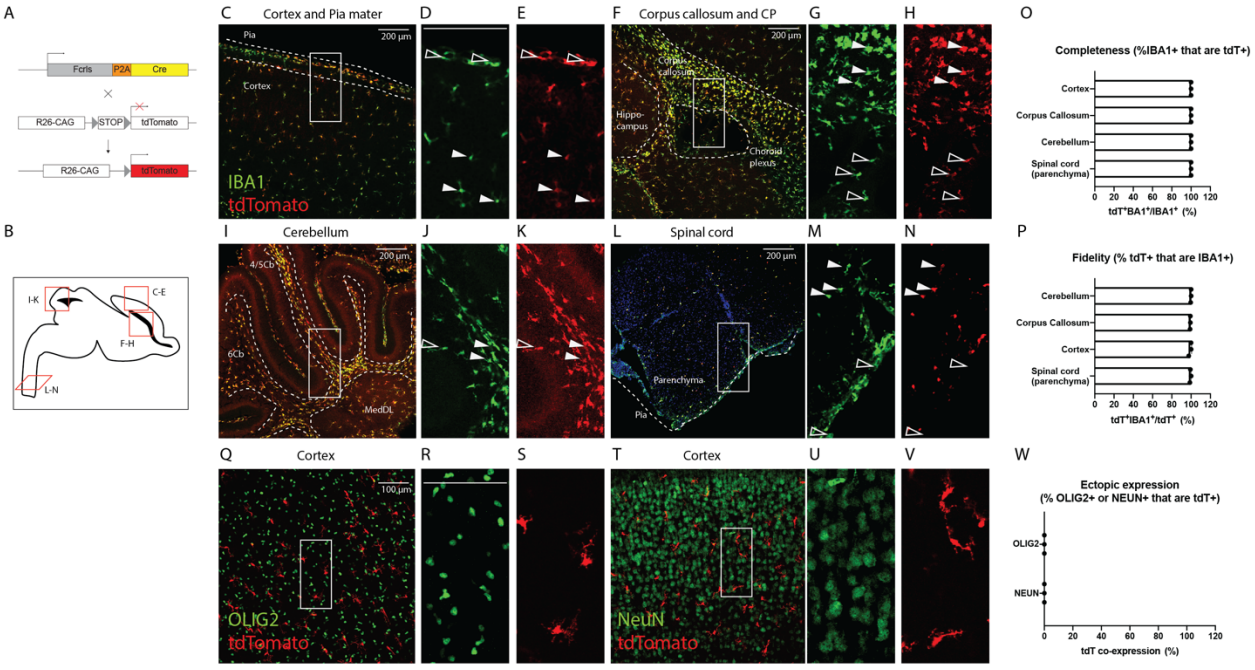

Figure 8 ***Fcrls-Cre*** **mice Recombine Floxed DNA in Microglia Effectively and Specifically. A**, Schematic of experiment to probe Cre activity. *Fcrls-Cre* mice were mated to Ai14 tdTomato reporter mice and analyzed at postnatal day 7. Cre activity is reported by tdTomato fluorescence. **B,** Schematic of sagittal brain slice and annotation of areas imaged. **C-E**, Representative confocal micrograph of IBA1-immunofluorescence staining in cortex and pia mater. Solid arrowheads in magnifications: tdT tomato in parenchymal microglia. Open arrowheads: tdTomato in IBA1$^+$ myeloid cells located in the meninges. **F-H**, Representative confocal micrograph of IBA1-immunofluorescence staining in corpus callosum and choroid plexus. Solid arrowheads in magnifications: tdT tomato in parenchymal microglia. Open arrowheads: tdTomato in IBA1$^+$ myeloid cells located in the choroid plexus. **I-K**, Representative confocal micrograph of IBA1-immunofluorescence staining in the cerebellum. Solid arrowheads in magnifications: tdT tomato in white-matter microglia. Open arrowheads: tdTomato in gray-matter microglia. **L-N**, Representative confocal micrograph of IBA1-immunofluorescence staining in the spinal cord. Solid arrowheads in magnifications: tdT tomato in parenchymal microglia. Open arrowheads: tdTomato in IBA1$^+$ myeloid cells in the pia. **O-P**, Quantification of the completion and fidelity of Cre activity in IBA1$^+$ parenchymal macrophages in the CNS. **Q-V**, Representative confocal micrograph of OLIG2- or NEUN-immunofluorescence staining in the spinal cord for cells of the oligodendrocyte or neuron lineages. **W**, Quantification of Cre activity in OLIG2- or NEUN-immunostaining-positive cells.

2.3.3 *Fcrls-Cre* mice Recombine Floxed DNA in Microglia in the Embryonic Brain

As the first glia to enter the brain, microglia play an important role during embryonic brain development and disruption of microglia during this time by maternal inflammation is linked to developmental impairments (Thion et al., 2018b, 2018a). To test whether the *Fcrls-Cre* line is suitable for conditional deletion of floxed genes during embryonic development, timed mating was set up for *Fcrls-Cre* mice with *Ai14 tdTomato* reporter mice. Embryos were harvested at E12.5 and prepared for immunofluorescence staining by slicing coronally to expose cortex, choroid plexus, medium ganglionic eminence (MGE), and lateral ganglionic eminence (LGE) (Figure 9A, B). High power confocal micrographs showed that $IBA1^{+}$ expressing microglia across these regions express tdTomato (Figure 9C-M). In addition, choroid plexus macrophages also express tdTomato (Figure 9K-M). Together, these data demonstrate that the *Fcrls-Cre* mouse line is suitable for recombination of conditional alleles in microglia during embryonic development.

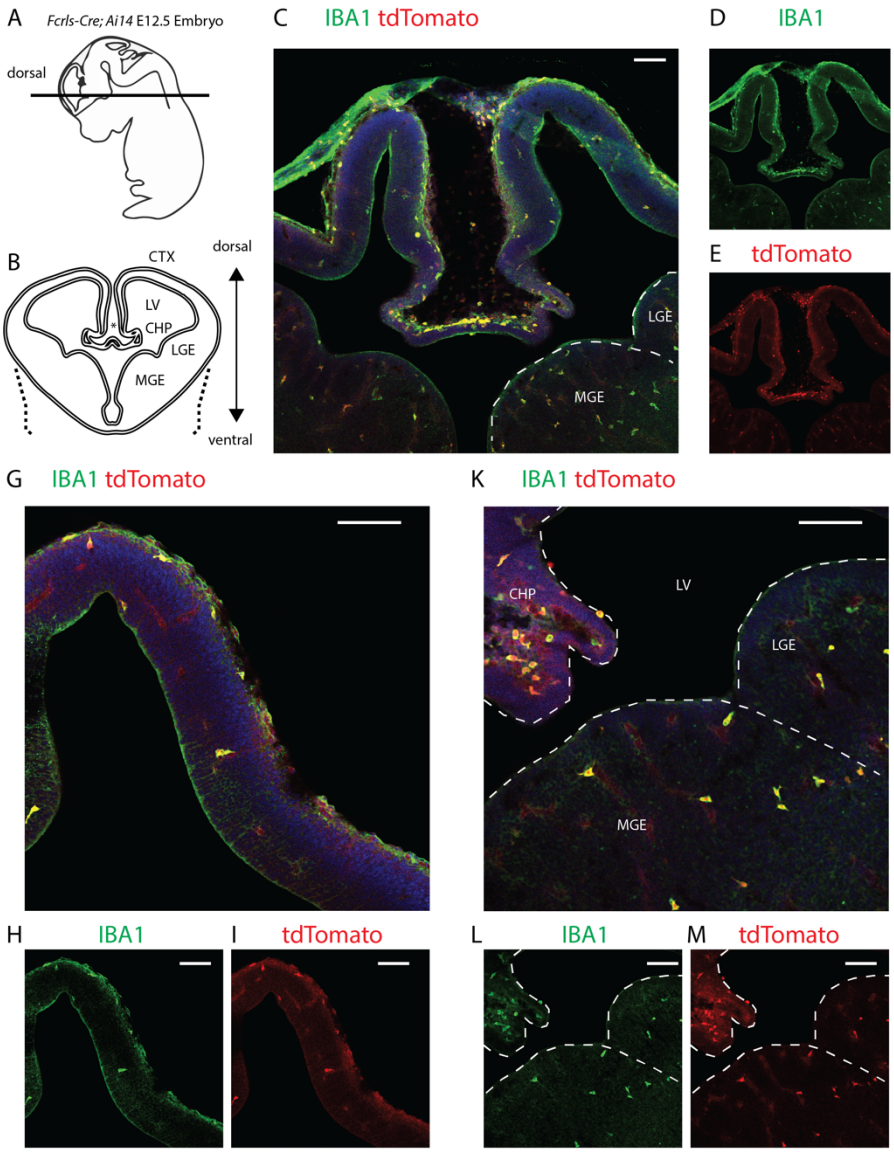

Figure 9 *Fcrls-Cre* mice Recombine Floxed DNA in Microglia in the Embryonic Brain. A, Schematic of experiment to probe Cre activity in *Fcrls-Cre; Ai14* E12.5 embryos. Sagittal view of whole embryo which was coronally sectioned as indicated. **B,** Schematic of coronal brain slice and annotation of areas imaged. CTX cortex, CHP choroid plexus, LGE lateral ganglionic eminence, LV lateral ventricle, MGE medium ganglionic eminence. **C-E**, Representative confocal micrograph of IBA1-immunofluorescence staining in cortex, MGE, and LGE. **G-M**, Magnified view of cortex, MGE, and LGE confocal micrographs. Experiment representative of two E12.5 embryos from one litter.

2.3.4 *Fcrls-Cre* mice Recombine Floxed DNA in a Fraction of IBA1-expressing cells in Peripheral Tissues

Fcrls is highly enriched in microglia compared to other myeloid cells (Butovsky et al., 2014), but even minute amounts of Cre can lead to all-or-none recombination events of floxed genomic sequences. To probe whether peripheral macrophages display Cre activity in *Fcrls-Cre* mice, peripheral organs were collected, stained, and imaged from *Fcrls-Cre; Ai14* tdTomato reporter mice at postnatal day 7. Across several of these organs, including liver, large intestine, thymus, heart, and small intestine, tdTomato expression was observed (Figure 10A-E). The highest colocalization of tdTomato and IBA1 immunofluorescence staining was observed in the liver ~30%, whereas below 10% of small and large intestine macrophages expressed tdTomato. In sum these results suggest that *Fcrls-Cre* displays Cre activity in a fraction of about 10-30% of peripheral macrophages.

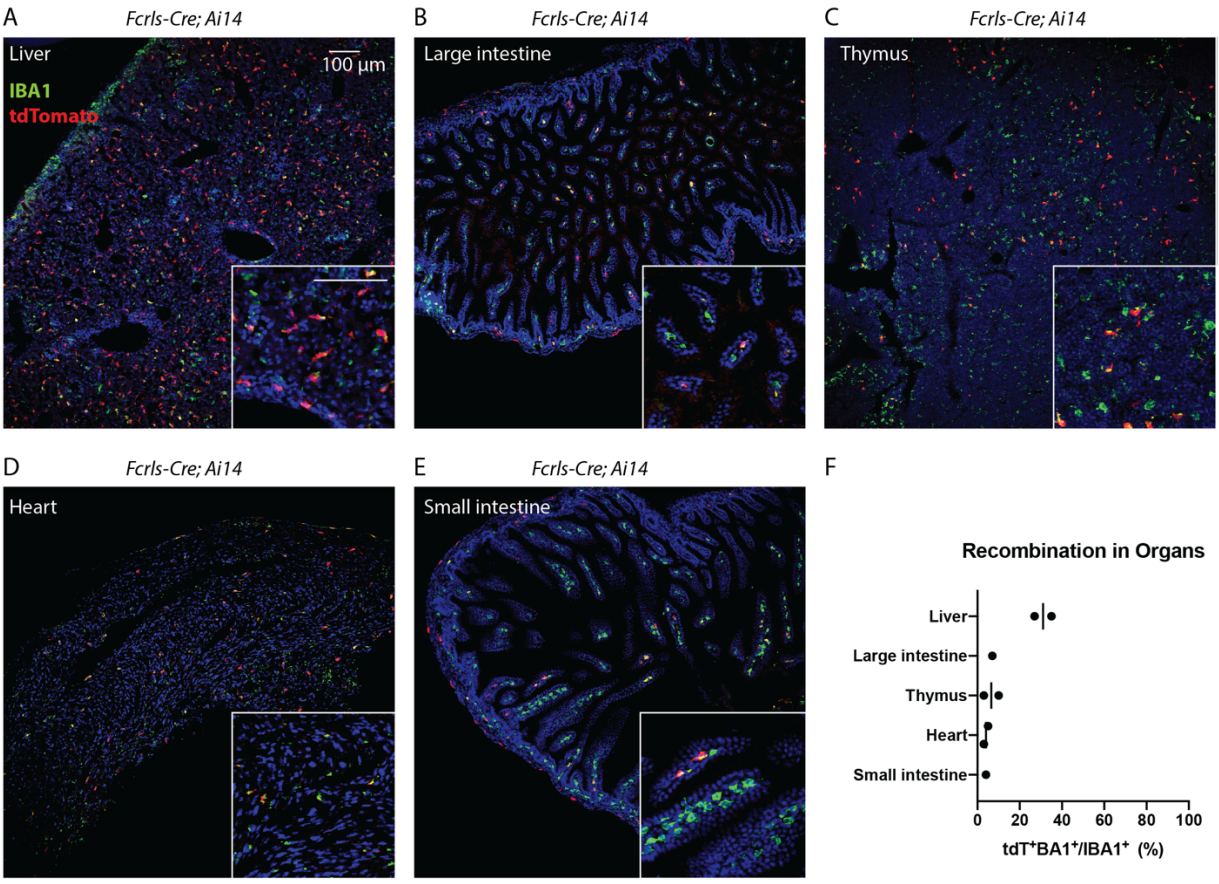

Figure 10 *Fcrls-Cre* mice Recombine Floxed DNA in a Fraction of IBA1-expressing cells in Peripheral Tissues. **A**, Representative confocal micrograph of tdTomato expression as surrogate for Cre activity in *Fcrls-Cre; Ai14* P7 liver. **B,** Confocal micrograph of tdTomato expression as surrogate for Cre activity in *Fcrls-Cre; Ai14* P7 large intestine. **C,** Representative confocal micrograph of tdTomato expression as surrogate for Cre activity in *Fcrls-Cre; Ai14* P7 large thymus. **D,** Representative confocal micrograph of of tdTomato expression as surrogate for Cre activity in *Fcrls-Cre; Ai14* P7 heart tissue. **E,** Confocal micrograph of tdTomato expression as surrogate for Cre activity in *Fcrls-Cre; Ai14* P7 small intestine. **F**, Quantification of Cre activity in IBA1-immunostaining-positive cells in peripheral organs.

2.3.5 *Fcrls-Cre* Mice Spare Floxed DNA in White Blood Cells Completely

Monocytes infiltrate the brain mediate pathological events in stroke, Alzheimer's disease, and multiple sclerosis (Henderson et al., 2009; Ritzel et al., 2015; Shang et al., 2016). Recently developed CreERT2 lines including *Tmem119-CreERT2* and *P2Ry12-CreERT2* almost completely avoid recombination of floxed alleles in monocytes (Kaiser and Feng, 2019; McKinsey et al.,

2020). For constitutively active Cre lines, however, the currently best available line, *Cx3cr1-CreM* (MMRRC, Gong et al., 2010; Zhao et al., 2019), is expected to express Cre in monocytes and perhaps other white blood cells based on the endogenous expression profile of *Cx3cr1* (ImmGen.org). This inability to discern the two cell types impedes unequivocal attribution of microglia function in these disorders when using this line. To test whether *Fcrls-Cre* displays Cre activity in leukocyte subsets, white blood cells were harvested from adult *Ai14* control mice, *Fcrls-Cre; Ai14* mice or *Cx3cr1-CreM; Ai14* mice and stained for flow cytometry (Figure 11A). Using flow cytometry, single, live, CD45-expressing cells were further analyzed and parsed into CD3e/CD19^{+} lymphocytes, CD11b^{+}Ly6G^{+} granulocytes, and CD115^{+}Ly6C^{hi} and CD115^{+}Ly6C^{lo} monocytes (Figure 11B-H). Leukocytes from *Ai14* mice were analyzed as controls to set the threshold for tdTomato expression. Histograms of tdTomato expression showed that while different leukocyte subsets in *Cx3cr1-CreM; Ai14* mice express tdTomato, virtually no tdTomato expression was detected in leukocytes from *Fcrls-Cre; Ai14* mice (Figure 11I-L). Quantification showed that 0% of CD3e/CD19^{+} lymphocytes, 0% of CD11b^{+}Ly6G^{+} granulocytes, and 0% of CD115^{+}Ly6C^{hi} monocytes and 0% of CD115^{+}Ly6C^{lo} monocytes expressed tdTomato compared to 4.5%, 2.2%, 77%, and 97% of these cells in *Cx3cr1-CreM; Ai14* mice, respectively (Figure 11M-P). Together, these data demonstrate that, unlike the *Cx3cr1-CreM* line, the *Fcrls-Cre* line avoids undesirable Cre recombinase activity in white blood cells, especially monocytes.

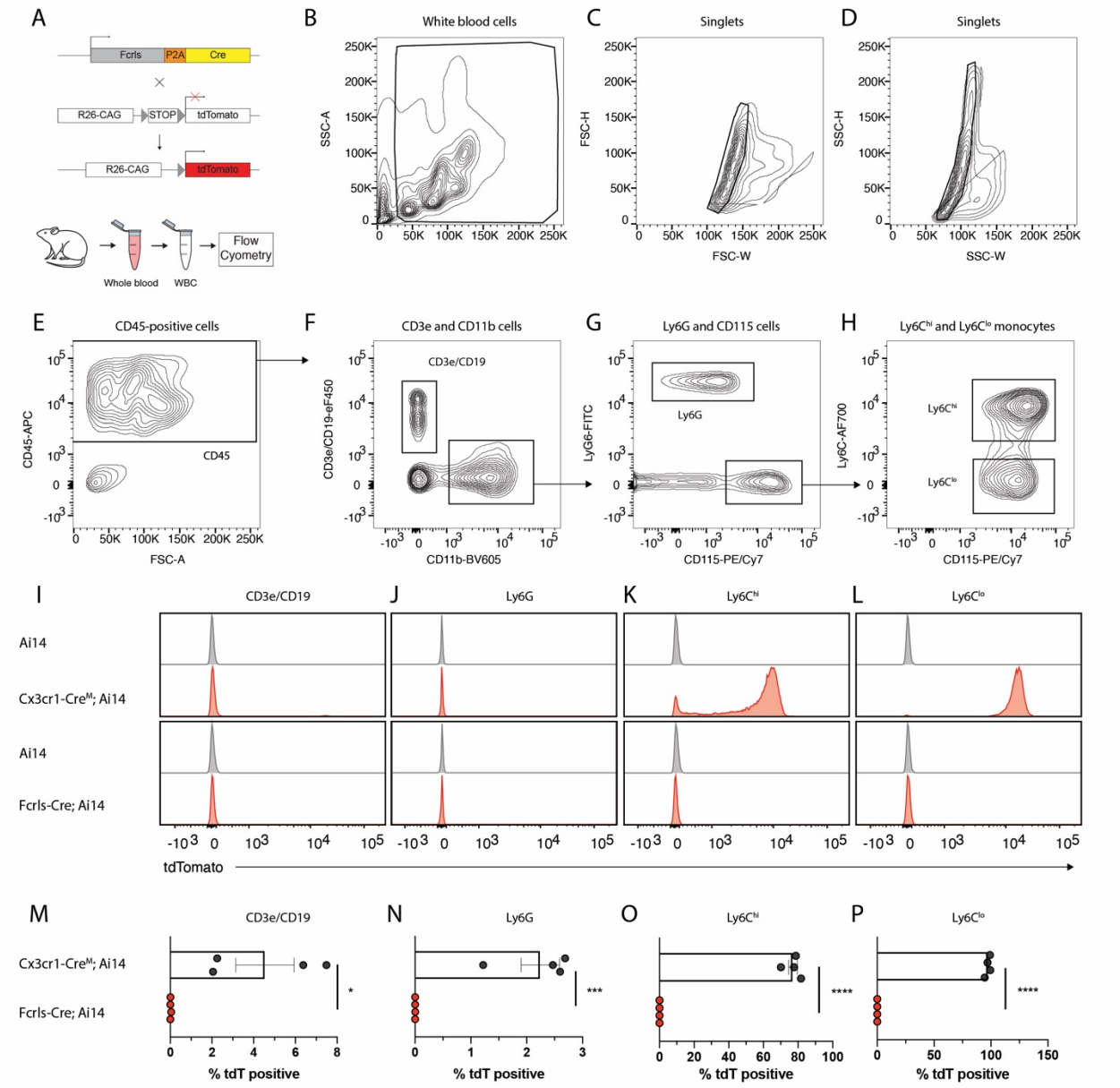

Figure 11 ***Fcrls-Cre*** **Mice Spare Floxed DNA in White Blood Cells Completely. A**, Schematic of experiment to probe Cre activity. *Fcrls-Cre* mice were mated to Ai14 tdTomato reporter mice and analyzed at adult age. Cre activity is reported by tdTomato fluorescence. Whole blood was collected, red blood cells lysed, and white blood cells (WBC) stained for flow cytometry. *Cx3cr1-Cre^{M}; Ai14* mice were used for comparison **B-E,** Flow cytometry density plots showing gating strategy for single, live, CD45-positive white blood cells. **F-H**, Flow cytometry density plots showing gating for CD3e/CD19^{+} lymphocytes, CD11b^{+}Ly6G^{+} granulocytes, and CD115^{+}Ly6C^{hi} and CD115^{+}Ly6C^{lo} monocytes. **I-L** Histograms showing tdTomato fluorescence among the different white blood cell subset populations for *Ai14* controls, *Cx3cr1-Cre^{M}; Ai14* mice, and *Fcrls-Cre; Ai14* mice. **M-P** Scatter plots showing the percentage of tdTomato-positive cells amongst all cells within a given subset in *Cx3cr1-Cre^{M}; Ai14* mice, and *Fcrls-Cre; Ai14* mice. N=4 mice each. *p=0.0178, ***p=0.0006, ****p<0.0001.

2.4 Discussion

Transgenic mouse lines enabling the conditional deletion of floxed target genes are critical for the study of microglia and additional constitutively active Cre lines that spare immune cells in the periphery and white blood cells would be a great addition to the toolbox. This study addressed this need by creating an *Fcrls-P2A-Cre* mouse line. I show that injecting zygotes with CRISPR/Cas9 and a *P2A-Cre*-containing repair template targeting the stop codon of *Fcrls* resulted in several live births with in-frame placed transgene. Using an Ai14 reporter strain and immunostaining, I further demonstrate that the *Fcrls-P2A-Cre* line effectively and specifically recombines floxed alleles in microglia across several brain regions and the spinal cord. Further studies with the same reporter show that recombination occurs early in development and that a fraction of tissue-resident macrophages in some peripheral tissues exhibit Cre activity as well. Finally, utilizing flow cytometric analysis, I show that Cre activity is virtually nonexistent in different white-blood cell subsets.

Fcrls is one of the most highly expressed genes in microglia (Hammond et al., 2019), but its function remains unknown, since mice lacking *Fcrls* appear to be normal (Kaiser and Butovsky, personal communication). In this study, I nonetheless opted for a bicistronic knock-in approach using 2A peptide aiming to preserve endogenous expression and potential function of *Fcrls*. Besides insertion of the exogenous *2A-Cre* sequence, development of the mice further required insertion of a point mutation at the PAM site of one of the CRISPR guide RNAs to prevent cutting of the targeting vector or targeted allele (Figure 7). While the functional consequence of changing a base in the 3'UTR is unknown and difficult to predict, the base was chosen based on lack of conservation in rats, rabbits, and humans. *Fcrls-P2A-Cre* mice are healthy and do not display any overt abnormalities, but further studies are needed to test whether *Fcrls* transcript or protein are

reduced and whether the mice display more subtle abnormalities on the morphological or transcriptional level.

My studies using Ai14 reporter mice display that *Fcrls-P2A-Cre* mice recombine floxed alleles efficiently and with high fidelity at two different time points examined (Figures 8 and 9). The high completeness observed in the cortex, corpus callosum, and cerebellum is well in line with *Fcrls* expression based on scRNA sequencing and *in-situ* hybridization studies (Hammond et al., 2019; Li et al., 2019). Also in line with these sequencing studies, I observed recombination in border-associated macrophages such as those in the choroid plexus (Figures 8 and 9). Similar, albeit sparser activity has been reported in the currently most specific inducible Cre lines *Tmem119-CreERT2, P2ry12-CreERT2*, and *Hexb-CreERT2* based on endogenous expression pattern and experimental data (Kaiser and Feng, 2019; Masuda et al., 2020; McKinsey et al., 2020). Further, *Cx3cr1-CreM* (MMRRC, Gong et al., 2010; Zhao et al., 2019), the currently available best constitutively active Cre is active in these border-associated macrophages. While perivascular and meningeal macrophages were not examined in *Fcrls-P2A-Cre* mice in detail, the spatial extent of labeling indicates that they most likely display Cre activity (Figures 8 and 9). Further detailed studies using co-labeling with specific markers for these cells in immunofluorescence staining or flow cytometry are hence warranted. With respect to temporal activity of Cre, studies at embryonic day 12.5 revealed activity before this stage (Figure 9), which renders this line suitable for studies during early development. Similar activity has not been shown for the *Cx3cr1-CreM* line yet and given that scRNA sequencing data shows less consistent expression of this gene (Hammond et al., 2019; Li et al., 2019), a head-to-head comparison using reporter mice is warranted.

Examination of Cre activity in peripheral organs revealed that floxed alleles are recombined in a fraction of tissue-resident macrophages in the intestine, liver, thymus, and heart (Figure 10).

Using the comparatively sensitive Ai14 reporter, recombination was observed in 10-20% of these macrophages, which is much lower than that seen in *Cx3cr1-CreM* mice. While recombination in even a subset of tissue-resident macrophages may appear surprising given the absence of *Fcrls* expression in adult peripheral macrophages (ImmGen.org), it is plausible based on transient *Fcrls* expression seen in some tissues at low to moderate levels during development (Mass et al., 2016). In such tissues with macrophages that turn over slowly, even low expression of Cre is sufficient for all-or-none recombination events. In sum, these data suggest that *Fcrls-P2A-Cre* is particularly suitable when early and efficient Cre activity is sought while spurious activity in some peripheral tissue-resident macrophages is acceptable.

Finally, and most significantly, my flow cytometric studies show that Cre is virtually inactive in white blood cells (Figure 11). This observation is important when studying disease models since infiltration of monocytes is common in CNS diseases (Henderson et al., 2009; Ritzel et al., 2015; Shang et al., 2016). A frequently used work-around using inducible lines that display Cre activity in monocytes is to induce recombination with tamoxifen and wait for monocyte turnover, which generally suitable for lineage tracing. However, the approach leaves ambiguity in disease contexts where monocytes with recombined alleles may at least partially drive pathology before getting turned over. Compared to other lines, *Fcrls-P2A-Cre* mice offer unique advantages. The currently best constitutively active Cre line *Cx3cr1-CreM* labels a large fraction of monocytes and a small fraction of lymphocytes and neutrophils (Figure 11) and other lines that achieve similar specificity, namely *P2ry12-CreERT2* and *Tmem119-CreERT2*, require tamoxifen administration (Kaiser and Feng, 2019; McKinsey et al., 2020). One limitation of the studies in *Fcrls-P2A-Cre* mice is that they were carried out in healthy adult animals. Moving forward, testing additional time points, and performing studies in disease context will add additional insights. Taken together, the attribute of

Fcrls-P2A-Cre mice to spare monocytes and other white blood cells renders this line extraordinarily suitable for studies where constitutive activity of Cre is desired and where monocytes would be a major factor confounding interpretation.

Fcrls-P2A-Cre mice present an exquisite addition to the microglia toolbox. In the future, more and even better constitutively active Cre lines may be developed. Most recently, *Cx3cr1* and *Sall1* loci were harnessed to create a split Cre mouse line, which displays impressive fidelity (Kim et al., 2021). At the same time, implementation of this line for knockout studies is hampered by its inefficiency that requires breeding of two loci to homozygosity in addition to the homozygous floxed allele for efficient knockout. Perhaps, a better combination for a split Cre approach achieving similar specificity while retaining high efficiency might be targeting *P2ry12* and *Fcrls* on the same allele on chromosome 3. This would facilitate breeding and genetic crosses of the mice. Moving forward, combining these improved mouse lines with emerging strategies to deliver genetic material to microglia, research into microglia function in health and disease will be much facilitated.

3 Development of an Easy-to-Use Software for the Quantification of Myelin *g*-ratio

I conceived and oversaw the project with Minqing Jiang, Harrison Allen, and Guoping Feng. I prepared and imaged tissues for electron microscopy of the corpus callosum. I benchmarked the software against manual tracing. I wrote the manuscript with input from all authors. Harrison Allen wrote the software. Minqing Jiang and Ohyoon Kwon contributed to the benchmarking of the software. Special thanks to Boaz Barak, Jing Wang, and Zhigang He for contributing additional electron micrographs for the benchmarking and testing of the software.

This chapter was previously published by Tobias Kaiser, Harrison Allen, Ohyoon Kwon, Boaz Barak, Jing Wang, Zhigang He, Minqing Jiang, and Guoping Feng in eNeuro: 30 June 2021, ENEURO.0558-20.2021; DOI: https://doi.org/10.1523/ENEURO.0558-20.2021

3.1 Abstract

In the central and peripheral nervous systems, the myelin sheath promotes neuronal signal transduction. The thickness of the myelin sheath changes during development and in disease conditions like multiple sclerosis. Such changes are routinely detected using electron microscopy through *g*-ratio quantification. While *g*-ratio is one of the most critical measurements in myelin studies, a major drawback is that *g*-ratio quantification is extremely laborious and time-consuming. Here, we report the development and validation of MyelTracer, an installable, stand-alone software for semi-automated *g*-ratio quantification based on the Open Computer Vision Library (OpenCV). Compared to manual *g*-ratio quantification, using MyelTracer produces consistent results across multiple tissues and animal ages, as well as in remyelination after optic nerve crush, and reduces total quantification time by 40-60%. With *g*-ratio measurements via MyelTracer, a known hypomyelination phenotype can be detected in a Williams Syndrome mouse model. MyelTracer is easy to use and freely available for Windows and Mac OS X (https://github.com/HarrisonAllen/MyelTracer).

3.2 Introduction

The myelin sheath is essential for proper neuronal functions in central and peripheral nervous systems. Oligodendrocytes and Schwann cells produce the myelin sheath through lamellar enwrapping of axons (Simons and Trotter, 2007; Salzer, 2015; Hughes and Appel, 2016; Stadelmann et al., 2019). The myelin sheath insulates axons, thereby preserving axonal integrity and promoting neuronal signal transduction (Sherman and Brophy, 2005; Nave, 2010). Under physiological conditions, changes in myelin contribute to behaviorally relevant neural plasticity mechanisms and experience-dependent sensory adaptations (Gibson et al., 2014; McKenzie et al., 2014; Hughes et al., 2018).

Abnormal changes in myelin are prominent features of many clinical pathologies. Ultrastructural myelin abnormalities, such as hypomyelination, myelin degeneration, and tomaculi, are cardinal features of prototypic white-matter diseases like multiple sclerosis, Pelizaeus Merzbacher disease, and Charcot-Marie-Tooth disease (Krajewski et al., 2000; Sander et al., 2000; Franklin and ffrench-Constant, 2008; Lin and Popko, 2009; Duncan and Radcliff, 2016). In addition, myelin abnormalities have recently been discovered as common features of neurodevelopmental disorders, including Pitt Hopkins Syndrome, Rett Syndrome, autism spectrum disorders (ASDs), and William's Syndrome (Zhao et al., 2018; Barak et al., 2019; Phan et al., 2020).

In both preclinical and clinical settings, pathological myelin abnormalities are often identified by studying myelin ultrastructure. Specifically, researchers use *g*-ratio as a metric for the relative thickness of the myelin sheath in cross-sectional micrographs (Rushton, 1951). Since manual myelin tracing is a major bottleneck in *g*-ratio quantification, tools that streamline this

process will tremendously facilitate future studies investigating activity-dependent homeostatic and pathological changes to the myelin sheath.

Several non-automated, semi-automated, and fully automated toolboxes are currently available. They include *G-ratio for ImageJ, AxonSeg,* and *AxonDeepSeg* (Goebbels et al., 2010; More et al., 2011; Bégin et al., 2014; Zaimi et al., 2016, 2018; Janjic et al., 2019). Collectively, these tools have facilitated different quantitative measurements of myelin ultrastructure, such as the number of axons and *g*-ratio. However, the current tools with more automation impose difficult requirements on their users, such as pre-processing data or modifying parameters by writing code. These drawbacks have impeded the tools' widespread adoption by the scientific community. We identified four major requirements of an open access toolbox that would significantly facilitate myelin analyses: (1) an intuitive graphical user interface that can be installed and used without running code, (2) consistent quantification results compared to manual analysis, (3) significantly less time-consuming, and (4) well-organized output data files and overlay images for publication and post-hoc quality control.

Here we report the development and validation of MyelTracer, an easy-to-use software that fulfills these critical requirements. Built using OpenCV and PyQt5's GUI toolkit, MyelTracer replaces the manual tracing of axons and myelin with semi-automated, threshold-dependent outlining. Compared to manual quantification, semi-automated quantification of axon diameters and *g*-ratio via MyelTracer produces consistent results across several tissues and developmental time points while reducing total quantification time by 40-60% depending on the region. Furthermore, using *g*-ratio measured with MyelTracer, we can detect a known hypomyelination phenotype in a Williams Syndrome mouse model, as well as in remyelination after optic nerve crush, indicating the applicability of MyelTracer for studies in disease contexts. To ensure

MyelTracer's all-in-one output functionality, we included a manual tracing function and counters for quantification of abnormally shaped sheaths and fraction of myelinated axons, respectively. MyelTracer is a valuable tool for the study of myelin ultrastructure and is freely available to the public as an installable software for Mac and PC https://github.com/HarrisonAllen/MyelTracer.

3.3 Results

3.3.1 MyelTracer is a semi-automated software using computer vision

G-ratio quantification requires measuring the cross-sectional areas of axons and myelin sheaths, which is typically performed via manual tracing. Done manually, this process can be immensely time-consuming and laborious. To facilitate *g*-ratio quantification, we created MyelTracer by wrapping the powerful Python libraries provided by OpenCV in an easy-to-use GUI using PyQt5. MyelTracer performs automatic detection of contours using dynamic thresholding and separation of adjacent myelin sheaths based on user input. We packaged MyelTracer as a readily installable software for Windows and Mac OS X operating systems. Conceptually, MyelTracer takes a raw electron micrograph input image (Figure 12A), converts it to grayscale, applies a bilateral filter, and thresholds it to a black and white binary image (Figure 12B). MyelTracer extracts boundaries between the black and white pixels on the binary image and creates a contour image based on user-defined filtering parameters (Figure 12C). For *g*-ratio plotting, MyelTracer is configured to measure the inner and outer myelin sheath as well as the axon diameter to account for periaxonal space present in electron micrographs (Figure 12A). Using the GUI (Figure 12G), the user can select the contours of axon, inner myelin, and outer myelin while adjusting the threshold to closely match the displayed contours to the underlying myelin ultrastructure. Once selected, MyelTracer groups the corresponding axons, inner myelin, and outer myelin together and overlays those selections on top of the original image (Figure 12D). The software automatically computes diameters of perfect circles from area measurements and derives *g*-ratios by dividing inner myelin diameters by outer myelin diameters, which can then be plotted against the axon diameter (Figure 12E, F).

To use MyelTracer efficiently, we recommend the following workflow (Figure 12H). First, select all axons in the image by adjusting the threshold parameter to match contours to the axon shape. Second, adjust the threshold to match myelin sheaths. Third, check for contiguous contours of adjacent myelin sheaths as well as discontinuous contours around myelin sheaths. If necessary, use the cut tool to separate adjacent myelin sheaths, or use the draw tool to connect discontinuous myelin sheaths. Fourth, select the inner and outer myelin sheath contours, adjusting the threshold parameter to fit. Fifth, save the progress and export the result, which includes *g*-ratio measurements and an overlay (Figure 12D). MyelTracer also provides a manual tracing option for otherwise untraceable features and a counting tool to calculate the percentage of myelinated axons. Together, these functions make MyelTracer an all-in-one software suite for studying myelin ultrastructure.

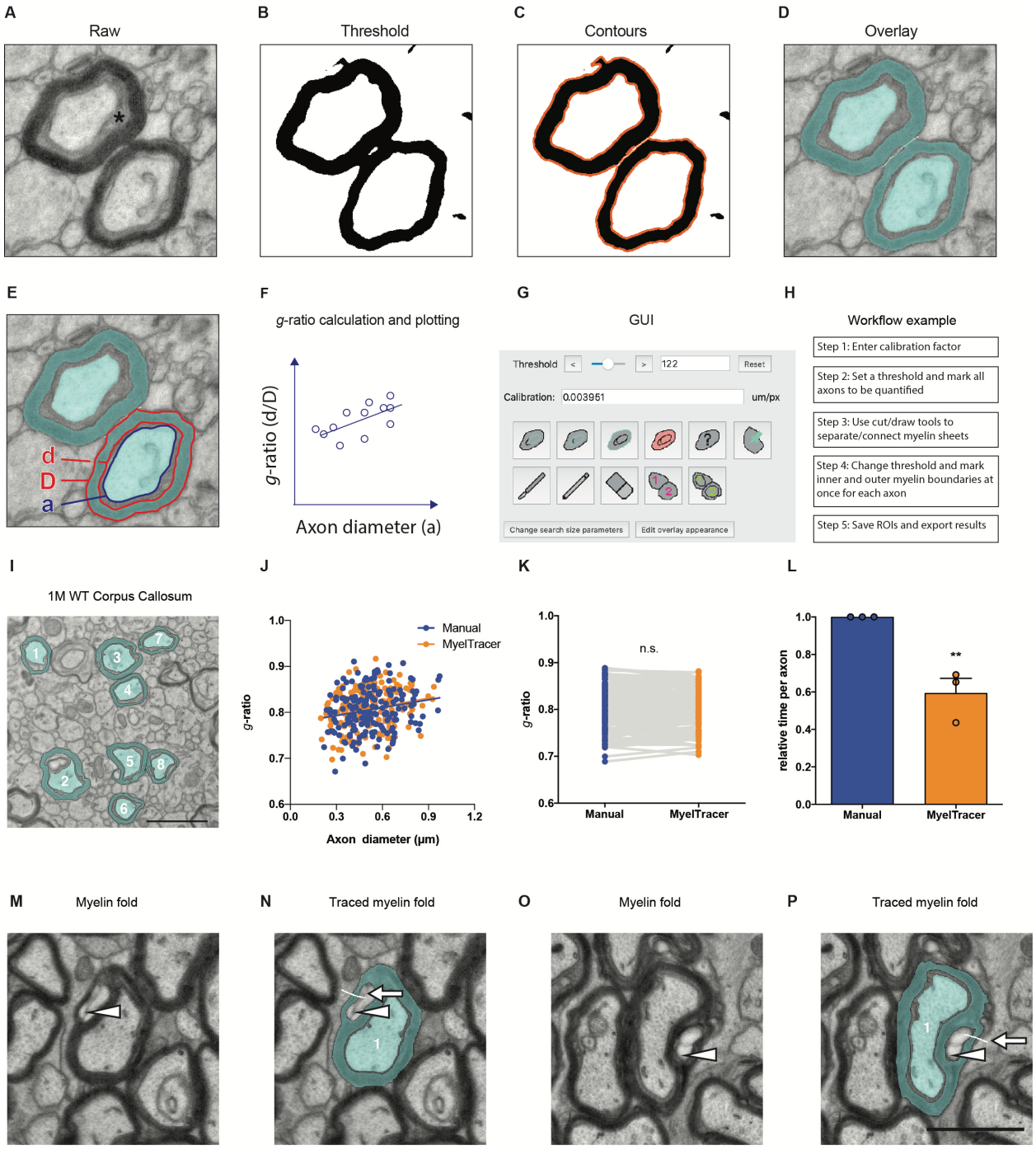

Figure 12 MyelTracer semi-automatically traces axons and myelin and returns results consistent with manual tracing. ***A-D***, Electron micrograph of dorsal corpus callosum, software-generated threshold overlays, and post-selection overlay (blue) show different steps of the image analysis. * periaxonal space. ***E,*** Electron micrograph with MyelTracer overlay and outlines for features including axon diameter (a), inner myelin diameter (d), and outer myelin diameter (D), each computed from the respective areas. ***F,*** Schematic for *g*-ratio scatterplot illustrating how MyelTracer calculates the *g*-ratio. ***G,*** Image of the main user interface of MyelTracer. ***H***, Schematic showing an example workflow using MyelTracer. ***I***, Representative electron micrograph of corpus callosum from one-month-old

wild-type mice. ***J****, g*-ratio scatter plot from manual and MyelTracer quantifications for the same axons. ANCOVA test p-value=0.8996 (slopes) and p=0.7044 (intercepts) , n=174 axons. ***K***, *g*-ratios from manual and MyelTracer quantification paired for the same axons. Student's t-test p-value=0.9045, n=174 axons. ***L***, Comparison of time consumption between manual quantification and quantification using MyelTracer. Individual data points represent the average time spent per axon per image. p-value=0.0069; Student's t-test. Scale bar, 1 µm. ***M-P***, Illustration of MyelTracer's ability to quantify myelin sheets with folds (arrowheads). Folds require the user to draw a white line (arrows) with the cut tool to connect the area inside the fold with the outside area for semi-automated detection. Scale bar, 1 µm.

3.3.2 MyelTracer saves quantification time while maintaining accuracy

Myelin *g*-ratio quantification is routinely done by manually tracing the myelin sheath. Manual tracing is very time-consuming but considered the standard practice for accurate results. To compare the accuracy of MyelTracer to manual tracing in moderately myelinated tissues, we measured *g*-ratios using both methods in the same electron micrographs of corpus callosum from one-month-old mice (Figure 12I). Plotting the *g*-ratio as a function of axonal diameter, we did not find a significant difference between MyelTracer and manual quantification results (Figure 12J, MyelTracer: slope 0.061, y-intercept 0.77, n = 173, Manual: slope 0.057, y-intercept 0.77, n = 173; slopes p = 0.8996, intercept p = 0.7044) and their averages (Figure 12K, MyelTracer mean ± SD: 0.8072 ± 0.04417, n = 173, Manual: 0.8066 ± 0.04220, p = 0.9045). Next, to examine the amount of quantification time MyelTracer saves, the average amount of quantification time spent per axon was compared between these two methods. Using MyelTracer, significantly less time was spent per axon compared to manual tracing (Figure 12L, MyelTracer mean: 0.593, Manual: mean 1.0, n = 173 axons, 3 images, p = 0.0069). Further, to exemplify that MyelTracer can trace myelin sheets containing folds, several such sheets were analyzed. Taking advantage of the cut tool, MyelTracer readily detects myelin folds and correctly quantifies the myelin sheet without including the area in

the fold (Figure 12M-P). Together, these data show that MyelTracer maintains a high level of accuracy, comparable to manual tracing, while saving about 40% of time for the user.

Myelination is spatiotemporally regulated (Mayoral and Chan, 2016; Sun et al., 2018). As a result, there are variations in myelin sheath thickness and spatial density of myelinated axons across different types of tissues and developmental time points. To assess the feasibility of using MyelTracer for different types of tissue samples, electron micrographs from optic nerves and sciatic nerves were examined (Figure 13A, E). In the optic nerve of two-month-old mice, plotting *g*-ratio as a function of axon diameter revealed no significant difference between the results from using MyelTracer and those from manual quantification (Figure 13B, MyelTracer: slope 0.1046, y-intercept 0.7372, n = 193, Manual: slope 0.1001, y-intercept 0.7427, n = 193, slopes $p = 0.8311$, intercept $p = 0.4695$). We did not find a significant difference in *g*-ratio (Figure 13C, MyelTracer mean ± SD: 0.7976 ± 0.04328, n = 193, Manual: 0.8018 ± 0.04244, $p = 0.3406$), but a significant reduction in time spent quantifying *g*-ratio (Figure 13D, MyelTracer mean: 0.4808, Manual: mean 1.0, n = 193 axons, 3 images, $p = 0.0046$). In the sciatic nerve of one-month-old mice, regression relationships between *g*-ratio and axon diameter were not significantly different between using MyelTracer and manual quantification (Figure 13F, MyelTracer: slope -0.0386, y-intercept 0.627, n = 104, Manual: slope -0.030, y-intercept 0.615, n = 104, slopes $p = 0.7437$, intercept $p = 0.8997$). Comparing the results from using MyelTracer and those from manual quantification in the sciatic nerve, there was no difference in *g*-ratio (Figure 13G, MyelTracer mean ± SD: 0.5586 ± 0.07121, n = 104, Manual: 0.5576 ± 0.06833, $p = 0.9146$), while there was a significant reduction in time spent quantifying *g*-ratio (Figure 13H, MyelTracer mean 0.4054, Manual mean 1, n = 104 axons, 6 images, $p < 0.0001$). Together, these findings demonstrate that MyelTracer saves 40-60% user quantification time and offers accuracy levels that are comparable to manual quantification.

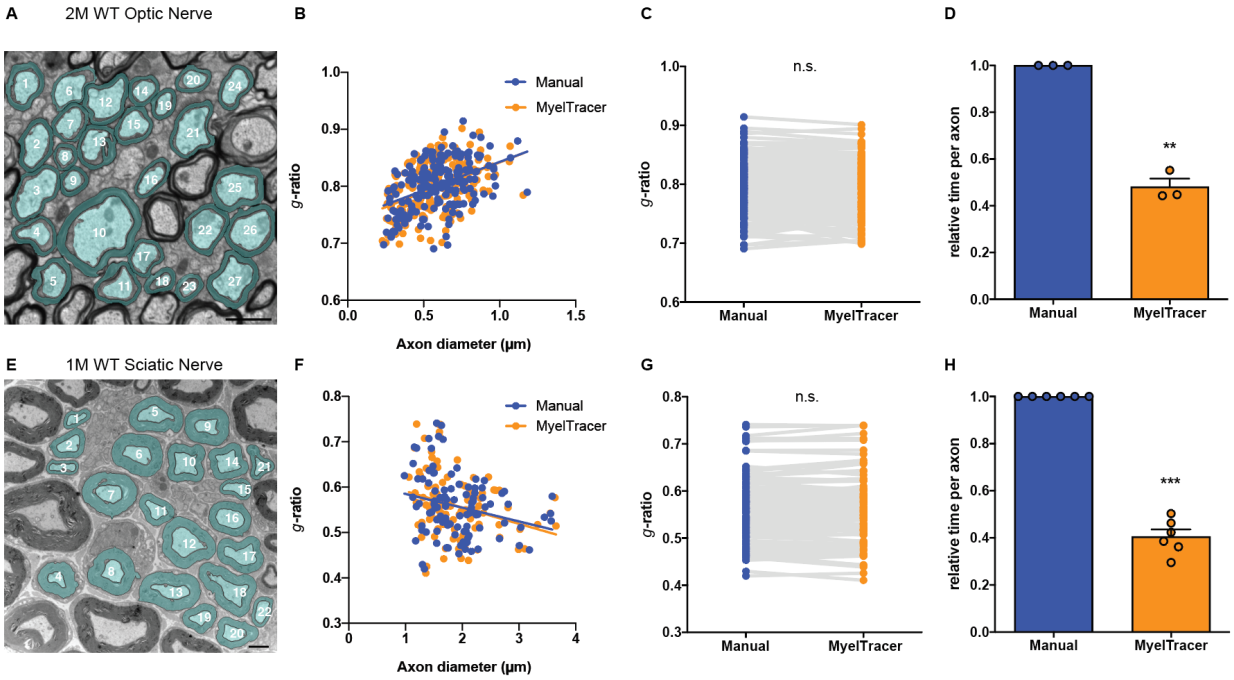

Figure 13 MyelTracer accurately returns *g*-ratios for myelinated tissues of varying axonal density. ***A***, Representative electron micrograph of the optic nerve at two months of age (2M) with MyelTracer-generated overlays (blue). Scale bar, 1 µm. ***B,*** *g*-ratio scatter plot from manual and MyelTracer quantifications for the same axons. ANCOVA test p-value=0.8311 (slopes) and p=0.4695 (intercepts), n=193 axons. ***C***, *g*-ratios from manual and MyelTracer quantifications paired for the same axons. p=0.3406, n=193 axons. ***D***, Comparison of time consumption between manual quantification and quantification using MyelTracer. Individual data points represent the average time spent per axon per image. p-value=0.0046. **E**, Representative electron micrograph of the sciatic nerve at one month of age with MyelTracer-generated overlays (blue). Scale bar, 2 µm. ***F,*** *g*-ratio scatter plot from manual and MyelTracer quantifications for the same axons. ANCOVA test p-value=0.7437 (slopes) and p=0.8997 (intercepts), n=104 axons. ***G***, *g*-ratios from manual and MyelTracer quantifications paired for the same axons. P=0.9146, n=104 axons. ***H***, Comparison of time consumption between manual quantification and quantification using MyelTracer. Individual data points represent the average time spent per axon per image. p-value<0.0001; Student's t-test.

3.3.3 Myelin thickness abnormalities can be detected using MyelTracer

Using MyelTracer for *g*-ratio quantification saves a significant amount of time and produces accurate results across different types of tissues from wild-type mice (Figures 12, 13). In research settings, however, most investigators seek a tool to detect differences between genotypes or treatment paradigms. To test whether MyelTracer is suitable for detecting differences between

two experimental groups, its performance was tested using electron micrographs from control ($Gtf2i^{fl/fl}$, $Nex\text{-}Cre^{-/-}$) and $Gtf2i^{fl/fl}$; $Nex\text{-}Cre^{+/-}$ mice, a model for Williams Syndrome with a known hypomyelination phenotype (Barak et al., 2019). With their genotypes blinded, electron micrographs of corpus callosum from both groups at one-month of age were analyzed using MyelTracer (Figure 14A, B). Regression relationships between *g*-ratio and axon diameter were significantly different between control and $Gtf2i^{fl/fl}$; $Nex\text{-}Cre^{+/-}$mice (Figure 14C, Control: slope 0.1649, y-intercept 0.6447, n = 332 axons, n = 3 mice, $Gtf2i^{fl/fl}$; $Nex\text{-}Cre^{+/-}$: slope 0.1487, y-intercept 0.7132, n = 787, n = 3 mice, slopes $p = 0.1484$, intercept $p < 0.001$). The *g*-ratio measurements were higher in $Gtf2i^{fl/fl}$; $Nex\text{-}Cre^{+/-}$ mice than those in control mice, indicating a reduction in myelin sheath thickness, a result consistent with the original report (Barak et al., 2019). Together, these data demonstrate that MyelTracer is suitable for detecting differences in myelin *g*-ratios across different genotypes.

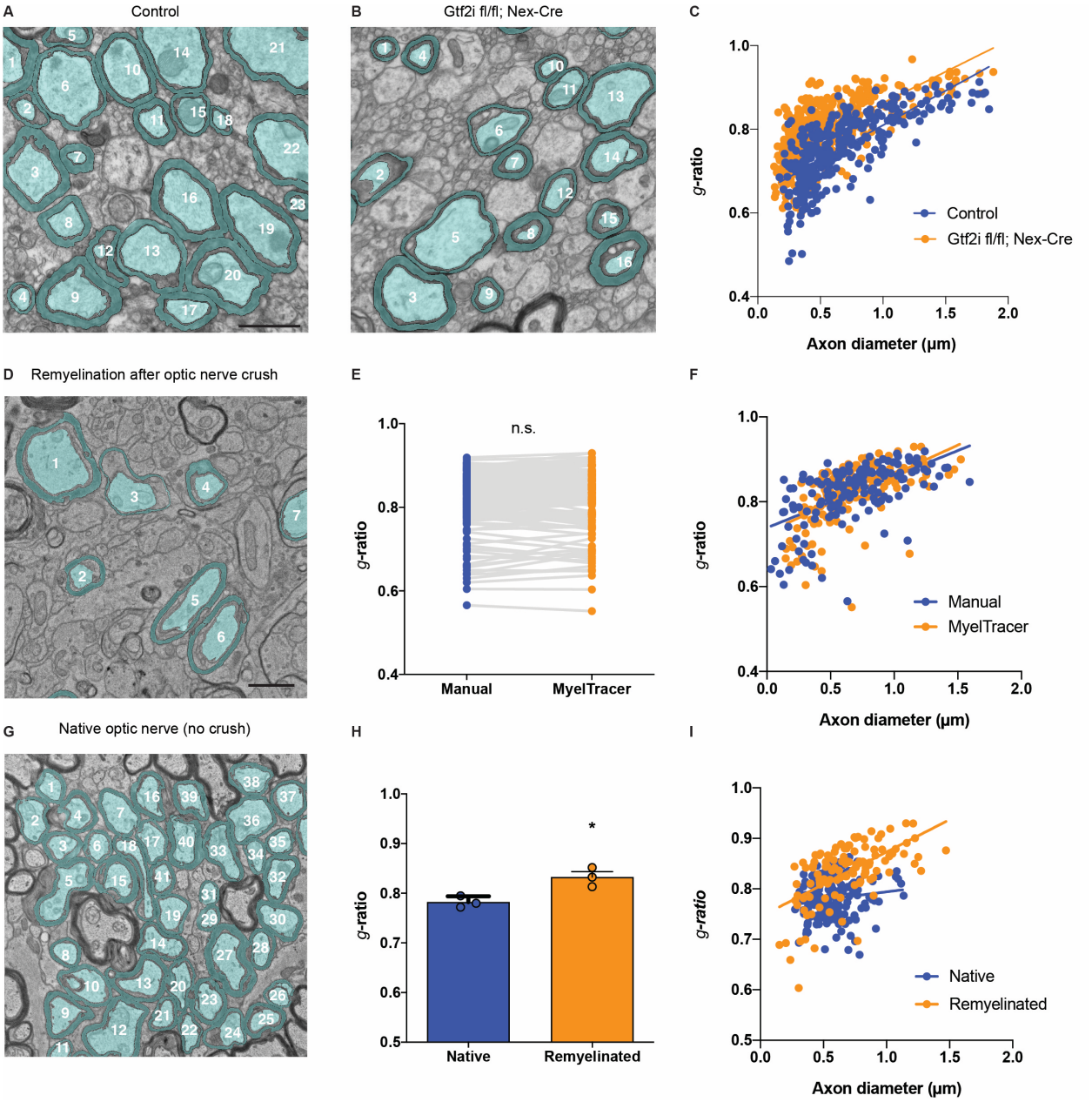

Figure 14 MyelTracer can be used to detect a myelin thickness abnormality in a Williams Syndrome mouse model and to measure *g*-ratios in remyelination.

A-B, Representative electron micrographs of the corpus callosum in control and Gtf2i fl/fl; Nex-Cre mice at one month of age with MyelTracer-generated overlays (blue). Scale bar, 1 µm. ***C***, *g*-ratio scatter plot from using MyelTracer for control and Gtf2i fl/fl; Nex-Cre mice. p-value<0.0001; ANCOVA test; n=3 mice, 332 axons for control and n=3 mice, 455 axons for Gtf2i fl/fl; Nex-Cre mice. ***D***, Representative electron micrograph of the optic nerve 28 days after optic nerve crush with MyelTracer-generated overlays (blue). Scale bar, 1 µm. ***E***, *g*-ratios from manual and MyelTracer quantifications paired for the same axons. P=0.9699, n=155 axons. ***F,*** *g*-ratio scatter plot from manual and MyelTracer quantifications for the same axons. ANCOVA test p-value=0.1511 (slopes) and p=0.8686 (intercepts), n=155 axons. ***G***, Representative electron micrograph of the native control optic nerve with MyelTracer-generated overlays (blue).

H, *g*-ratio group comparison of axons from native control and remyelinated axons from mice following optic nerve crush. p-value<0.0183; t-test; n=3 mice per group. ***I,*** *g*-ratio scatter plot of axons from native control and remyelinated axons from mice following optic nerve crush. ANCOVA test p-value < 0.0001 (slopes), Native control n=183 axons, Remyelinated n=116 axons.

3.3.4 MyelTracer can be used to quantify *g*-ratios in remyelination

MyelTracer readily recognizes well-developed myelin sheaths in micrographs of both central and peripheral nerves and axon tracts. In contrast to the relatively thick and compact myelin in these tissues, myelin in remyelinating tissues after injury is characterized by a thinner morphology (Franklin and ffrench-Constant, 2008; Duncan et al., 2017). To test MyelTracer's ability to quantify *g*-ratios in tissues undergoing remyelination, we analyzed micrographs from an optic nerve crush model 28 days after the injury (Figure 14D). Comparing the results from MyelTracer and those from manual quantification in this model, there was no difference in *g*-ratio (Figure 14E, MyelTracer mean ± SD: 0.8212 ± 0.06843, n = 155, Manual: 0.8210 ± 0.06944, p = 0.9699). Further, regression relationships between *g*-ratio and axon diameter were not significantly different between MyelTracer and manual quantification (Figure 14F, MyelTracer: slope 0.1484, y-intercept 0.7150, n = 155, Manual: slope 0.1282, y-intercept 0.7273, n = 155, slopes p = 0.1511, intercept p = 0.8686). To further test whether MyelTracer is suitable to detect the thinned myelin sheets in remyelination compared to native myelin sheets, its performance was tested using region-matched electron micrographs from remyelinated axons and axons from matched native control animals (Figure 14G). Comparison of the average *g*-ratio per animal revealed significantly increased *g*-ratios in the remyelinated group compared to the native control group (Figure 14H, Native control mean ± SD: 0.7821 ± 0.01162, n = 3 mice, Remyelinated: 0.8324 ± 0.01942, n = 3 mice, p = 0.0183). Regression relationships between *g*-ratio and axon diameter were significantly different between the optic nerve axons in native control and remyelinated mice (Figure 14I,

Native control: slope 0.03137, y-intercept 0.7627, n = 183 axons, Remyelinated: slope 0.1281, y-intercept 0.7449, n = 116, n = 3 mice, slopes $p < 0.0001$). Together, these results indicate that MyelTracer is suitable for *g*-ratio measurements in remyelination.

3.4 Discussion

In this study, we show that MyelTracer can address the need for an easy-to-use, stand-alone software for streamlining *g*-ratio quantification. OpenCV, PyQt5 and fbs were used in Python to develop and package MyelTracer, an easy to install software with an intuitive GUI. MyelTracer utilizes contrast in electron micrographs to generate contours around axons and myelin sheaths. The user can select contours outlining myelin features of interest (axons, inner myelin, and outer myelin), which then allow MyelTracer to group corresponding features, measure their areas and calculate *g*-ratios. As an all-in-one platform for myelin analyses, MyelTracer can also be used to calculate the percentage of myelinated axons. Using MyelTracer, user quantification time is reduced by 40-60% depending on the region, and its accuracy is comparable to manual tracing. Using MyelTracer, a known hypomyelination phenotype of the Williams Syndrome mouse model can be detected, confirming its suitability for studies assessing phenotypic changes in myelin sheaths. MyelTracer is freely available at https://github.com/HarrisonAllen/MyelTracer.

Myelin ultrastructure is highly heterogeneous with a wide range of axon calibers and myelin sheath morphologies, presenting a challenge for automated analysis. MyelTracer uses OpenCV to automatically contour cross-sections of axons and myelin sheaths in electron micrographs (Figure 12A-C). The easy-to-use GUI allows users to intuitively interact with and fine-tune the results generated by the underlying computer vision algorithms (Figure 12D, G). MyelTracer decreases analysis time by dramatically accelerating axon and myelin sheath contouring compared to manual tracing. This automated feature differentiates MyelTracer from existing non-automated tools, such as *GRatio for ImageJ*, which is an ImageJ plugin that facilitates grouping of traced structures and data export (Goebbels et al., 2010).

In addition to MyelTracer, several semi-automated and automated tools are available that exhibit different strengths and weaknesses. *AxonSeg* and *AxonDeepSeg* are MATLAB-based segmentation algorithms that are fully automated, enabling high-throughput measurements (Zaimi et al., 2016, 2018). These tools are useful for processing large datasets but require image pre-processing, adjustment of parameters in MATLAB, or additional training of the neural network using manually labeled images from user-specific datasets, which can be hurdles for implementation. Janjic et al. developed a high-fidelity tool using deep neural networks, which suits researchers with a computer science background seeking an advanced *g*-ratio quantification tool (Janjic et al., 2019). While there are other useful tools available, MyelTracer's intuitive GUI makes it a powerful tool allowing researchers to quantify myelin without computer science knowledge.

G-ratio quantification using MyelTracer was demonstrated to be accurate across different tissues, such as corpus callosum, optic nerve, and sciatic nerve (Figures 12, 13). For these types of samples, there was a 40-60% reduction in time spent on quantification (Figure 12L, 2D, 2H). The variation in the amount of time-reduction depended on the type of tissue. The smallest time-reduction was for corpus callosum of one-month-old mice. This is likely due to the heterogeneity in axonal caliber, axonal density, and the contrast level among the axon, periaxonal space, inner tongue, and the myelin sheath (Figure 12A, I). In contrast, the greatest time-reduction was observed for sciatic nerve, which has clearly defined myelinated axons with homogeneous morphology, minimal periaxonal space and minimal myelin contiguity between adjacent axons (Figure 13E, H). Comparing MyelTracer workflows for corpus callosum versus sciatic nerve, a major difference was that the latter required less manual input to separate contiguous myelin sheaths (Step 3, Figure 12H). Similar to manual tracing and other computational toolboxes, MyelTracer also relies on the

quality of input images and therefore shows less effective performance for images with poor contrast levels, artifacts from inadequate perfusion or tissue handling.

The analysis of electron micrographs from Williams Syndrome mice shows that MyelTracer readily detects abnormalities in myelination (Figure 14A-C), demonstrating the suitability of MyelTracer for detecting differences in myelin *g*-ratio across different genotypes or treatment groups. In such studies, MyelTracer will decrease user quantification time, and streamline data generation for publication purposes.

Extending the application for MyelTracer, analysis of remyelinating axons 28 days after optic nerve crush shows that the software is suitable for *g*-ratio measurements in studies of remyelination (Figure 14D-I). Myelin sheaths in remyelinating tissues are generally found to be thinner (Franklin and ffrench-Constant, 2008; Duncan et al., 2017), and they can appear almost discontinuous in a given sectioning plane. This presents a challenge to automation and may require user input using MyelTracer's *Cut* and *Draw* tools as extensively outlined in the Users' Manual (Extended Data 2). Notwithstanding these challenges, MyelTracer is suitable for the semi-automated tracing of micrographs in studies of remyelination provided that the myelin sheaths and axons display good contrast.

As a user-friendly all-in-one software suite, MyelTracer will also allow researchers to quantify the percentage of myelinated axons, which together with *g*-ratio, are the most commonly reported metrics in myelin studies. Beyond existing tools and MyelTracer, advances in computer vision and artificial intelligence may further advance data analysis methods and produce more powerful toolboxes to streamline quantitative analysis of myelin ultrastructure.

4 Probing the Role of IgG and Microglial FCER1G in White-matter Development

I generated and characterized the *Fcer1g Fx* mouse. I performed the western blots and immunostainings, flow cytometry, fluorescence-activated cell sorting, qPCR, drug administration for microglia depletion, sample preparation and imaging for electron microscopy, and *in-situ* hybridizations. Minqing Jiang contributed to the electron microscopy, immunofluorescence imaging, and immunoblots. Liang Li contributed to the in-situ hybridization experiment. Nicholas Sanders helped with mouse colony maintenance. The RNA sequencing work was carried out by the Barbara K. Ostrom (1978) Bioinformatics and Computing Core Facility of the Swanson Biotechnology Center.

4.1 Abstract

In the CNS, oligodendrocytes produce myelin to promote axonal health and conductivity. Under physiological conditions, changes in myelin are linked to learning and behavioral plasticity, whereas aberrant changes in myelin underlie motor, sensory, and cognitive impairments in disease. While we increasingly understand the cellular mediators and molecular cues that guide myelin development, several pathways remain incompletely defined. Previous research implicated FCER1G, a mandatory subunit of Fc receptors in myelination. Here, I address its cellular pathway and test whether its canonical ligand, IgG, plays a role in myelin development. Using immunoblotting and immunostaining, I find that maternal IgG localizes to microglia in the developing brain. Further, immunoblotting, immunofluorescence staining, and electron microscopy reveal fewer MAG^+ oligodendrocytes and thinner axons in mice lacking IgG postnatally. While gene expression analysis and *in-situ* hybridization show *Fcer1g* expression exclusively on microglia, conditional deletion of this gene in microglia does not replicate the defects seen in mice lacking IgG. Similarly, mice constitutively lacking *Fcer1g* do not display the same phenotype in axon thinning, suggesting that IgG exerts its effect through a non-canonical mechanism. Studies using broad microglia depletion during development reveal no clear effects on MAG^+ oligodendrocytes and other myelin metrics and argue against a binary effect of microglia on myelin development. Instead, transcriptomic studies on sorted microglia indicate that IgG is required for the induction of a specific subset of microglia that is known to support myelination in the developing white matter. Together, these studies provide a characterization of IgG in the developing brain and suggest further avenues to test the role of specific microglia subsets.

4.2 Introduction

Myelination of axons evolved in vertebrates to enhance propagation of signals and create more efficient nervous systems (Nave, 2010). Defects in myelin are hallmarks of many clinical diseases like multiple sclerosis, Pelizaeus Merzbacher disease, and Charcot-Marie-Tooth disease that manifest as impairments in sensory and motor function (Krajewski et al., 2000; Sander et al., 2000; Franklin and ffrench-Constant, 2008; Lin and Popko, 2009; Duncan and Radcliff, 2016). In addition to these prototypic white-matter diseases, myelin abnormalities have more recently been discovered in mouse models of neurodevelopmental disorders, including Pitt Hopkins Syndrome, Rett Syndrome, autism spectrum disorders (ASDs), and William's Syndrome (Zhao et al., 2018; Barak et al., 2019; Phan et al., 2020).

In the CNS, oligodendrocytes form myelin, and this process is supported by neurons and other glia that display and secrete important molecular cues (Liedtke et al., 1996; Hagemeyer et al., 2017; Wlodarczyk et al., 2017; Giera et al., 2018; Barak et al., 2019). Recently, the contribution of these cells and molecular cues have become an intense focus in research. Microglia secrete IGF-1 during postnatal development and thus promote the development of thicker myelin sheaths (Wlodarczyk et al., 2017). Similarly, microglia-derived transglutaminase-2 and activin-A increase OPC proliferation and differentiation (Miron et al., 2013; Giera et al., 2018). Amongst the molecular pathways and genes studied, a previous report shows that the Fc receptor subunit *Fcer1g* is required for myelination (Nakahara et al., 2003). Canonically, Fc receptors bind IgG appears to penetrate the brain (Fairén et al., 1992; Upender et al., 1997; Hazama et al., 2005). However, neither the function of IgG, nor another Fc receptor ligand has been tested in white-matter development.

Here, I address the molecular and cellular pathways underlying the role of *Fcer1g* in myelination. First, I provide evidence for the localization of the Fc receptor ligand IgG to microglia in the developing corpus callosum. Using two independent mouse models for the depletion of IgG, I show that IgG is not produced by the pups but derived from the dam. I further demonstrate that mice lacking IgG harbor fewer MAG^+ oligodendrocytes and thinner axons in the corpus callosum. Aiming to determine the cellular pathway of IgG-FcR signaling, I show that a mandatory Fc receptor subunit is only expressed by microglia and not OPCs in the developing mouse parenchyma. Studies using conditional deletion of this gene in microglia show that the effects of IgG on corpus callosum development are not mediated through microglial Fc receptors. Using a constitutive Fc receptor deletion strategy, I further provide evidence suggesting that IgG exerts its effects through a non-canonical Fc receptors-independent pathway. Finally, I adopt two strategies aiming to address the involvement of microglia in these processes. First, I show that broadly depleting all subsets of microglia does not clearly produce a hypomyelination phenotype. Second, I provide evidence suggesting that IgG influences the polarization of microglia and is required for the induction of a microglia subset that resides in the white matter.

4.3 Results

4.3.1 Maternally-derived Immunoglobulin Binds to Microglia in the Developing Brain

Brain development is carefully orchestrated by neurons and glia that utilize both cell-autonomous and secreted factors, which have become an intense focus in research. Amongst the pathways and factors, previous studies show that *Fcer1g*, encoding an obligatory subunit for Fc-receptors, is required for myelination (Nakahara et al., 2003). Further, early studies suggest that the canonical ligand of Fc-receptors, IgG, may occur in the brain (Fairén et al., 1992; Upender et al., 1997; Hazama et al., 2005). To test whether IgG indeed occurs in the brain, to determine the spatiotemporal expression of IgG in the brain in depth, and to define its source during the time when myelination occurs, biochemical and immunohistochemical approaches were used. First, I examined protein preparations from brains from postnatal day 0 (P0) to postnatal day 28 (P28, Figure 15A). A band of 100 to 150 kDa, corresponding to the molecular weight of IgG was observed, and the amount declined along development. To confirm the molecular identity as well as the source of this immunoreactivity, I further prepared protein samples from P14 WT and P14 $RAG^{-/-}$ mice, which are immunodeficient, adult WT mice, and mice from an immunodeficient $RAG^{-/-}$ dam (Figure 15B). Immunodeficient P14 mice still displayed immunoreactivity at 150 kDa, whereas adult mice and P14 mice from $RAG^{-/-}$ dams did not. These data suggested that the band corresponded to IgG, which is not endogenously produced by the pup, but derived from the dam. The data further show that its amount declines along development to undetected levels in the adult. If IgG perfuses the brain parenchyma rather than just the cerebral microvasculature, it should also be detectable in the cerebrospinal fluid (CSF). To test this possibility, I collected CSF from P1 mice and compared it to serum and purified IgG (Figure 15C). Immunoreactivity corresponding to IgG was detectable in the CSF and this reactivity was much lower compared to

immunoreactivity of serum. This suggests that IgG is present in the CSF, yet reduced in concentration compared to the serum.

In the peripheral system, IgG occurs in a soluble form as well as membrane bound upon interaction with its receptor FcR. To determine the localization of IgG in the brain, I stained brain slices from 7-day-old mice from WT or immunodeficient dams ($RAG^{-/-}$) with antibodies against IgG and microglia, the brain cells that express FcR (Zhang et al., 2014; Saunders et al., 2018). IgG immunoreactivity was diffusely present throughout the parenchyma and especially concentrated on IBA1-positive microglia in the corpus callosum (Figure 15D-I). IgG-immunofluorescence was completely absent in P7 pups from $RAG^{-/-}$ dams, indicating specificity of the signal (Figure 15G-I).

Immunoglobulins can be passed from the dam to the offspring via the placenta or the colostrum, and persist for several days to weeks due to its half-life of approximately 21 days. To test whether IgG occurrence in the brain reflects IgG persistence in the brain after initial prenatal acquisition or, alternatively, acquisition through the milk postnatally, I removed pups from their dams at P1 and subjected them to cross fostering until analysis at P7. Mice born to immunodeficient dams that were fostered by WT dams readily acquired IgG (Figure 15J-L) and mice fostered by immunodeficient dams after being born to WT dams displayed little IgG (Figure 15M-O). To further test the source of IgG, a second genetic model was used. Mice lacking the neonatal Fc-receptor FcRn (encoded by the gene *Fcgrt*) are unable to transport IgG across their gut epithelium and thus lack maternal IgG in their plasma (Roopenian and Akilesh, 2007). Using both immunoblotting and immunofluorescence staining, I observed that Fcgrt-deficient mice lack the immunostaining signal seen in wildtype animals (Figure 15 P-R). Together, these data support

the conclusion that the immunostaining signal represents IgG, which is taken up postnatally from the milk into the brain, where its concentration declines rapidly in absence of replenishment.

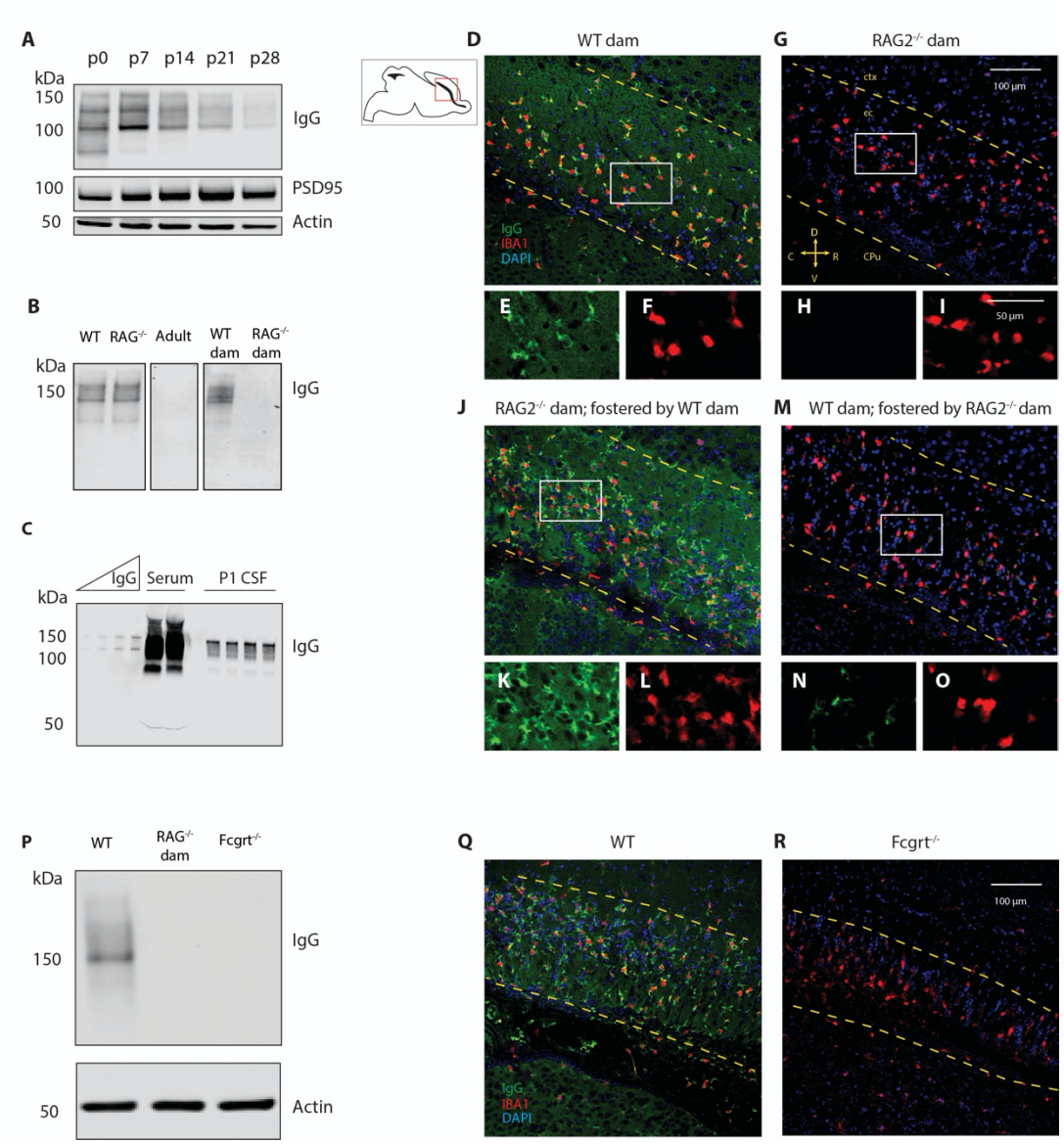

Figure 15 Maternal Immunoglobulin G from the milk binds to microglia in the postnatal brain.

A Brains at different ages were lysed and immunoblotted with anti-mouse secondary antibodies. PSD95 and actin serve as loading controls. **B** Brain lysates of P14 WT and RAG-/- (immunodeficient), adult, and P14 mice from WT or RAG-/- dams (immunodeficient dam) were immunoblotted. **C** Purified mouse IgG, serum, and postnatal day 1 (P1) CSF were immunoblotted. **D-F** High-power confocal micrograph of the corpus callosum of perfused P7 WT brains, sagitally sectioned and stained against mouse IgG and IBA1. **G-H** Brain of P7 mouse born to RAG-/- dam processed as in D-F. **J-L** Brain of P7 mouse born to RAG-/- dam and fostered from P1 to P7 by WT dam. M-O Brain of P7 mouse born to WT dam and fostered from P1 to P7 by RAG-/- dam. **P** Representative immunoblot from P7 mice born

to WT dam, RAG-/- dam, or of Fcgrt-/- genotype. **Q-R** Representative confocal micrographs of the corpus callosum of perfused WT and Fcgrt-/- brains, sagitally sectioned and stained against mouse IgG and IBA1.

4.3.2 Mice deprived of Maternal Immunoglobulin Develop with fewer MAG$^+$ Oligodendrocytes and Lower Myelin Protein Expression in Early Postnatal Life

Microglia influence oligodendrocyte precursor cell development through phagocytosis and secretion of molecular cues (Wlodarczyk et al., 2017; Giera et al., 2018; Li et al., 2019). Nakahara and colleagues examined *Fcer1g*, the mandatory subunit of activating Fc-receptors and found that it was necessary for the development of myelin (Nakahara et al., 2003). To test whether the canonical ligand of these Fc-receptors is similarly required for myelination, I immunostained brain slices from postnatal day 10 pups born to wildtype or RAG2$^{-/-}$ dams for MAG$^+$ oligodendrocytes, which were most severely affected in the Nakahara study (Figure 16A, B). Comparing the number of immunostaining-positive cells between the genotypes, I found that mice born to immunodeficient dams harbored significantly fewer MAG$^+$ cells (Figure 16C, WT dam mean ± SEM: 114.8 ± 3.981, n = 11 pups from 3 dams, RAG2$^{-/-}$ dam: 93.91 ± 13.31, n=11 from 2 dams, p = 0.0014). To further examine the number of OLIG2$^+$ oligodendrocytes and oligodendrocyte precursor cells, additional immunostainings were performed (Figure 16D, E). Comparison of pups born to WT and pups born to RAG2$^{-/-}$ dams revealed significantly reduced numbers of OLIG2+ cells in pups born to RAG2$^{-/-}$ dams (Figure 16F, WT dam mean ± SEM: 697.4 ± 12.58, n = 13 pups from 4 dams, RAG2$^{-/-}$ dam: 627.8 ± 17.49, n=13 from 3 dams, p = 0.0036). These reductions were significant, albeit less severe than the impairments seen in *Fcer1g* knockout animals. Previous studies of mice lacking *Fcer1g* further reported reduced myelin protein expression in protein lysates (Nakahara et al., 2003). To test whether mice lacking postnatal IgG express lower levels of myelin proteins in early postnatal development, I turned to the spinal cord as a tissue that

is relatively highly myelinated at this age compared to the brain and more reproducibly dissectable. Spinal cords were dissected from pups born to wildtype or RAG2$^{-/-}$ dams, tissue lysates prepared, and immunoblotted (Figure 16G). Comparing the immunoreactivity between pups born to wildtype dams or immunodeficient dams, several reductions in protein expression were observed. Significant reductions were observed for MAG (Figure 16H, WT dam mean ± SEM: 1.0 ± 0.04, n = 9 pups from 3 dams, RAG2$^{-/-}$ dam: 0.8296 ± 0.04, n=11 from 3 dams, p = 0.0071), MBP 21 kDa isoform (Figure 16I, WT dam mean ± SEM: 1.0 ± 0.07, n = 9 pups from 3 dams, RAG2$^{-/-}$ dam: 0.6929 ± 0.05, n=11 from 3 dams, p = 0.002), MBP 18.5 and 17 kDa isoforms (Figure 16J, WT dam mean ± SEM: 1.0 ± 0.05, n = 9 pups from 3 dams, RAG2$^{-/-}$ dam: 0.7155 ± 0.03, n=11 from 3 dams, p = 0.002), and a trend was observed for PLP (Figure 16K, WT dam mean ± SEM: 1.0 ± 0.06, n = 9 pups from 3 dams, RAG2$^{-/-}$ dam: 0.8299 ± 0.07, n=11 from 3 dams, p = 0.07). Together, these data indicate that mice lacking IgG postnatally develop myelin abnormally during early postnatal development.

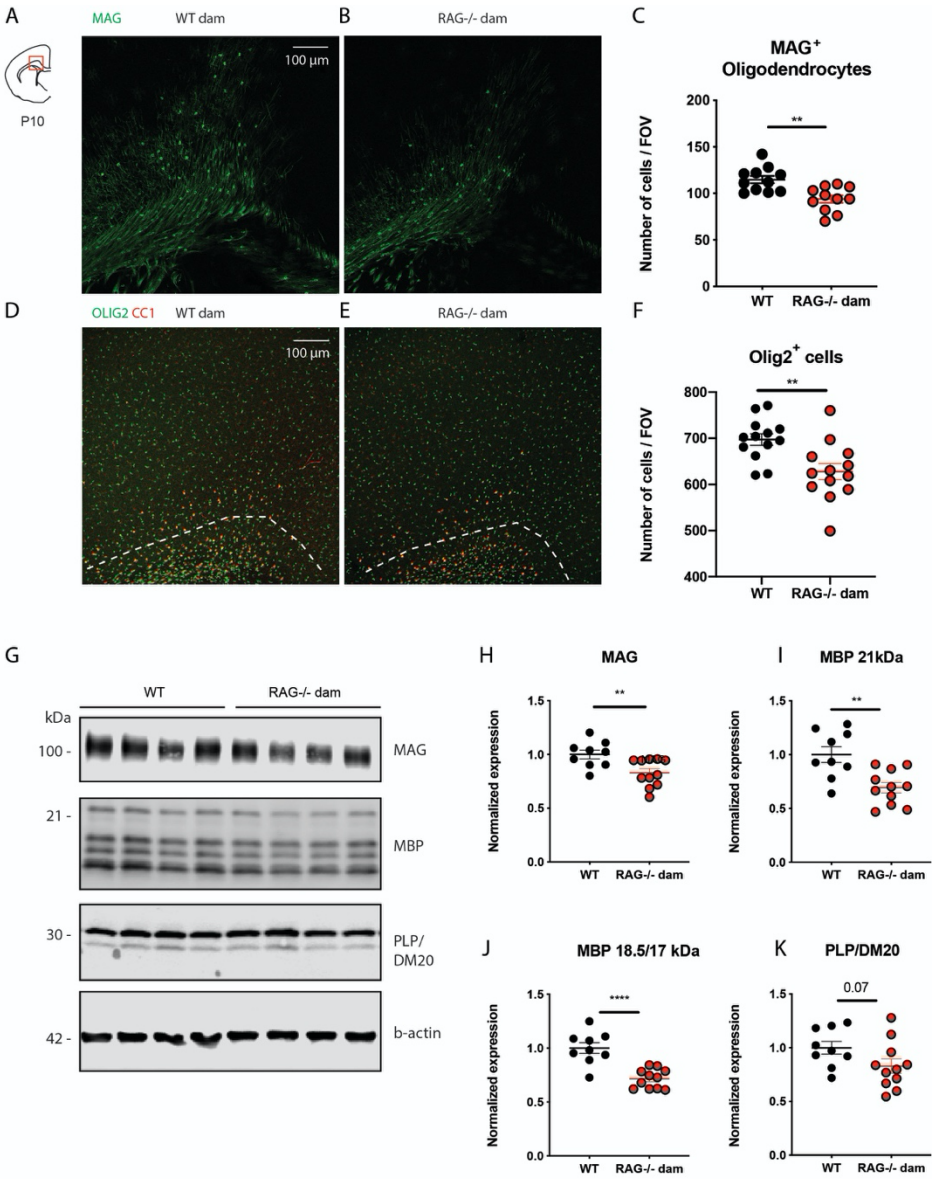

Figure 16 Mice deprived of Maternal Immunoglobulin Display Lower Myelin Protein Expression in Early Postnatal Life.

A-B Representative immunofluorescence staining in the area shown for MAG$^+$ myelinating oligodendrocytes from pups born to WT or RAG-/- dams. P10 postnatal day 10. **C** Quantification of the number of MAG$^+$ oligodendrocytes per field of view (FOV). N=11 pups WT (3 dams), N=11 pups RAG-/- (2 dams). P=0.0014. **D-E** Representative immunofluorescence staining in the area shown for Olig2$^+$ oligodendrocytes and oligodendrocyte precursor cells from pups born to WT or RAG-/- dams. P10 postnatal day 10. **F** Quantification of the number of OLIG2$^+$ cells per field of view (FOV). N=13 pups WT (4 dams), N=13 pups RAG-/- (3 dams). P=0.0036. **G** Representative immunoblots of P7 spinal cord from pups born to WT dams or RAG-/-. **H-K** Quantification of immunoreactivity for MAG (p=0.0071), MBP 21kDa (p=0.0020), MBP 18.5/17kDa (p<0.0001), and PLP/DM20 (p=0.07). N=9 pups WT (3 dams), N=11 pups RAG-/- (3 dams).

4.3.3 Mice Deprived of Maternal Immunoglobulin Display Thinner Axons in the Corpus Callosum

Myelin sheets concentrically wrap around the axon and the thickness of the wrapping is relatively constant in the healthy brain, with some variations during development and learning (Hughes et al., 2018). Mice lacking IgG postnatally displayed fewer MAG^+ oligodendrocytes and lower myelin protein expression at postnatal days 10 and 7, respectively. Further, mice lacking the mandatory subunit for the IgG receptor in the brain, *Fcer1g*, displayed a severe hypomyelination phenotype in electron microscopy studies (Nakahara et al., 2003). To test whether mice lacking IgG postnatally show abnormal myelin ultrastructure, ultrathin sections of the corpus callosum were prepared from P28 mice born to wildtype or $RAG2^{-/-}$ dams. During this process, care was taken to prepare a highly reproducible region, by first cutting 80 µm coronal slices using a vibratome, followed by embedding of a rectangular portion of the slice at bregma -0.94 for slicing mm (Figure 17A). Electron micrographs of the dorsal corpus callosum showed overall comparable morphology on a gross level between slices of mice born to wildtype or $RAG2^{-/-}$ dams (Figure 17B-E). The *g*-ratio, as a metric for the relative thickness of the myelin sheath in cross-sectional micrographs (Rushton, 1951), was measured using MyelTracer. Regression relationships showed that the relative thickness of the myelin sheath was indistinguishable in mice born to wildtype or $RAG2^{-/-}$ dams (Figure 17F, wildtype dam: slope 0.1586, y-intercept 0.6765, n = 455, $RAG2^{-/-}$ dam: slope 0.1545, y-intercept 0.6849, n = 496, slopes p = 0.7805, intercept p = 0.1100). Similarly, the *g*-ratio averaged across all axons per mouse was comparable between mice born to wildtype or $RAG2^{-/-}$ dams (Figure 17G, WT dam mean ± SEM: 0.7568 ± 0.0005, n = 6 mice, $RAG2^{-/-}$ dam: 0.7613 ± 0.01, n=6, p = 0.7005). Next, we probed whether there was a difference between mice born to wildtype or $RAG2^{-/-}$ dams regarding the fraction of myelinated axons, which was reduced about 50% in *Fcer1g* mice in the Nakahara study (Nakahara et al., 2003). The fraction of myelinated axons is calculated as the number of myelinated axons divided by the total number of

axons, including small caliber axons which are numerous at this age (Figure 17C, E). Comparing the two groups, I did not find a significant difference in the fraction of myelinated axons, albeit there was a trend (Figure 17H, WT dam mean ± SEM: 12.57 ± 1.396%, n = 7 mice, RAG2$^{-/-}$ dam: 9.547 ± 0.6187%, n=7, p = 0.07). To evaluate this more closely, the number of axons per area was plotted. Comparing the two groups, I found that the axonal density is greater in the mice born to the RAG2$^{-/-}$ dam compared to the mice born to wildtype dams (Figure 17I, WT dam mean ± SEM: 5209 ± 357.6 axons/mm^2, n = 7 mice, RAG2$^{-/-}$ dam: 7387 ± 611.2 axons/mm^2, n=7, p = 0.0096). In line with this, there was a trend for reduced axonal diameter of larger myelinated and unmyelinated axons in mice from RAG2$^{-/-}$ dams compared to those from wildtype dams (Figure 17J, WT dam mean ± SEM: 0.5409 ± 0.014 µm, n = 7 mice, RAG2$^{-/-}$ dam: 0.5055 ± 0.013 µm, n=7, p = 0.08). To further examine this, hundreds of axons measured for each animal were binned at 0.1 µm and the frequency distribution of axonal diameters assessed. Plotting the frequency distribution further showed that there was a significantly higher ratio of small axons and a leftward shift of the distribution in the mice from RAG2$^{-/-}$ dams compared to those from wildtype dams (Figure 17K, WT dam mean for 0.2 µm bin: 5.7%, n = 7 mice, RAG2$^{-/-}$ dam: 9.3%, n=7, padj = 0.011, WT dam mean for 0.3 µm bin: 17.97%, n = 7 mice, RAG2$^{-/-}$ dam: 21.51%, n=7, padj = 0.012). Together, these data show that while the myelin morphology is normal in P28 mice from RAG2$^{-/-}$ dams, the morphology of axons is affected, such that they are overall slightly thinner.

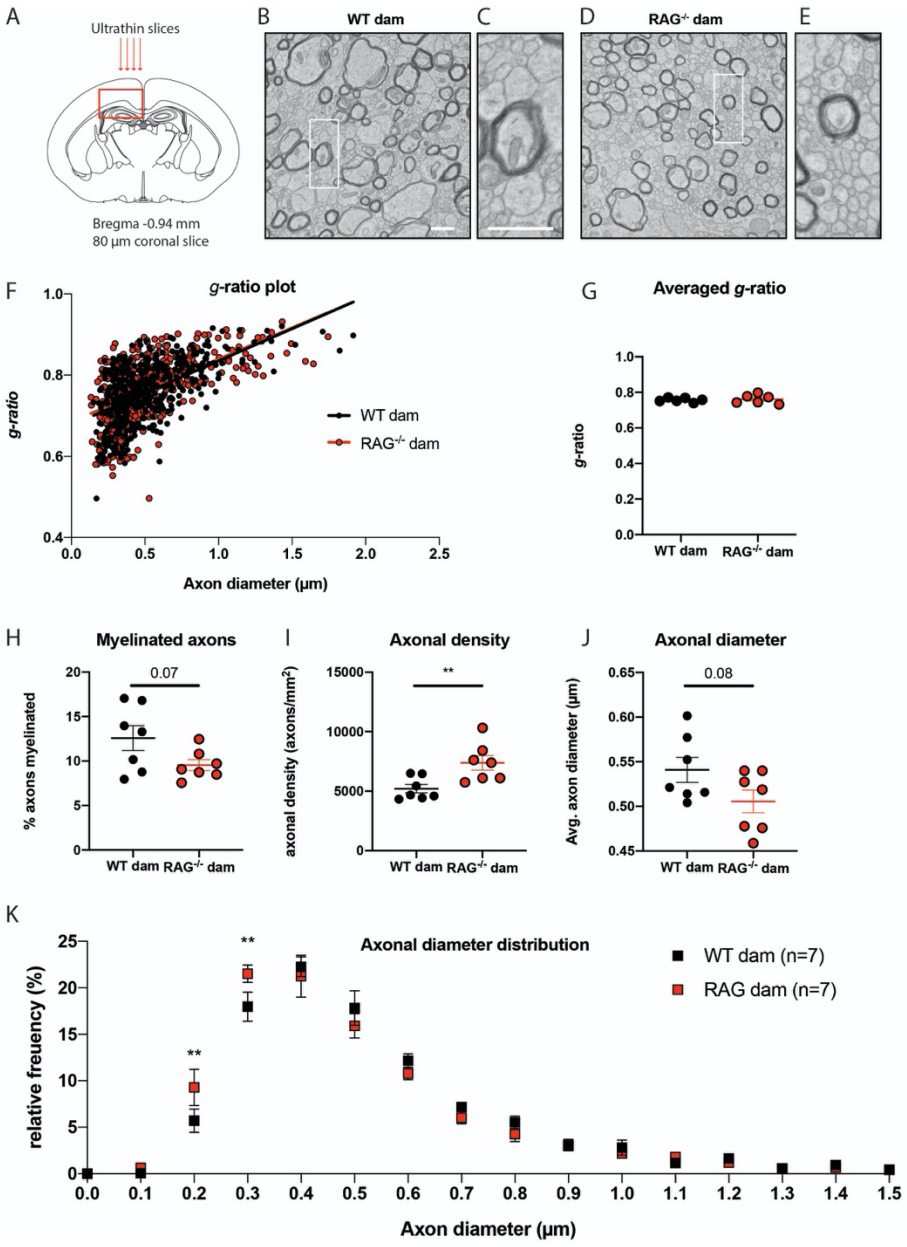

Figure 17 Mice Deprived of Maternal Immunoglobulin Display Subtle Abnormalities in the Corpus Callosum

A Schematic of ultrathin slicing to prepare electron microscopy samples from the same reproducible region. **B-E** Representative electron micrographs of the dorsal corpus callosum from P28 mice born to WT dams or RAG-/- dams. Scale bar 1 µm. **F** *g*-ratio scatter plot from P28 mice born to WT dams or RAG-/- dams. ANCOVA test p-value=0.7805 (slopes) and p=0.11 (intercepts), n=455 axons WT (n=6 mice, 3 dams), n=496 axons RAG-/- (n=6 mice, 3 dams). ***G***, Averaged *g*-ratios per mouse. Unpaired t-test p=0.7005, n=6 mice each. **H** Fraction of myelinated axons. Unpaired t-test P=0.0708, n=7 each. **I** Axonal density as number of all axons per area. Unpaired t-test **P=0.0096, n=7 each. **J** Axonal diameter of myelinated and unmyelinated larger axons. Unpaired t-test **P=0.0862, n=7 each. **K** Frequency-distribution of axonal diameters across P28 mice born to WT or RAG-/- dams. **Padj$_{0.02µm}$=0.011, **Padj$_{0.03µm}$=0.012, n=7 each.

4.3.4 The IgG Receptor Subunit Fcer1g is Exclusively Expressed by Microglia

Deletion of *Fcer1g* is reported to result in a hypomyelination phenotype (Nakahara et al., 2003) and mice lacking maternal IgG postnatally display abnormalities in early myelin development and in the maturing corpus callosum at P28 (Figures 16 and 17). In the postnatal brain, IgG localizes to microglia, presumably through binding to one of the Fc-receptors that employs the obligatory subunit FCER1G, which is amongst the 20 most enriched genes in microglia (Figure 15, Figure 18A. Conversely, Nakahara and coworkers find that the Fc-receptor subunit *Fcer1g* is expressed by oligodendrocyte precursor cells in the corpus callosum (Nakahara et al., 2003). To examine whether *Fcer1g* is only expressed by microglia or also in cells of the oligodendrocyte lineage, I first examined bulk and single cell RNA sequencing datasets. Zhang and coworkers prepared microglia and OPCs by immunopanning at P17 and performed bulk sequencing (Zhang et al., 2014). In this dataset, microglia highly express *Fcer1g*, while OPC express very low amounts that are in all likelihood due to the contamination with 5% of microglia reported by the authors for this protocol (Figure 18B). Similarly, in Li et al's microglia single-cell RNA sequencing data set, it is apparent that *Fcer1g* is highly expressed in all *Cx3cr1*-expressing subsets of microglia (Figure 18C, D, Li et al., 2019). In contrast, *Fcer1g* is not expressed in the OPC dataset from Marques and coworkers (4E, F, Marques et al., 2016)). To expand these findings and test *Fcer1g* expression *in vivo* at P7, both OPCs ($PDGFRa^{+}$) and microglia ($CD11b^{+}$ $CD45^{lo/int}$) were acutely isolated (Figure 18G, H). Using qPCR on mRNA isolated from the sorted cells, I observed that while microglia expressed *Fcer1g*, OPCs did not (Figure 18I). Together, these observations support the conclusion that *Fcer1g* is only expressed in microglia in the developing brain.

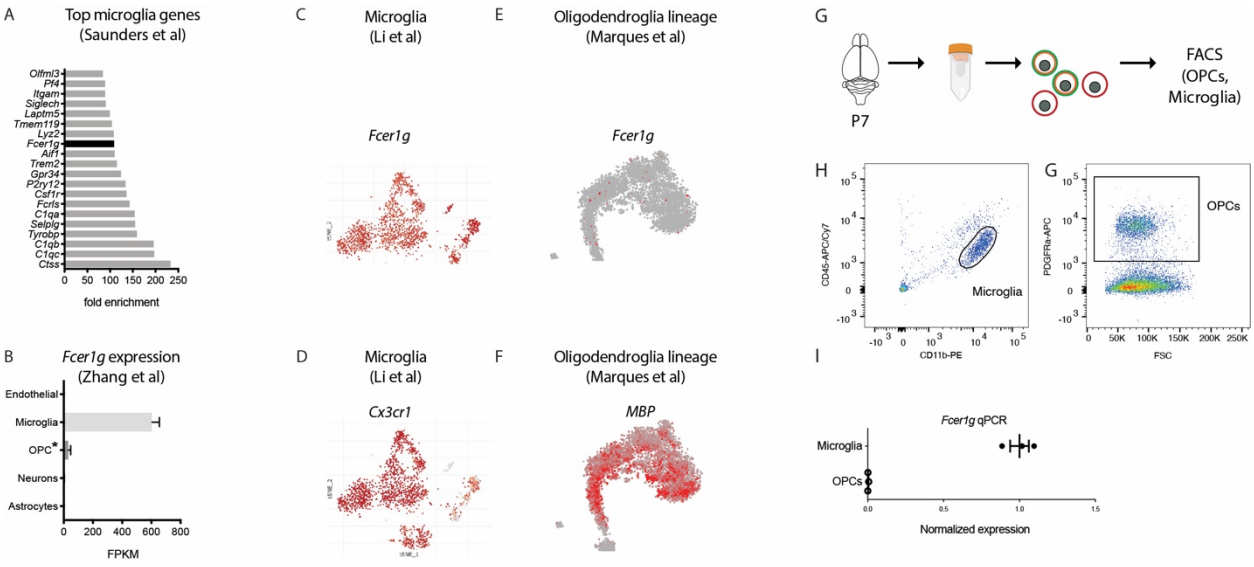

Figure 18 The IgG Receptor Subunit *Fcer1g* is Highly Enriched by Microglia in the Brain

A The 20 most-enriched genes based on the Saunders et al single-cell sequencing dataset for microglia (Saunders et al., 2018). **B** *Fcer1g* gene expression for different sorted or immuno-panned and bulk-sequenced cell types. * The OPC dataset contains 5% microglia contamination in this study (Zhang et al., 2014). **C-D** t-Distributed stochastic neighbor embedding projection for *Fcer1g* and *Cx3cr1* in a microglia single-cell dataset (Li et al., 2019). **C-D** t-Distributed stochastic neighbor embedding projection for *Fcer1g* and *MBP* in a oligodendrocyte lineage single-cell dataset (Marques et al., 2016) **G** Schematic of experiment to isolate microglia and OPCs from P7 brain. **H** Representative pseudocolor plots of fluorescence-activated cell sorting for microglia and OPCs. **I** Quantitative real-time PCR of *Fcer1g* transcript expression among microglia and OPCs. N=3 per genotype. ****P<0.0001.

The bulk RNA sequencing, single-cell RNA sequencing and qPCR data from acutely isolated microglia and OPCs point to exclusive expression of *Fcer1g* by microglia, not OPCs in the developing brain. However, there are several limitations to these findings: (1) they lack spatial information, (2) depend on the stringency of dissociation across brain regions and single-cell suspension preparation, and (3) dissociation protocols may artificially impact transcripts, which altogether give rise to the possibility that *Fcer1g* amongst OPCs within the corpus callosum *in vivo* could be missed. To further test this, corpus callosum tissue from postnatal day 7 mice was prepared by either flash freezing or fixation with paraformaldehyde for fluorescence in-situ

hybridization or immunofluorescence staining, respectively (Figure 19A). Using the highly RNAscope V2 chemistry, *Fcer1g* was detected within *Fcrls*-expressing microglia in the corpus callosum, whereas no colocalization was observed with *Olig2*-expressing cells of the oligodendrocyte lineage (Figure 19B-F). Similarly, immunofluorescence staining for FCER1G completely colocalized with IBA1 immunoreactivity, with no FCER1G+ signal emanating from OLIG2+ cells (Figure 19G-M). Together, these *in vivo* RNA and protein expression data demonstrate that *Fcer1g* is only expressed by myeloid cells in the developing corpus callosum.

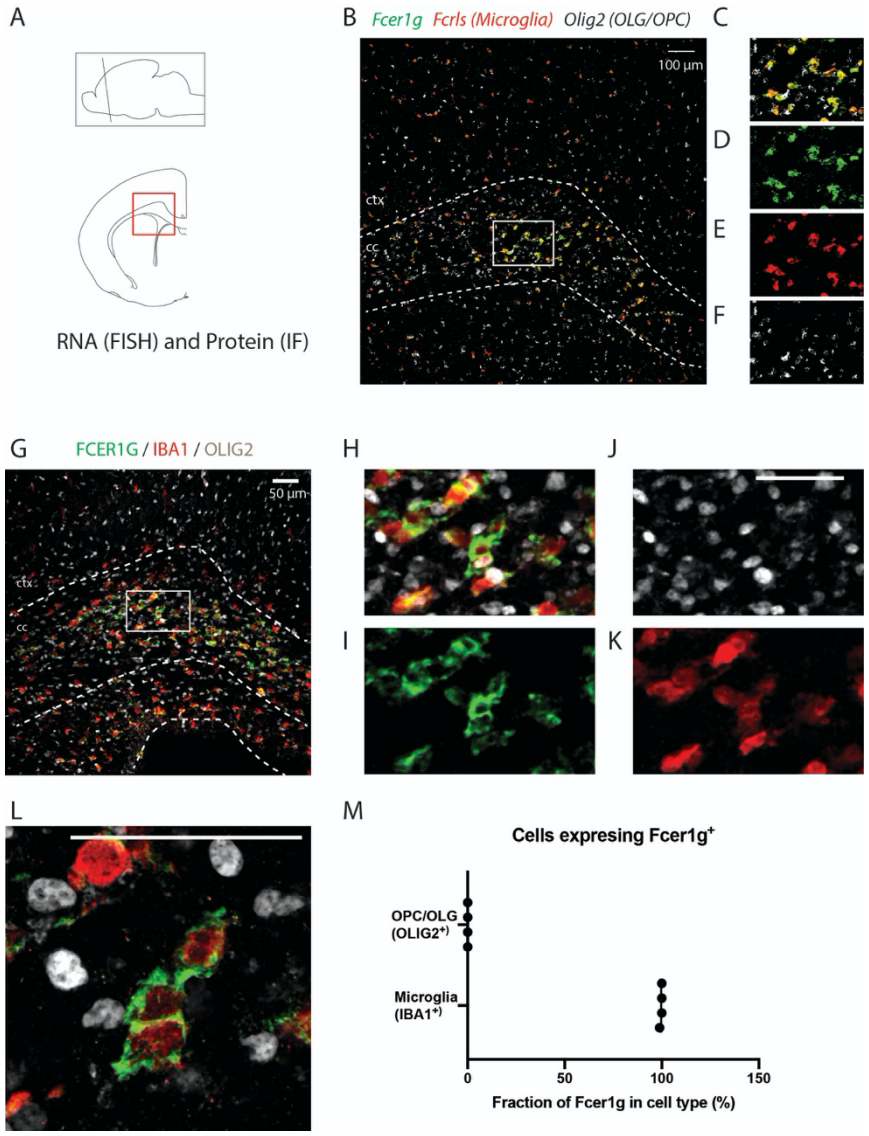

Figure 19 The IgG Receptor Subunit *Fcer1g* is Expressed by Microglia But Not OPCs in the Corpus Callosum
A Schematic of representative region for fluorescence in-situ hybridization (FISH) or immunofluorescence (IF) staining of mouse brains at postnatal day 7. **B-F** Representative confocal micrographs of fluorescence in-situ hybridization using RNAscope V2 chemistry for *Fcer1g, Fcrls* (microglia marker)*, and Olig2* (OPC/Oligodendrocyte marker). **G-K** Representative confocal micrographs of immunofluorescence staining for FCER1G, IBA1 (microglia marker), and OLIG2. Ctx cortex. Cc corpus callosum. **L** High power confocal micrograph of the corpus callosum. Scale bar 50μm. **M** Scatter plot of FCER1G+ colocalization with OLIG2+ and IBA1+ cells. N=4 mice. ****P<0.0001.

4.3.5 Generation of an Fcer1g Conditional Knock-out Mouse

The *Fcer1g* RNA and FCER1G protein expression data strongly suggest that the early myelin and axon tract abnormalities seen in IgG-deficient pups and the reported hypomyelination phenotypes in *Fcer1g*-deficient mice are due to a lack of the receptor on microglia. To functionally test this possibility, I generated a conditional knockout allele (Figure 20A). FCER1G is a relatively small protein of 86 amino acids, encoded by *Fcer1g* that consists of five exons and 4 introns spanning approximately 5 kb. In analogy to the constitutive knockout mouse employed by Nakahara et al, the transmembrane domain-encoding exon 2 was targeted (Nakahara et al., 2003). In addition, exon 3 was included due to the small size of intron 2 and the availability of non-conserved regions within intron 1 and intron 3 for the placement of loxP sites. Excision of exon 2 and 3 will lead to premature stop codon in exon 5 and a truncated 34 amino acid peptide that lacks the transmembrane domains and the interchain disulfide acceptor. Further, splicing should be unaffected and *Fcer1g* properly expressed in homozygous floxed animals. Two crRNAs and a double strand DNA donor template containing 1500 bp homology arms were designed and injected into zygotes. Zygotes were implanted into surrogates and 6 founder animals 4042-4047 were born. To determine founder animals with insertion of loxP sites at the correct positions, three PCR reactions were carried out followed by Sanger sequencing of the products from the reactions

spanning the homology arms boundaries (Figure 20B-F). Placement of the loxP sites was observed for founder 4044 and 4045, while the other mice presumably had full or partial off-target insertions that rendered them positive for PCR1, but which were not further investigated. Founders 4044 and 4045 were backcrossed to C57BL/6J and F1 offspring mated within each line to generate homozygous F2 4044 Fx/Fx and 4045 Fx/Fx animals. To test whether FCER1G expression is preserved in Fx/Fx animals, mice were sacrificed at postnatal day 7 and brains were immunostained for FCER1G. Comparing both 4045 and 4044 Fx/Fx to wildtype animals, it was found that 4045 animals express FCER1G indistinguishable from wildtype mice, whereas 4044 Fx/Fx animals are devoid of any FCER1G expression (Figure 20G-J). This suggests that the 4045 line is fully functional and the 4044 line functionally a null. To investigate this difference, a large fragment spanning the entire genomic sequence from exon 1 to exon 5 was amplified in PCR4. Agarose gel electrophoresis revealed a band at the expected size in wildtype and 4045 animals, while the PCR from the 4044 animals only yielded product at the size of a predicted off-target site of the primers (Figure 20K). This suggests that one or both of the primer binding sites in exon 1 or 5 is eliminated in the 4044 line, possibly due to a large deletion outside the homology arms. Together, these data show that a conditional allele for *Fcer1g* was successfully created in the 4045 line, whereas a second founder line resulted in a functional knockout.

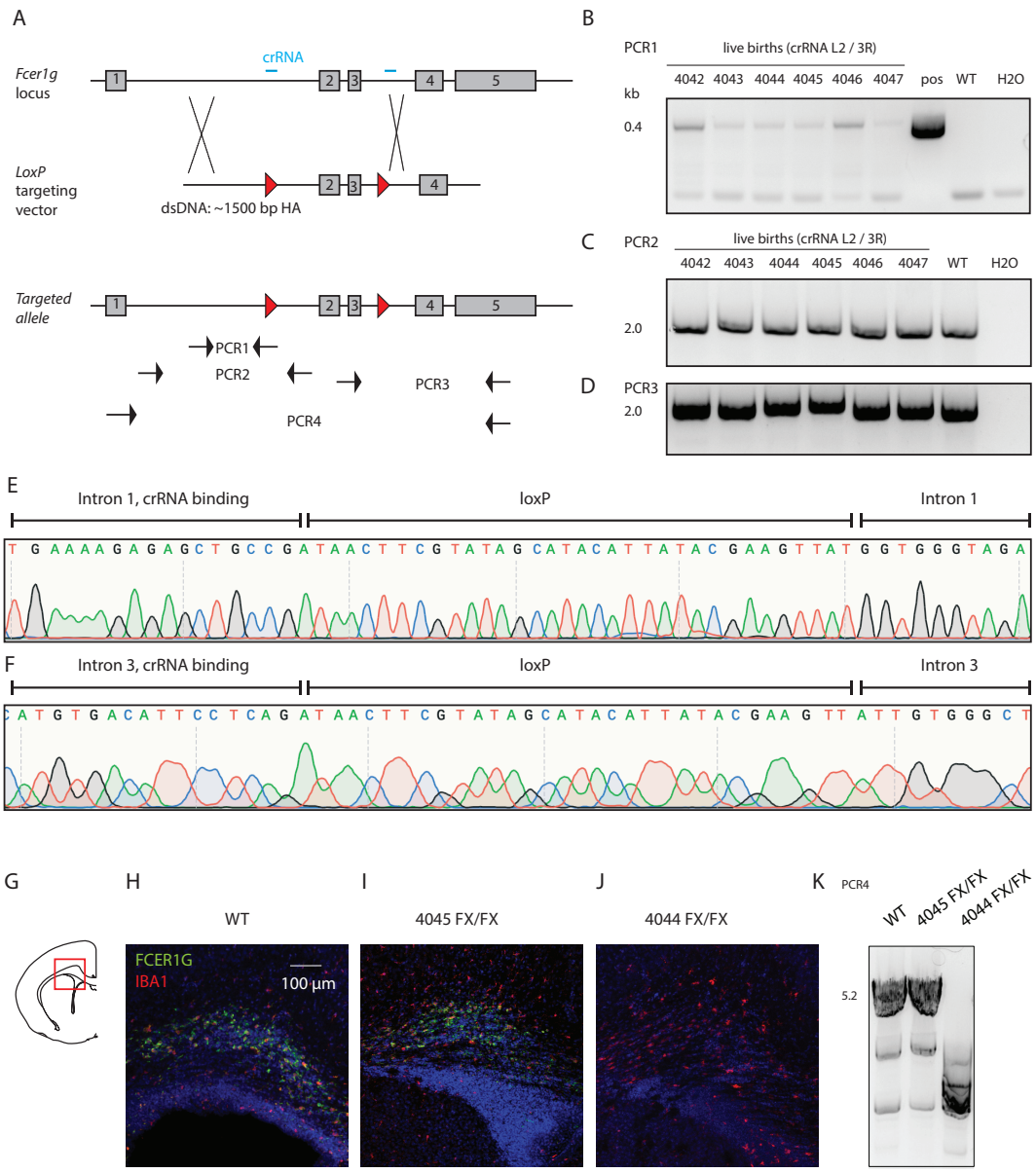

Figure 20 Generation of an *Fcer1g FX* Conditional Knock-out Mouse

A Schematic of transgenic strategy using two crRNAs (blue bars) and a double strand DNA (dsDNA) donor with 1.5 kb homology arms (HA) to generate Fcer1g loxP (FX) mice. Several PCR primers are indicated for assessment of correct knock-in (arrows). **B-D** Representative agarose gel electrophoresis images of indicated PCR reactions for six live-born pups. PCR1 covers part of intron 1 and the loxP site. PCR2 and PCR3 amplify DNA outside-in and inside-out, extending beyond the homology arms. kb kilobases. **E** Sanger sequencing across the loxP sites on PCR products from PCR2 and PCR3. **G** Schematic of representative region for immunofluorescence staining of mouse brains at postnatal day 7. **H-J** Representative immunofluorescence staining in WT, 4045 founder FX/FX, and 4044 founder FX/FX mice. **K** Representative agarose gel electrophoresis image for an amplicon spanning the entire genomic region of *Fcer1g*.

4.3.6 Mice with Microglia-specific Deletion of *Fcer1g* Develop Normal Myelin Postnatally

Cell-type specific studies of *Fcer1g* hinge on a Cre driver line, ideally with high fidelity and completion and no phenotypic impairments stemming from the Cre transgene placement. In this case specifically, it was reasoned that a Cre line would display great recombination efficacy early in development in all microglia subsets, especially microglia in the white matter where FCER1G staining is most concentrated (Figure 19G). Further, fidelity would be beneficial, but could be compromised on if *Fcer1g* is not expressed in the ectopic cell type and if the cell type is reasonably unlikely to play a role in myelination. *Tie2-Cre* was considered a good candidate due to the expression in yolk-sac precursors of microglia and off-target expression in endothelial cells (Kisanuki et al., 2001 p.2). To test the recombination efficacy of *Tie2-Cre* in early postnatal microglia, the Cre driver was crossed to Ai14 tdTomato reporter mice (Figure 21A) and slices were prepared from the corpus callosum at P7 (Figure 21B). Using immunofluorescence staining, expression of tdTomato was observed in endothelial cells and all IBA1-positive microglia in the corpus callosum (Figure 21C-G). These data indicate that the *Tie2-Cre* line is suitable for relatively microglia-specific ablation of *Fcer1g* with high efficacy.

To test whether microglial *Fcer1g* is required for myelination during early postnatal development, the 4045 *Fcer1g Fx* mice, hereinafter referred to as *Fcer1g Fx*, was crossed to *Tie2-Cre* mice (Figure 21H). Mice were bred to generate *Fcer1g Fx/Fx* and *Fcer1g Fx/Fx; Tie2-Cre* littermates, perfused and immunostained for FCER1G (Figure 21I-K). Confocal microscopy revealed that *Fcer1g Fx/Fx; Tie2-Cre* lacked FCER1G expression, indicating that Tie2-Cre recombines the loxP allele with high efficacy in microglia. Slices from the same littermates were stained for MAG-positive oligodendrocytes in the corpus callosum region at postnatal day 10 (Figure 21L-N). MAG-positive cells were observed in similar numbers in the corpus callosum of *Fcer1g Fx/Fx* and *Fcer1g Fx/Fx; Tie2-Cre* mice and there was no statistically significant

difference (Figure 21O, *Fx/Fx* mean ± SEM: 68.11 ± 5.032 cells/FOV, n = 7 mice, *Fx/Fx; Tie2-Cre*: 66.08 ± 4.555 cells/FOV, n=9, p = 0.7704). These results show that microglial *Fcer1g* deletion does not lead to a defect in early myelin development. They further suggest either that *Fcer1g* exerts its role through a non-myeloid cell type, or that the *Fcer1g Fx* allele is does not recapitulate the original *Fcer1g* knockout allele.

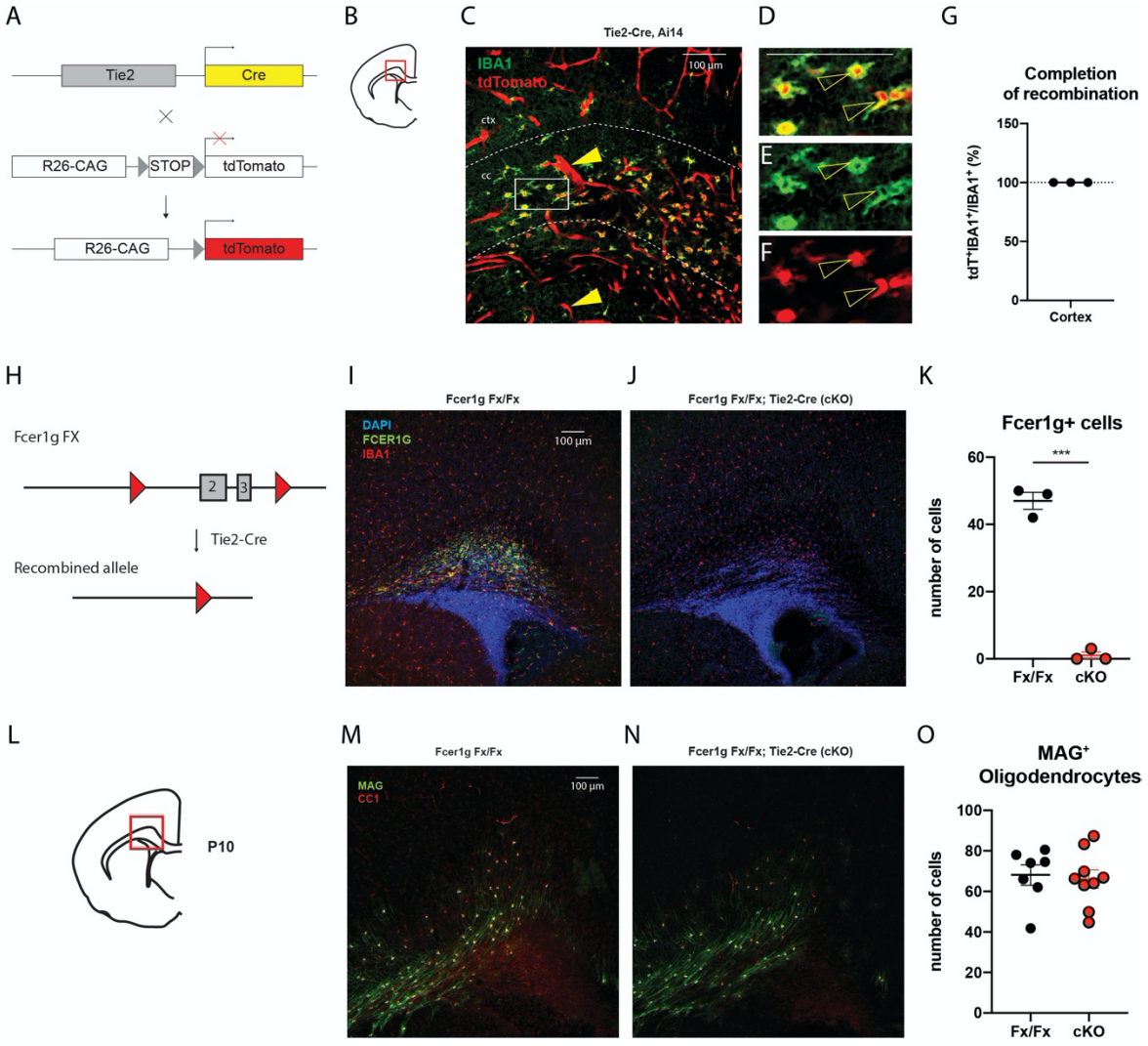

Figure 21 Mice with Microglia-specific Deletion of *Fcer1g* Develop Normal Myelin Postnatally

A Schematic of experiment to assess capabilities of the Tie2-Cre mouse line to recombine floxed alleles in early postnatal microglia. **B** Schematic of representative region for immunofluorescence staining of mouse brains at

postnatal day 7. **C-F** Representative confocal micrographs of the corpus callosum from Tie2-Cre; Ai14 mice. Ctx cortex. CC corpus callosum. Solid arrowheads blood vessels. Open arrowheads microglia. **G** Scatter plot of tdTomato+/IBA+ cell amongst IBA1+ cells. N=3 mice. **H** Schematic of Fcer1g FX/FX recombination by Tie2-Cre for conditional knockout in microglia. **I-J** Representative confocal micrographs of FCER1G immunofluorescence staining of the corpus callosum from Fcer1g Fx/Fx and Fcer1g Fx/Fx; Tie2-Cre mice. **K** Scatter plot comparing the number of FCER1G+ positive cells in the corpus callosum between Fcer1g FX/FX and Fcer1g FX/FX; Tie2-Cre mice at P10. **L** Schematic of representative region for immunofluorescence staining of mouse brains at postnatal day 10. **M-N** Representative confocal micrographs of MAG immunofluorescence staining of the corpus callosum from Fcer1g Fx/Fx and Fcer1g Fx/Fx; Tie2-Cre mice. **O** Scatter plot comparing the number of MAG^+ positive oligodendrocytes in the corpus callosum between Fcer1g FX/FX and Fcer1g FX/FX; Tie2-Cre mice at P10.

4.3.7 Mice with Constitutive Deletion of *Fcer1g* Develop Normal Myelin Postnatally

Using *Fcer1g Fx* mice for the conditional ablation of *Fcer1g* from microglia, I failed to observe any abnormalities in early postnatal myelin development akin to those observed in pups lacking maternal IgG (Figures 16 and 17) or those seen in a previous report (Nakahara et al., 2003). This appeared to be at odds with the conclusion that only microglia express *Fcer1g* in the brain (Figures 20 and 21) and that constitutive *Fcer1g* knockout mice show a strong hypomyelination phenotype (Nakahara et al., 2003). To test whether the hypomyelination phenotype seen in *Fcer1g* knockout mice can be reproduced, the original mice from Taconic were procured and the most significant myelin phenotypes previously described were examined. First, sections were prepared for immunofluorescence staining of the corpus callosum at postnatal day 10 (Figure 22A). MBP immunofluorescence appeared comparable between $Fcer1g^{-/-}$ and wildtype animals (Figure 22B, C). Further, the number of MAG-positive oligodendrocytes per field of view were indistinguishable between $Fcer1g^{-/-}$ and wildtype animals (Figure 22D-F, WT mean ± SEM: 132.9 ± 4.562 cells/FOV, n = 3 mice, $Fcer1g^{-/-}$: 139.0 ± 6.638 cells/FOV, n=3, p = 0.4932). Next, spinal cord samples from pups at postnatal day 7 were processed and immunoblotted for MAG, PLP, and MBP (Figure 22G). Using densiometric quantification of the immunoblotting signal, no

differences were observed for MAG (Figure 22H, WT mean ± SEM: 1.0 ± 0.09, n = 3 mice, *Fcer1g*$^{-/-}$: 0.8894 ± 0.12, n=3, p = 0.4959), PLP (Figure 22I, WT mean ± SEM: 1.0 ± 0.03, n = 3 mice, *Fcer1g*$^{-/-}$: 1.196 ± 0.1495, n=3, p = 0.2678), or MBP (Figure 22J, WT mean ± SEM: 1.0 ± 0.1, n = 3 mice, *Fcer1g*$^{-/-}$: 1.187 ± 0.09, n=3, p = 0.2311). Together, these findings suggest that constitutive *Fcer1g* knockout mice develop myelin normally during early postnatal development.

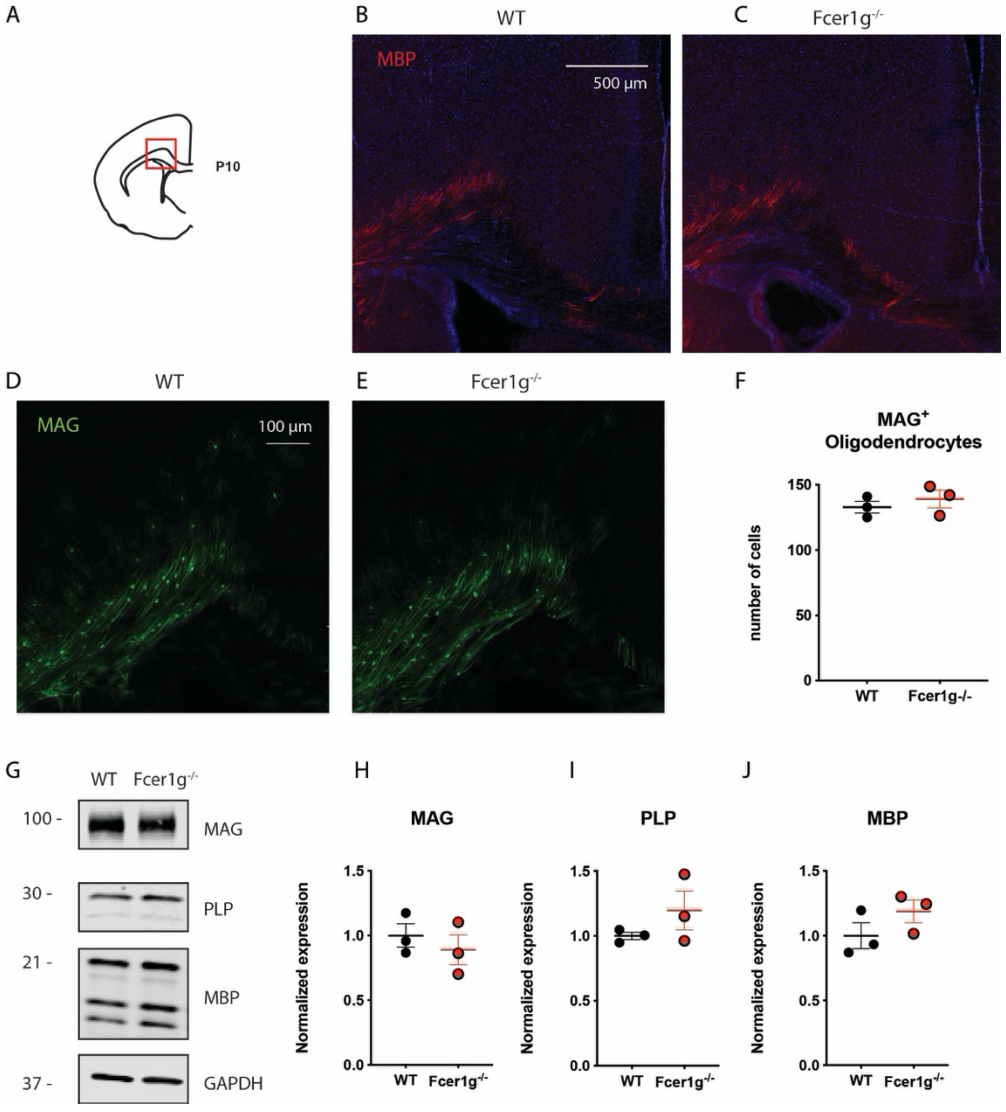

Figure 22 Mice with Constitutive Deletion of *Fcer1g* Develop Normal Myelin Postnatally

A Schematic of representative region for immunofluorescence staining of mouse brains at postnatal day 10. B-C Representative confocal micrographs of MBP immunofluorescence staining in the corpus callosum of WT and

Fcer1g-/- mice. D-E Representative confocal micrograph of MAG immunofluorescence staining in the corpus callosum of WT and *Fcer1g-/-* mice. **F** Scatter plot comparing the number of MAG^+ oligodendrocytes between WT and *Fcer1g-/-* mice. G Representative immunoblot images for P7 spinal cord of WT and *Fcer1g-/-* mice. H-J Scatter plot of normalized protein expression for MAG, PLP, and MBP for P7 spinal cord of WT and *Fcer1g-/-* mice. N=3 mice each.

4.3.8 Mice with Constitutive Deletion of Fcer1g Display Normal Myelin in Early Adulthood

In addition to abnormalities in early myelin development, mice lacking maternal IgG displayed some axon tract abnormalities in the corpus callosum at postnatal day 28 (Figure 17), albeit different in nature and not as striking as the abnormalities in myelin ultrastructure seen in *Fcer1g* knockout mice (Nakahara et al., 2003). To test whether the subtle phenotype of increased axonal density and reduced caliber is mediated through activating Fc-receptors and thus *Fcer1g*, brains from wildtype and $Fcer1g^{-/-}$ mice were processed for ultrathin electron microscopy sections of a highly reproducible region (Figure 23A). Axon and myelin cross-sectional electron micrographs of wildtype and $Fcer1g^{-/-}$ mice appeared similar and regression relationships between *g*-ratio and axon diameter were not significantly different between wildtype and $Fcer1g^{-/-}$ mice (Figure 23B-F, wildtype: slope 0.1574, y-intercept 0.7233, n = 88, $Fcer1g^{-/-}$: slope 0.1484, y-intercept 0.7308, n = 141, slopes p = 0.8391, intercept p = 0.6722). Similarly, *g*-ratios averaged for each mouse were indistinguishable between wildtype and Fcer1g-/- mice (Figure 23G, WT mean ± SEM: 0.8036 ± 0.005, n = 3 mice, $Fcer1g^{-/-}$: 0.8052 ± 0.007, n=3, p = 0.8611). Next, the fraction of myelinated axons, axonal density, and average axonal diameter were analyzed, and all found to be comparable between wildtype and $Fcer1g^{-/-}$ mice (Figure 23H-J). Finally, to probe whether $Fcer1g^{-/-}$ show a similar shift in axonal calibers as mice lacking IgG postnatally, the distribution of axonal diameters was plotted and found the be indistinguishable between wildtype

and *Fcer1g*$^{-/-}$ animals (Figure 23K). Together, these data suggest that the abnormalities seen in mice lacking maternal IgG are not mediated through Fc-receptors.

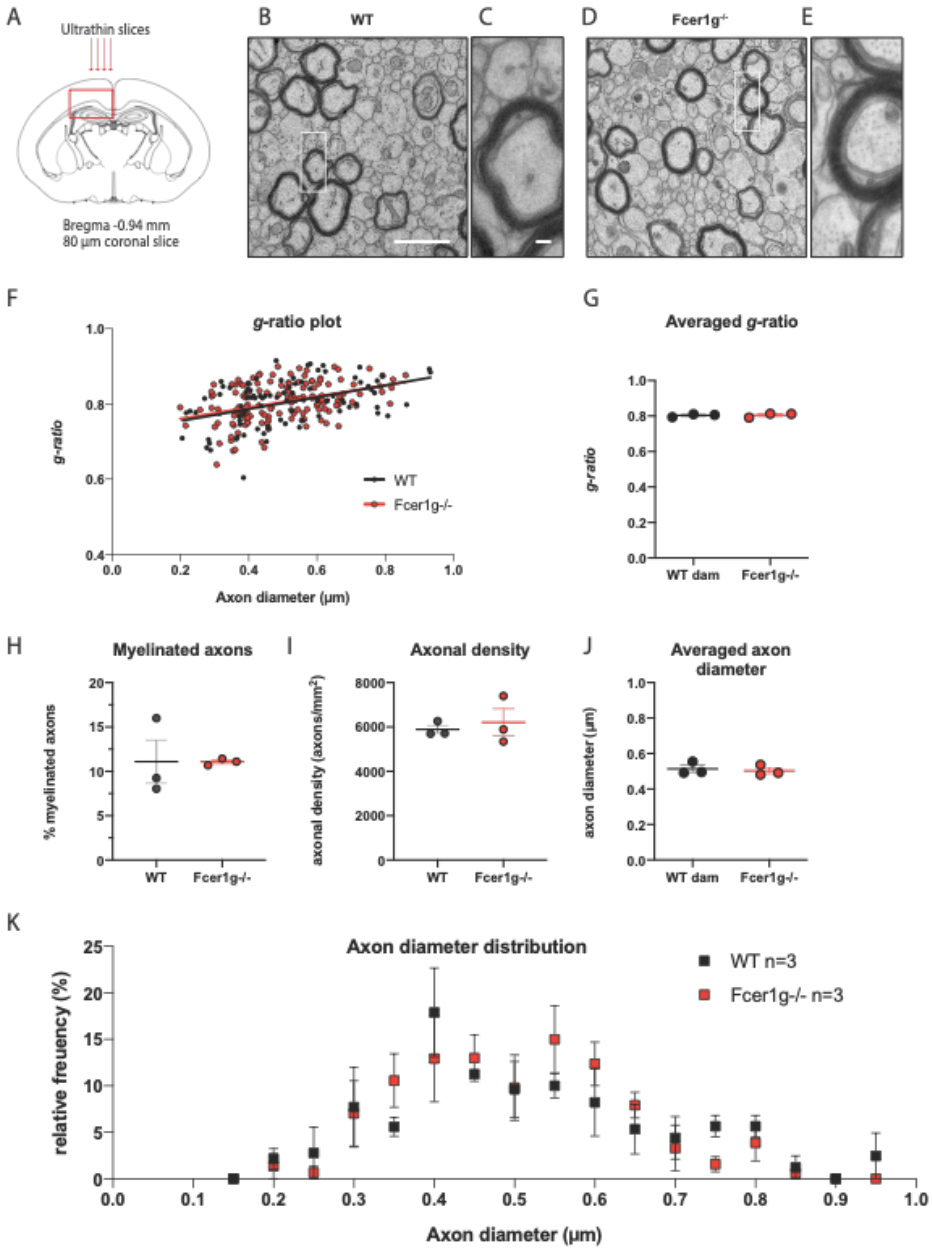

Figure 23 Mice with Constitutive Deletion of Fcer1g Display Normal Myelin in Early Adulthood

A Schematic of ultrathin slicing to prepare electron microscopy samples from the same reproducible region. **B-E** Representative electron micrographs of the dorsal corpus callosum from P28 WT and *Fcer1g*$^{-/-}$ mice. Scale bars 1 µm in B, 100 nm in C. **F** *g*-ratio scatter plot of P28 WT and *Fcer1g*$^{-/-}$ mice. ANCOVA test p-value=0.8391 (slopes) and p=0.6722 (intercepts), n=88 axons WT (n=3 mice), n=141 axons *Fcer1g*$^{-/-}$ (n=3 mice). ***G***, Averaged *g*-ratios per mouse. Unpaired t-test p=0.8611, n=3 mice each. **H** Fraction of myelinated axons. Unpaired t-test p=0.9934, n=3

each. **I** Axonal density as number of all axons per area. Unpaired t-test p=06447, n=3 each. **J** Axonal diameter of myelinated and unmyelinated larger axons. Unpaired t-test p=0.7016, n=3 each. **K** Frequency-distribution of axonal diameters across P28 WT and *Fcer1g*$^{-/-}$ mice. N=88 axons WT (n=3 mice), n=141 axons *Fcer1g*$^{-/-}$ (n=3 mice).

4.3.9 Drug-mediated Depletion of Microglia Does Not Clearly Cause Hypomyelination

IgG clearly localized to microglia in the brain during early postnatal development and canonical IgG receptors, namely activating Fc-receptors utilizing the obligatory subunit *Fcer1g* are highly expressed on microglia (Figures 15, 18, 19). Functionally, postnatal IgG appears to be required for some aspects of early myelin and axon tract development, yet its effect did not appear to be mediated by the Fc-receptors (Figures 16, 17, 21, 22, 23). To test whether microglia may play a role in these processes, as suggested by a previous report (Hagemeyer et al., 2017), two drug-mediated microglia depletion strategies were adopted. First, in analogy with the approach by Hagemeyer and coworkers, BLZ945, an orally active CSF-1R inhibitor was administered to mice at postnatal day 2, 3, and 5 (Figure 24A). Subsequently, tissue was harvested at postnatal day 7 for immunofluorescence staining and postnatal day 21 for immunoblotting. Staining for IBA1-positive microglia at postnatal day 7 indicated near complete ablation in BLZ945-treated mice compared to vehicle-treated littermates (Figure 24B-D, vehicle mean ± SEM: 100.0 ± 6.311%, n = 3 mice, BLZ945 13.59 ± 1.101%, n=3, p = 0.0002). This indicates that this paradigm using BLZ945 treatment during postnatal development leads to near complete ablation of microglia. Next, tissue was collected at postnatal day 21 from the hemispheres and the cerebellum. Protein lysates were prepared and immunoblots for MAG, PLP, and MBP performed (Figure 24E, I). Immunoblots were quantified and the expression of several myelin proteins was found to be significantly reduced in hemisphere samples from BLZ945-treated mice compared to vehicle-treated animals (Figure 24F-H). Similarly, reductions in these proteins were found in the cerebellum samples, albeit less robustly and only statistically significant for MBP (Figure 24J-L).

These findings from BLZ-mediated depletion are in line with the reported result, suggesting that microglia are required for early postnatal myelin development (Hagemeyer et al., 2017).

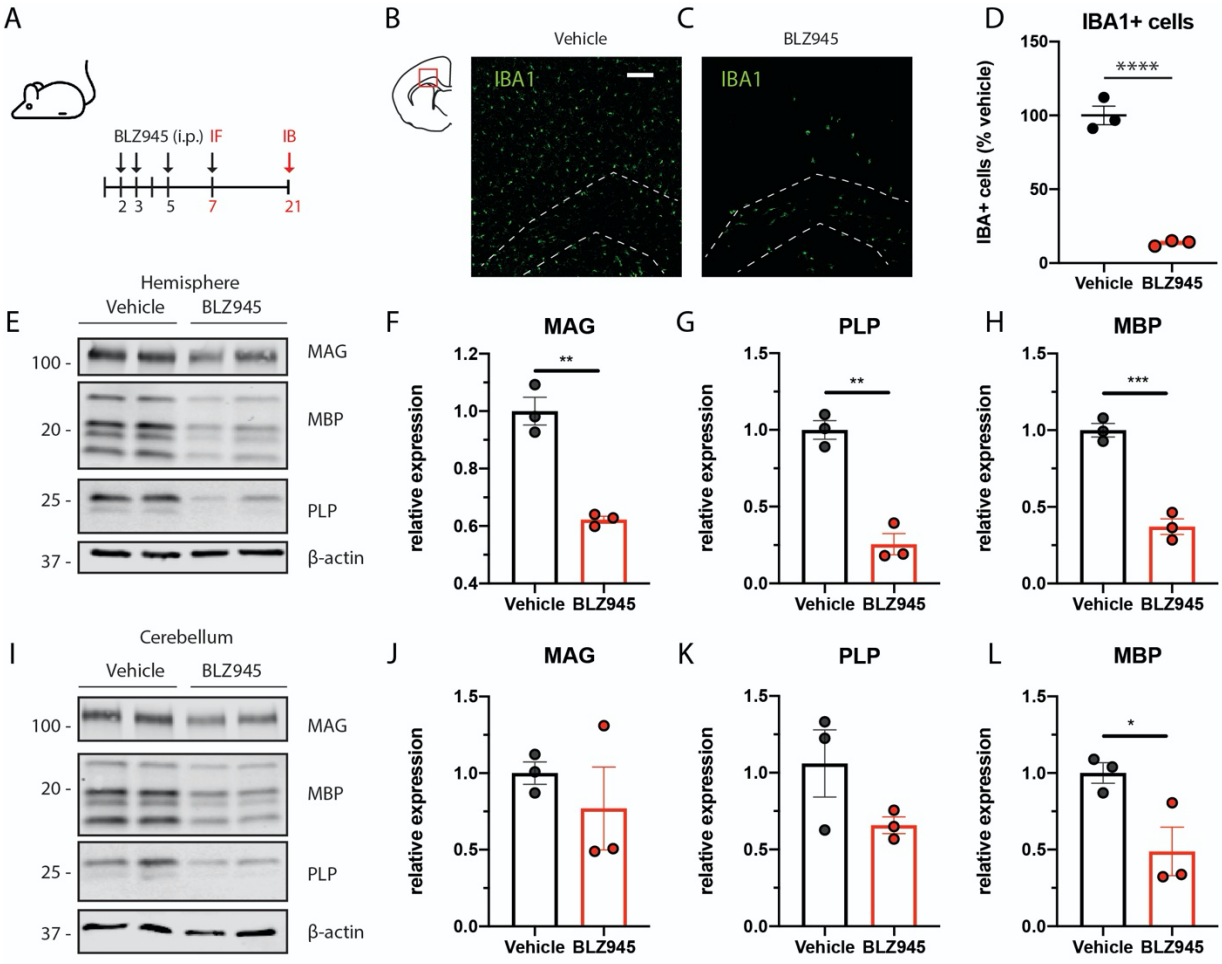

Figure 24 Postnatal Ablation of Microglia with the CSF1R Antagonist BLZ945 Impairs Myelination

A Schematic of the experimental paradigm from birth to postnatal day 21. i.p. intraperitoneal. IF Immunofluorescence staining. IB Immunoblotting. **B-C** Representative confocal micrographs of IBA1+ immunofluorescence staining of the corpus callosum region from mice treated with vehicle or BLZ945. **D** Scatter plot of the number of IBA1+ positive cells within field of view normalized to vehicle. **E** Representative immunoblot image of hemisphere samples prepared from vehicle- or BLZ945-treated animals at P21. **F-H** Quantification of immunoreactivity for PLP (**p=0.0013), MAG (**p=0.0017) and MBP (***p=0.0008). N=3 mice per group. **E** Representative immunoblot image of cerebellum samples prepared from vehicle- or BLZ945-treated animals at P21. **I-J** Quantification of immunoreactivity for PLP (p=0.1491), MAG (p=0.4556) and MBP (*p=0.0408). N=3 mice per group.

In addition to BLZ945 used by Hagemeyer and colleagues, a second complimentary drug-mediated microglia depletion protocol was used employing the more recently developed PLX5622, another CSF-1R inhibitor with increased specificity (Spangenberg et al., 2019). In this paradigm, mice were treated daily with 100 mg/kg PLX5622 from postnatal day 2 to 8 and tissue was collected for flow cytometry, immunofluorescence staining, and immunoblot at postnatal day 8, 10, and 21, respectively (Figure 25A). Immunofluorescence staining showed near complete ablation of IBA1-positive microglia in the cortex and corpus callosum (Figure 25B-D, cortex vehicle mean ± SEM: 100.0 ± 4.034%, n = 3 mice, PLX5622 4.134 ± 2.622%, n=3, $p < 0.0001$, corpus callosum vehicle mean ± SEM: 100.0 ± 4.325%, n = 3 mice, PLX5622 12.04 ± 4.383%, n=3, $p = 0.0001$). Similarly, flow cytometric measurement confirmed near complete elimination of $CD11b^{+}CD45^{lo/int}$ microglia in PLX5622-treated animals compared to vehicle-treated littermate controls (Figure 25E-G, vehicle mean ± SEM: 1884 ± 505 cells, n = 3 mice, PLX5622 20 ± 3 cells, n=3 vehicle, n=5 PLX5622, $p = 0.0023$). Surprisingly, when analyzing $PDGFRa^{+}$ OPCs, a statistically significant increase was observed in PLX5622-treated animals compared to their littermate controls (Figure 25H-J, vehicle mean ± SEM: 527 ± 24 cells, n = 3 mice, PLX5622 1336 ± 259 cells, n=3 vehicle, n=5 PLX5622, $p = 0.035$). Immunofluorescence analysis of MAG^{+} oligodendrocytes showed that vehicle- and PLX5622-treated were comparable (Figure 25K, L, vehicle mean ± SEM: 100 ± 9.3%, n = 3 mice, PLX5622 91.65 ± 4.4%, n=3, $p = 0.4636$). To further study correlates of myelination, PLX5622-injected mice were sacrificed at postnatal day 21 and protein lysates prepared in analogy to studies using BLZ945. Immunoblotting for MAG, PLP, and MBP did not reveal any significant difference in myelin protein expression between microglia-depleted compared to control animals (Figure 25M-T). Finally, body weights during postnatal development of mice treated with either drug were compared to their vehicle-treated

littermates and found to be significantly reduced in BLZ-treated animals, whereas PLX5622-treated animals developed normally (Figure 25U-V). Together, these results from the administration of the more specific CSF-1R inhibitor PLX5622 suggest that early myelin development can proceed normally in absence of microglia and that broadly disrupting microglia does not adversely affect early myelin development.

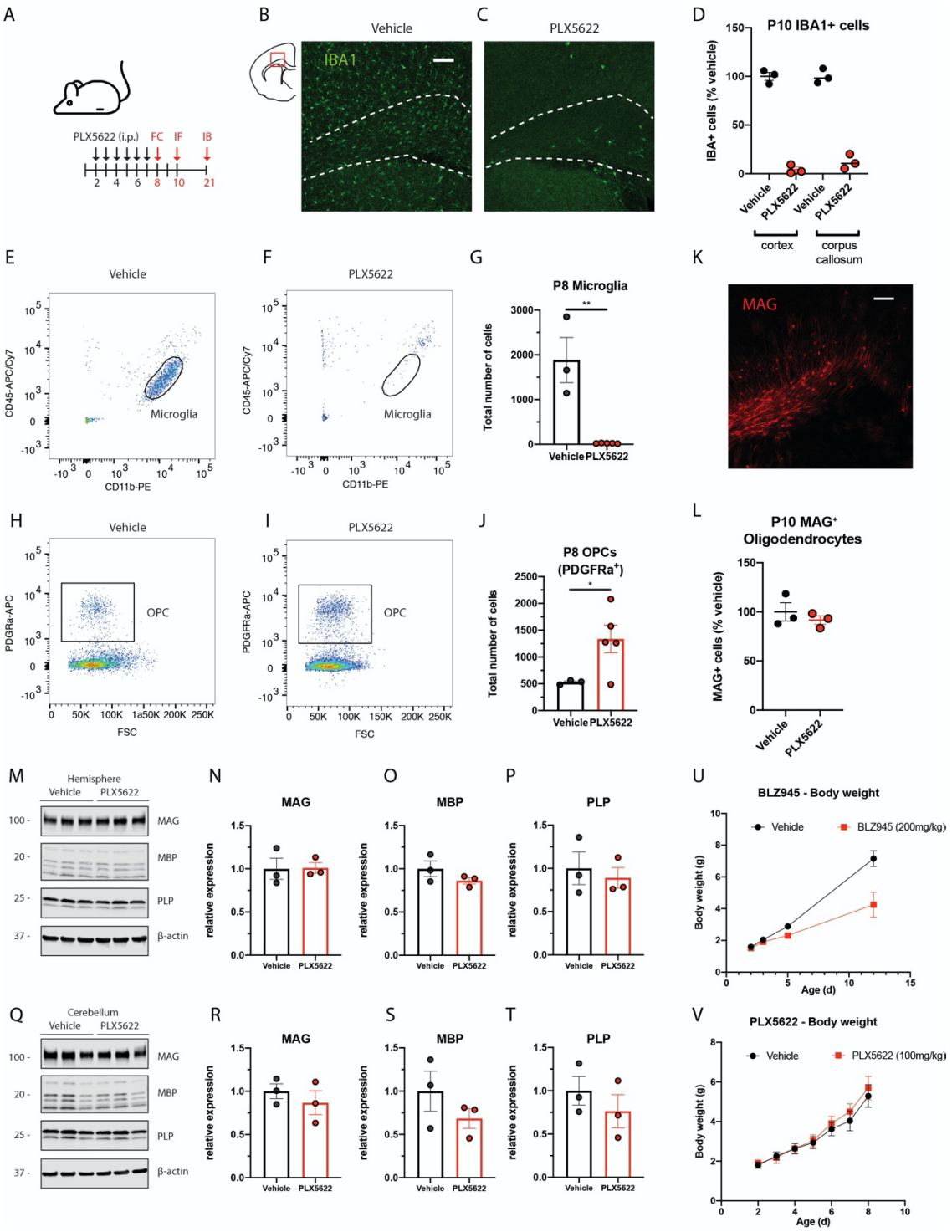

Figure 25 Postnatal Ablation of Microglia with the More Specific CSF1R Antagonist PLX5622 Does Not Impair Myelination

A Schematic of the experimental paradigm from birth to postnatal day 21. i.p. intraperitoneal. Arrows mark PLX5622 (100 mg/kg) intraperitoneal injection or tissue harvesting days. FC Flow cytometry. IF Immunofluorescence staining. IB Immunoblotting. **B-C** Representative confocal micrographs of IBA1+ immunofluorescence staining of the corpus

callosum region from mice treated with vehicle or PLX5622. **D** Scatter plot of the number of IBA1+ positive cells within field of view normalized to vehicle. **E-F** Representative pseudo-color flow cytometry plots for microglia (single cell, live, $Gr1^-$, $CD11b^+$, $CD45^{lo/int}$) in cell suspensions prepared from vehicle- or PLX5622-treated animals. **G** Scatter plot of the number of microglia in brain cell suspensions from vehicle- or PLX5622-treated mice. **p=0.0023. n=3 mice per group. **H-I** Representative pseudo-color flow cytometry plots for oligodendrocyte precursor cells (OPCs, single cell, live, $Gr1^-$, PDGFRa+) in cell suspensions prepared from vehicle- or PLX5622-treated animals. **J** Scatter plot of the number of OPCs in brain cell suspensions from vehicle- or PLX5622-treated mice. *p=0.035. n=3 mice per group. **K-L** Representative immunofluorescence image of MAG+ immunostained oligodendrocytes at P10 and scatter plot comparing vehicle- and PLX5622-treated animals. N=3 mice per group. Scale bar 100 µm. **M** Representative immunoblot image of hemisphere samples prepared from vehicle- or PLX5622-treated animals at P21. **N-P** Quantification of immunoreactivity for PLP, MAG and MBP. N=3 mice per group. **Q** Representative immunoblot image of cerebellum samples prepared from vehicle- or PLX5622-treated animals at P21. **R-T** Quantification of immunoreactivity for PLP, MAG and MBP. N=3 mice per group. **U-V** Body weight during postnatal development in control and BLZ945- or PLX5622-injected mice.

4.3.10 Mice Lacking Maternal IgG Harbor Fewer $Spp1^+$ Axon-Tract-Associated Microglia

During postnatal development, IgG appears to play a role in some aspects of early myelin and axon tract development (Figures 16, 17). Hypothesis-based testing ruled out that IgG's effect is mediated through its canonical Fc-receptors (Figures 21-23) and broad depletion of all microglia subsets also did not significantly affect myelination or phenocopy effects seen in mice lacking IgG postnatally (Figure 25). To probe whether IgG affects microglia in a more subtle way, an unbiased bulk RNA sequencing approach of sorted microglia was adopted. For this experiment, the intestinal IgG-transport-deficient *Fcgrt*$^{-/-}$ model was employed for IgG depletion (Figure 15-P-R, Roopenian and Akilesh, 2007), since it was crucial to analyze littermates from the same dam due to rapid maturation of microglia after birth (Bennett et al., 2016). Further, to maximize the number of littermates for comparison within one litter, heterozygous females were bred to homozygous males, resulting in 50% *Fcgrt*$^{-/-}$ and 50% *Fcgrt*$^{+/-}$ control animals, the latter of which harbor IgG amounts indistinguishable from wildtype animals (Figure 26A). To probe differences in transcriptomes between mice lacking IgG postnatally and controls, P7 pups were perfused with

ice-cold saline, brains were dounced ice-cold, single-cell suspensions were stained for microglia markers and sorted (Figure 26B, C). Single, live, $CD11b^{+}$, $CD45^{lo/int}$ cells were lysed and RNA prepared for RNA sequencing. Globally, RNA sequencing found transciptomes from $Fcgrt^{+/-}$ and $Fcgrt^{-/-}$ microglia. However, upon closer inspection, several genes were found the be reduced in mice lacking IgG postnatally. These genes included *Spp1* (Figure 26D, $Fcgrt^{+/-}$ mean ± SEM: 8.13 ± 0.07, $Fcgrt^{-/-}$ 7.179 ± 0.25, n=4 $Fcgrt^{+/-}$, n=3 $Fcgrt^{-/-}$, p = 0.0087), *Gpnmb* (Figure 26E, $Fcgrt^{+/-}$ mean ± SEM: 3.63 ± 0.16, $Fcgrt^{-/-}$ 2.75 ± 0.13, n=4 $Fcgrt^{+/-}$, n=3 $Fcgrt^{-/-}$, p = 0.01), *Lgals1* (Figure 26F, $Fcgrt^{+/-}$ mean ± SEM: 5.11 ± 0.07, $Fcgrt^{-/-}$ 4.854 ± 0.07, n=4 $Fcgrt^{+/-}$, n=3 $Fcgrt^{-/-}$, p = 0.05), and *Igf1* (Figure 26G, $Fcgrt^{+/-}$ mean ± SEM: 5.27 ± 0.08, $Fcgrt^{-/-}$ 5.03 ± 0.09, n=4 $Fcgrt^{+/-}$, n=3 $Fcgrt^{-/-}$, p = 0.11), all of which constitute the core signature of a recently identified subset of white-matter tract-associated microglia, also known as proliferative zone-associated microglia or axon-tract microglia (WAM, PAM, ATM, Wlodarczyk et al., 2017; Hammond et al., 2019; Li et al., 2019). To confirm these findings from RNA sequencing, qPCR was performed on the same samples as well as additional samples from a replication cohort. In this analysis, both *Spp1* (Figure 26H, $Fcgrt^{+/-}$ mean ± SEM: 1 ± 0.09, $Fcgrt^{-/-}$ 0.49 ± 0.06, n=11 $Fcgrt^{+/-}$, n=7 $Fcgrt^{-/-}$, p = 0.0016), and *Gpnmb* (Figure 26I, $Fcgrt^{+/-}$ mean ± SEM: 1 ± 0.11, $Fcgrt^{-/-}$ 0.48 ± 0.08, n=11 $Fcgrt^{+/-}$, n=6 $Fcgrt^{-/-}$, p = 0.0042) were reduced in $Fcgrt^{-/-}$ mice compared to control littermates. These data show that transcripts that are identifying for the white-matter associated subset of microglia (WAM) are reduced in acutely isolated microglia from mice lacking IgG postnatally.

Microglia from mice lacking IgG during postnatal development display reduced levels of *Spp1* and *Gpnmb*. There are several possibilities underlying this including an overall reduced number of WAM in the brain, fewer transcripts of *Spp1* and *Gpnmb* amongst an equal number of WAM, or overall increased numbers of non-WAM microglia that would effectively dilute their RNA in a

bulk sequencing approach. To test whether their number is reduced, fresh frozen slices spanning the rostrocaudal axis were prepared from *Fcgrt*$^{+/-}$ and *Fcgrt*$^{-/-}$ mice and stained for fluorescence in-situ hybridization with probes for *Fcrls* (microglia marker) and *Spp1* (Figure 26J). Images were taken of all areas populated by *Spp1*$^{+}$ WAM, namely the corpus callosum and the neuroepithelium (Figure 26J, Q). *Spp1*$^{+}$ WAM were observed in significantly greater numbers in Fcgrt+/- mice compared to Fcgrt-/- (Figure 26K-X, *Fcgrt*$^{+/-}$ mean ± SEM: 1 ± 0.03, *Fcgrt*$^{-/-}$ 0.67 ± 0.09, n=5 *Fcgrt*$^{+/-}$, n=4 *Fcgrt*$^{-/-}$, p = 0.0067). In sum, these findings suggest that there are fewer *Spp1*$^{+}$ WAM in the brain in absence of maternal IgG postnatally.

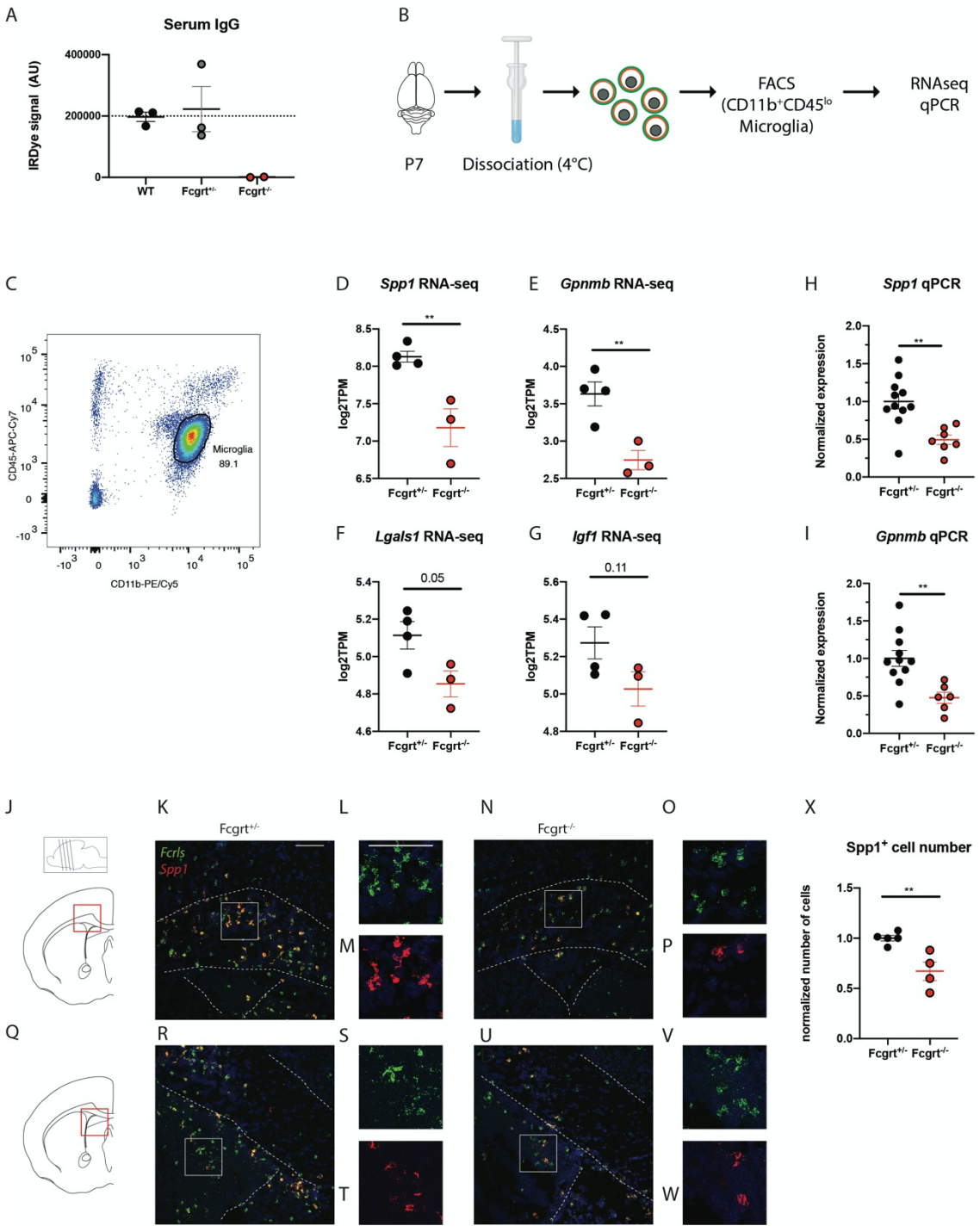

Figure 26 Mice Lacking Maternal IgG Postnatally Harbor Fewer Spp1^{+} Axon-Tract-Associated Microglia

A Scatter plot of IRDye signal quantified from IgG immunoblot of serum samples from WT, Fcgrt$^{+/-}$ and Fcgrt$^{-/-}$ pups at P7. **B** Schematic of the experimental paradigm to freshly isolate microglia for RNA sequencing and qPCR without artificially activating them. **C** Representative pseudo-color flow cytometry plot showing microglia gate (single cell, live, CD11b^{+}, CD45$^{int/lo}$). **D-G** Scatter plots of normalized gene counts from RNA sequencing experiment. *Spp1*

p=0.0087, *Gpnmb* **p=0.01, *Lgals1* p=0.05, *Igf1* p=0.11, n=4 $Fcgrt^{+/-}$ and n=3 $Fcgrt^{-/-}$. **H-I Scatter plots of normalized gene expression from qPCR experiment. *Spp1* **p=0.0016, *Gpnmb* **p=0.0042, n=11 $Fcgrt^{+/-}$ and n=7 $Fcgrt^{-/-}$. **J** Schematic of the anatomic region centered on the cingulum for confocal imaging at P7. **K-P** Representative confocal micrographs of fluorescence in-situ hybridization for *Spp1* and *Fcrls* (microglia marker) in $Fcgrt^{+/-}$ and $Fcgrt^{-/-}$ animals. **Q** Schematic of the anatomic region centered on the neuroepithelium for confocal imaging at P7. **R-W** Representative confocal micrographs of fluorescence in-situ hybridization for *Spp1* and *Fcrls* (microglia marker) in $Fcgrt^{+/-}$ and $Fcgrt^{-/-}$ animals. **X** Scatter plots of normalized $Spp1^{+}$ cell counts) in $Fcgrt^{+/-}$ and $Fcgrt^{-/-}$ animals. *Spp1* **p=0.0067, n=5 $Fcgrt^{+/-}$ and n=4 $Fcgrt^{-/-}$.

4.4 Discussion

This study addresses the role of IgG and microglial Fc receptors in white-matter development. I show that maternally-derived IgG binds to microglia in the developing brain and that mice lacking this molecule display reduced numbers of myelinating oligodendrocytes and lower myelin protein expression in the spinal cord. Further, I find subtle abnormalities in axonal morphology in the corpus callosum of IgG-deficient mice. Seeking to address whether the effects of IgG and similar effects reported for the role of *Fcer1g*, the mandatory subunit of its canonical Fc receptors, are mediated by microglia rather than cell autonomously through OPCs, I reveal that *Fcer1g* is expressed by microglia in the brain, but not OPCs. I leverage CRISPR/Cas to generate a conditional Fcer1g loxP (Fx) allele und show that the Fx allele is expressed normally and that crossing with a microglia Cre line removes *Fcer1g* expression from the brain. Surprisingly, I demonstrate that the abnormalities in myelin seen in IgG-deficient mice are neither present in the microglia-specific *Fcer1g* knockout mice, nor the previously published constitutive *Fcer1g* knockout mice, pointing to a non-canonical mechanism of IgG distinct from signaling through Fc receptors. Additional studies using depletion of all microglia subsets using two different CSF1R-antagonist paradigms yielded mixed results. Finally, transcriptional analysis of isolated microglia from mice lacking maternal IgG reveal an underrepresentation of *Spp1* and *Gpnmb* transcripts, which constitute the core signature of white-matter associated microglia, suggesting that IgG mediates more subtle shifts in microglia polarization.

The brain is traditionally viewed as an immune privileged site where IgG or other serum proteins are excluded by the blood-brain barrier (Muldoon et al., 2013). In my experiments, I find that immunoreactivity in western blots corresponding to the molecular weight of IgG can be detected in brain lysates from early postnatal, but not adult mice (Figure 15). This signal appears

to peak around 7 days postnatally and studies using immunodeficient mice demonstrate that while independent of the immune status of the pup, it depends on the immune status of the dam (Figure 15). Interestingly, much of it seems to be passed on during early postnatal development as shown by the cross-fostering experiment, further strengthening the conclusion that this molecule is maternally derived. In addition to its source, my studies address the molecular identity of the signal given that a host of proteins undergoes maternofetal transfer and could hence give rise to the immunostaining signal (Gitlin and Koch, 1968). My complimentary studies using *Fcgrt*-deficient mice born to *Fcgrt* heterozygous mice shed light on this. *Fcgrt* encodes FCRN, the neonatal Fc receptor required for serum half-life and maternofetal IgG transport. While *Fcgrt* heterozygous dams express this protein and are thus able to transfer IgG across the decidua basalis in the placenta and into the milk, pups deficient in *Fcgrt* lack the protein on the chorion side of the placenta and in their intestine, rendering them unable to take up maternal IgG (Roopenian and Akilesh, 2007). Both immunoblotting and immunofluorescence staining show that the signal is absent in Fcgrt-deficient pups, which bolster the conclusion that the molecule is indeed IgG (Figure 15). An important caveat to these studies is the question as to whether IgG leakage into the brain could represent an experimental artifact from manipulation of the tissue. Initial studies show that the signal is independent of perfusion pressure, and present in fresh-frozen tissues that did not undergo perfusion. This strongly suggests that the signal is not a perfusion artifact. A second question concerns the antigenic specificity of the IgG molecules. In this study, investigation into the functional significance of the antibodies was prioritized, but future studies should examine which target proteins in the brain, if any, the antibodies bind to.

IgG occurs in the brain and binds to microglia, especially in the developing corpus callosum, which begs the question as to what its role is. In absence of knowledge regarding the

target antigens, previous research suggested that it may signal through *Fcer1g*, a subunit of its canonical Fc receptors (Nakahara et al., 2003). Examination of the most striking phenotypes reported for *Fcer1g*-deficient mice revealed similar, albeit less severe reductions in MAG-positive myelinating oligodendrocytes at postnatal day 10 (Figure 16). In addition, OLIG2-expressing cells of the oligodendroglia lineage were reduced. This indicates that not merely the maturation, but rather the proliferation and survival of OLIG2-positive cells is affected by the presence of IgG postnatally, similar to what has been observed for Shh (Ravanelli and Appel, 2015). In experiments examining bulk protein expression, immunoblots of spinal cord lysate revealed reduced expression of several myelin proteins at postnatal day 7 (Figure 16). The spinal cord is a suitable tissue to measure and extrapolate myelin protein at this age due to the low expression in the brain, however, further studies are warranted using brain lysate at different adolescent ages.

My studies using electron microscopy to test whether postnatal IgG affects the corpus callosum and myelin ultrastructure reveal that the myelin sheath morphology is independent of IgG (Figure 17). This was surprising, given that mice lacking the IgG receptor subunit *Fcer1g* display severe hypomyelination with 50% fewer axons myelinated and thinner sheaths compared to control animals (Nakahara et al., 2003). One explanation for this discrepancy could be that IgG signals through Fc receptors that do not incorporate *Fcer1g*, for instance the inhibitory FcRIIb (Nimmerjahn and Ravetch, 2008). Another explanation could be that other non-IgG receptors that also incorporate *Fcer1g* underlie the hypomyelination phenotype, such as OSCAR, TREM, PIR-A, Dectin-2, and IL-3R (Brandsma et al., 2016). These receptors are mostly expressed in peripheral immune cells and further studies could elucidate their contribution to this pathology. A third explanation is that the effect observed by Nakahara and coworkers may have been artifactual, given that they could not be reproduced (Figure 23). Interestingly, while I did not observe

hypomyelination in mice lacking IgG postnatally, I found reduced axon sizes and increased axonal density due to an overall shift in axon calibers toward smaller calibers compared to control animals (Figure 17). This more subtle phenotype is reminiscent of observations MAG-deficient mice that display smaller axon calibers (Yin et al., 1998). Here, it is interesting to speculate that the reduced expression of MAG (Figure 16) may underlie the changes in axon caliber (Figure 17). With respect to its functional relevance, it is interesting to note that reduced calibers have been observed in autistic individuals where they were correlated with abnormal development of interhemispheric connections (Wegiel et al., 2018).

Experiments to define the cellular specificity of *Fcer1g* expression and to create an *Fcer1g* conditional knockout mouse confirm expression in microglia and the creation of the allele (Figures 18-21). Nakahara and coworkers found that *Fcer1g* was required for myelination and attributed the effect to OPCs based on immunohistochemistry and OPC tissue culture results (Nakahara et al., 2003). At the same time, the results were at odds with studies using bulk or single-cell RNA sequencing showing microglia as the sole expressor in the brain parenchyma (Zhang et al., 2014; Marques et al., 2016; Li et al., 2019). The discrepancy for this may be explained by methodological limitations, such as microglia contamination of the OPC culture, which appears likely given the experimental protocol used (Nakahara et al., 2003). My findings from sorted OPCs and microglia, as well as FISH and immunofluorescence staining clearly rule out expression in OPCs and highlight microglia as the sole expressors in the parenchyma (Figure 18-20). Generation of an *Fcer1g* loxP (Fx) allele was confirmed using multiple methodologies and this mouse line will be made available publicly via Jackson Laboratories to facilitate further functional studies of *Fcer1g*. In this study, I use the *Tie2-Cre* line that displays Cre activity in microglia but not OPCs to show

that *Fcer1g* can be completely ablated in the corpus callosum (Figure 21), further supporting the conclusion that *Fcer1g* is expressed by these cells only.

Functional studies examining myelinating oligodendrocytes, myelin protein, and myelin ultrastructure indicate that neither microglial *Fcer1g*, nor *Fcer1g* in other cell types is required for normal myelin development (Figures 21-23). While the finding that microglial *Fcer1g* does not play a role in myelination is novel, the findings in the constitutive *Fcer1g* knockout mice are at odds with a report by Nakahara and coworkers (Nakahara et al., 2003). One explanation for this discrepancy could be differences in the genetic background. Nakahara and colleagues used C57BL/6 without specifying whether the mice were from Jackson Laboratories, Taconic, or an entirely different source while C57BL/6N mice from Taconic were used for the studies reported here.

My studies seeking to confirm the requirement of microglia for normal myelination yield mixed results. First, in confirmation of previously published results (Hagemeyer et al., 2017), experiments using the CSF1R inhibitor BLZ945 to ablate microglia postnatally indicated that myelin protein expression was reduced in absence of microglia (Figure 24). However, a complimentary set of studies using the more recently developed and more specific CSF1R inhibitor PLX5622 (Spangenberg et al., 2019) did not reveal a hypomyelination phenotype when analyzed by immunoblotting and immunofluorescence staining (Figure 25). In fact, mice treated with PLX5622 displayed increased numbers of PGFRa positive OPCs compared to controls at postnatal day 8 (Figure 25). For these studies, it is of note that BLZ945-treated mice were markedly smaller than their littermates, whereas PLX5622-treated mice developed normally (Figure 25U-V). This suggests that the BLZ945-associated phenotype might, at least in part, be due to a general developmental delay or other mechanisms. While such mechanisms remain to be explored, the

data argue against Hagemeyer's conclusion that all microglia subsets are collectively required for postnatal myelination. Rather, BLZ945 may, at higher concentrations, bind directly to PDGFRa on OPCs and thus inhibit their viability directly (Liu et al., 2019b). In line with this, recently developed mice lacking microglia by virtue of CSF1R enhancer deletion (*CSF1R*$^{\Delta FIRE}$) display normal myelin in a gross analysis (Rojo et al., 2019). The conflicting results observed in these studies despite complete microglia depletion using either paradigm highlight the challenges of using such models and indicate that future studies into the role of microglia in myelination may benefit from more refined approaches.

Lastly, RNA sequencing studies on microglia sorted from mice lacking IgG postnatally show that several transcripts associated with the white matter-associated subset of microglia and that the number of microglia expressing these genes are reduced in absence of IgG compared to controls (Figure 26). This is intriguing considering studies suggesting that this particular subset plays a role in myelin development through means of growth factor secretion (Wlodarczyk et al., 2017). Further, this subset of cells is highly transient with occurrence only in the developing white matter tracts (Wlodarczyk et al., 2014, 2017; Hammond et al., 2019; Li et al., 2019), which aligns with the temporal occurrence profile of IgG postnatally (Figure 15). Thus, IgG could potentially be a signal to induce this subset of microglia or to bias developing microglia towards the WAM subset, similar to what has been reported for SIRPa in adulthood (Sato-Hashimoto et al., 2019). Differential activity of this subset may in turn lead to subtle changes in white-matter architecture (Figure 17). Together, the findings suggest a model in which maternal IgG enters the brain postnatally, where it binds to microglia and shifts their polarization toward the *Spp1*$^{+}$/*Gpnmb*$^{+}$ white-matter subtype. This shift in polarization translates to subtle changes in axon tract morphology. Mechanistically, the action of IgG follows a non-canonical pathway, independent of

Fc receptors. Future studies may examine functional consequences of these alterations on electrophysiological activity and behavior and test whether reconstitution with exogenous IgG can rescue the observed abnormalities.

Conclusions, Limitations, and Future Directions

Development of Improved Tools to Visualize and Manipulate Microglia

In Chapters 1 and 2, I presented evidence for the generation of three improved transgenic mouse lines for the visualization and manipulation of microglia, namely *Tmem119-P2A-EGFP*, *Tmem119-P2A-CreERT2*, and *Fcrls-P2A-Cre*. All three lines displayed highly efficient targeting and improved characteristics over existing tools, especially with respect to distinguishing microglia from border-associated macrophages and monocytes.

There were three main limitations in these studies. First, all lines were only tested in healthy animals rather than in a disease context that might result in the downregulation of gene expression from the targeted loci (Masuda et al., 2020). This is primarily a concern for the *Tmem119* transgenic lines, since *Fcrls* expression is not affected by disease (Hammond et al., 2019). One way to address this concern in the *Tmem119-P2A-EGFP* and *Tmem119-P2A-CreERT2* models would be to examine EGFP or tdTomato expression in experimentally induced facial nerve damage, white-matter damage through administration of cuprizone, crossing to the 5xFAD mouse model, or optic nerve crush. In the case of the *Tmem119-P2A-CreERT2* model, it would be particularly interesting to examine recombination efficiency in microglia by administering tamoxifen after onset of disease, given that this would be relevant when testing effects of therapeutic candidate gene deletion on the disease trajectory.

Secondly, the *Tmem119-P2A-CreERT2* and *Fcrls-P2A-Cre* lines were tested only with the Ai14-tdTomato reporter. This reporter is more sensitive than some others such as the R26-YFP reporter (Masuda et al., 2020). Hence, there is a possibility that the prediction for the level of Cre recombinase activity for an average floxed allele of interest would be overestimated based on the recombination efficiency for the Ai14 floxed allele. While an investigator should always determine

the efficiency of recombination for the floxed allele at hand, one way to address this issue would be to cross the mice to at least two to three different reporter alleles of different sensitivities and systematically assess efficiency and specificity. In this regard, a good future direction would be to systematically compare the most promising available lines using the same reporter alleles and experimental paradigms.

Thirdly, while BAMs were extensively examined in the *Tmem119-P2A-EGFP* and *Tmem119-P2A-CreERT2* lines, the *Fcrls-P2A-Cre* mouse was not tested in detail with respect to Cre activity in these cells. A way to address this would be to do histological analysis of border regions, including the dura, and flow cytometric analysis of single cell suspensions prepared from enzymatically digested brains.

Finally, even with the improved specificity of the *Fcrls-P2A-Cre* line that completely spares monocytes, some BAMs and peripheral macrophages still display recombinase activity. Recently, Jung and colleagues demonstrated that specificity can be tremendously improved by using a *Cx3cr1/Sall1* split-Cre approach. At the same time, the efficiency of recombination in this line was strongly diminished, presumably due to low expression level of *Sall1*, requiring breeding of multiple alleles located on different chromosomes to homozygosity. Moving forward, it would be tempting to leverage *Fcrls* and *P2ry12*, which are highly expressed microglia-specific genes on the same chromosome with non-overlapping ectopically targeted cell subsets, to create a novel split-Cre line that could be easily bred to mice with floxed alleles of interest.

The Role of Maternal IgG in White-matter Development

In Chapter 4, we presented evidence for the requirement of maternally derived IgG in white-matter development. Our principal findings showed that IgG localized to microglia in the

developing brain and that IgG was derived from the dam. We further showed that mice lacking IgG during embryonic and postnatal development harbored fewer MAG-positive myelinating oligodendrocytes at postnatal day 10 and thinner axons at postnatal day 28. Together, these data suggest a role of maternal IgG in white-matter development. However, there are a few limitations in our study including the possibilities that (1) maternal behavior may have affected the pups' development, (2) that the *RAG2* model for maternal immunodeficiency affects other mediators that get transferred from the dam to the pup, and (3) that peripheral mechanisms may have mediated the effect of maternal IgG on the white-matter development.

First, given that we used pups born to *RAG2*-deficient females, there is a possibility that differences in maternal behavior of $RAG2^{-/-}$ mice compared to normal mice affected the pups' brain development. Immunodeficient mice display impaired social recognition memory and it has been shown that myelination in the developing pups is affected by maternal behavior (Kikusui et al., 2007; Ono et al., 2008; McGowan et al., 2011; Grier et al., 2015). A second caveat is that our studies using *RAG2*-deficient dams also deplete the pups of other B- and T-cell derived cytokines that they would have acquired from the dam. While several such cytokines are known to influence brain development adversely in the context of maternal immune activation, it is possible that others, such as TGFβ would act in a beneficial way (Penttila et al., 2003; Butovsky et al., 2014; Choi et al., 2016). Thirdly, pups acquire IgG systemically from the dams, and, while IgG localizes to microglia in the CNS white-matter, our studies do not exclude potential peripheral action of IgG that could manifest in white-matter alterations. Such peripherals effects might include IgG action on the commensal flora or neonatal infection, both of which have profound effects on peripheral immune cells and their pro-inflammatory as well as anti-inflammatory mediators that might affect the brain.

These caveats could be addressed in two possible ways. One, studies examining the number of MAG-positive oligodendrocytes at P10 and corpus callosum ultrastructure at P28 could be carried out in *Fcgrt*-deficient animals that lack the IgG importer in the placenta and the neonatal gut (Roopenian and Akilesh, 2007). Using this model, it is possible to compare littermates born to the same dam, which would allow to rule out confounding effects of maternal behavior. Similarly, since FcRn (the protein encoded by *Fcgrt*) only imports IgG but not cytokines, potential confounding effects from depletion of these maternally derived mediators could be excluded. Two, rescue studies could be designed using IgG-deficient pups (born to immunodeficient mothers) that were implanted with miniosmotic pumps to deliver IgG to the brain directly (Hammond et al., 2014). Using this approach, pups born to the same dam could be used, thus excluding potentially confounding effects of maternal care. This paradigm could reveal whether IgG is sufficient to restore normal white-matter development, which would rule out the possibilities that maternal cytokines or peripheral effects contributed to the phenotype.

Another outstanding question in our studies is whether the observed white-matter phenotypes might be transient or permanent in nature. In absence of maternal IgG, fewer MAG-positive myelinating oligodendrocytes were observed at P10 and thinner axons at P28. These data suggest that the impairment spans at least a significant period during postnatal development. At the same time, abnormalities in early myelin development are frequently compensated for later, as is often observed in studies of myelination. Therefore, future experiments should examine whether the number of myelinating oligodendrocytes remains reduced at later timepoints in mice that lacked IgG postnatally. Further, electron microscopic studies in animals older than P28 would clarify whether the axonal phenotype is persistent or transient. By extension, additional analysis

should also examine axonal morphology at younger ages to shed light on when this phenotype arises.

The Role of White-matter-associated Microglia in Myelin Development

In the final subchapters of Chapter 4, we presented evidence suggesting that microglia were not clearly required for myelination. Specifically, our studies using PLX5622 to deplete microglia during postnatal development achieved close to 100% depletion of microglia in the cortex and approximately 90% depletion in the corpus callosum. These mice, however, displayed normal numbers of myelinating oligodendrocytes at P10 and normal myelin protein expression at P21. Also in this chapter, we demonstrated that a unique subpopulation of microglia located in the white-matter was dysregulated in absence of maternal IgG. These studies have a few limitations, most notably, that the microglia depletion paradigm failed to achieve 100% depletion in the corpus callosum, and that the identity of the drug-resistant microglia remained unknown. It is possible that microglia evading the depletion paradigm belong to the unique subset of white-matter-associated microglia that was recently identified and implicated in myelination (Wlodarczyk et al., 2017; Hammond et al., 2019; Li et al., 2019). While speculative at this point, their resistance to the depletion approach is reminiscent of their resistance to other ablation strategies using diphteria toxin (Wlodarczyk et al., 2017). Moving forward, it will be important to address the identity and relevance of this PLX5622-resistant population. This could be achieved in several ways including fluorescence in-situ hybridization for candidate transcripts such as *Spp1* and *Gpnmb* or FACS isolation of the cells and scRNA sequencing in mice that were treated with PLX5622. Finally, to achieve more complete depletion of microglia including the *Spp1*-positive subset and to test their relevance, the recently developed $Csf1r^{\Delta FIRE/\Delta FIRE}$ mouse model could be used (Rojo et al., 2019).

Materials and methods

Animal work

All animal procedures were performed in accordance with the MIT animal care committee's regulations. Mice were bred to a C57BL/6J or C57BL/6N background. For all experiments, mice of both sexes were used, and no apparent sex differences were observed. Mice were either created in-house as part of the projects (*Tmem119-EGFP, Tmem119-CreERT2, Fcrls-Cre, Fcer1g Fx*) or obtained from external sources. *Ai14(RCL-tdT)-D* (Stock #007914), *RAG2 KO (*Stock #008449*), Tie2-Cre aka B6.Cg-Tg(Tek-cre)1Ywa/J (*Stock #008863*), Fcgrt KO aka B6.129X1-Fcgrttm1Dcr/DcrJ* (Stock #003982*)* were obtained from JAX. *Fcer1g KO* (Model 583) was obtained from Taconic. *Cx3cr1-CreM* was generated by IVF using C57BL/6N oocytes and sperm from MMRRC (036395-UCD).

Generation of transgenic animals using CRISPR/Cas9

To generate *Tmem119* knock-in mice, donor DNA templates encoding ribosome-skipping peptide *porcine teschovirus-1 polyprotein* and *EGFP* (*P2A-EGFP*) or *CreERT2* (*P2A-CreERT2*) were synthesized. These sequences were flanked by sequences of 55-300 bp for EGFP and 1.5 kb for CreERT2 homologous to 5' and 3' regions around the *Tmem119* stop codon. These templates were injected into fertilized mouse oocytes together with a single crRNA (AGUCUCCCCCAGUGUCUAAC, Synthego) that cuts at the stop codon.

Tmem119 knock-in donor DNA templates were generated by digesting pAAV-P2A-EGFP with XbaI and EcoRI (New England Biolabs) and inserting three gblocks (LHA, P2A-EGFP or P2A-CreERT2, RHA, purchased from IDT) using Gibson cloning (HIFI assembly mix, New England Biolabs) according to the manufacturers protocol. Resulting plasmids were purified and

sequenced. For CreERT2, the highly purified dsDNA plasmid was directly used as donor DNA in injections. For EGFP, single strand DNA (ssDNA) was produced using PCR with forward primers for left homology arms between 55 and 300 bp (5'-A*G*C*AACTGGTCCTCCTGAAA-3' and 5'-CAAAGCCTGTGAAGGGTGGG-3', respectively, * denoting phosphorothioate) and a reverse primer for a 55 bp right homology arm (5'-CAAAGAGGTGACCCTCAAGG-3', with 5' phosphorylation for lambda digest of antisense strand). Using these primers, large scale PCR with Takara PrimeStar was performed to obtain 40-60 µg of product. The PCR product was highly purified with the Qiagen PCR purification kit and subject to digestion of the antisense strand. Lambda exonuclease (New England Biolabs) was used to digest 20 µg dsDNA at 37 °C for 60 min. Complete digestion of dsDNA was confirmed by agarose gel electrophoresis and Sanger sequencing with sense- and antisense-binding primers. DNA sequences for *pAAV-P2A-EGFP, Tmem119 LHA, P2A-CreERT2, P2A-EGFP, and Tmem119-RHA* are available online (Kaiser and Feng, 2019).

Mixtures for injection of zygotes were prepared freshly on the morning of the day of injection. Briefly, water to a final volume of 100 µl was mixed with final concentrations of 10 mM TrisHcl buffer, 0.61 µM crRNA, 0.61 µM tracrRNA (sequence proprietary to Synthego) and heated to 95 °C for 5 min. Heated mixtures were cooled to room temperature for 10 min and 30 ng/µl EnGen Cas9 protein (New England Biolabs) was added. Mixtures were incubated at 37 °C for 15 min to form Cas9 to crRNA-tracrRNA complexes. Final concentrations of 5 ng/µl donor DNA (P2A-EGFP ssDNA or P2A-CreERT2 plasmid dsDNA) and 10 ng/µl recombinant RAD51 protein were added. Mixtures were kept on ice until use, when they were incubated at 37 °C for 15 min followed by centrifugation at 10.000 rpm for 1 min to prevent clogging of the micropipette.

Injection of mixtures was carried out using standardized protocols of the transgenics facility in zygotes obtained from pure C57BL/B6N mice (Taconic).

To generate *Fcrls-P2A-Cre* knock-in mice, donor DNA template encoding ribosome-skipping peptide *porcine teschovirus-1 polyprotein* and *Cre* (*P2A-Cre*) was synthesized. The sequence was flanked by sequences of 1.5 kb homologous to 5' and 3' regions around the *Fcrls* stop codon. The template was injected into fertilized mouse oocytes together with three crRNAs (UCUAGAUCUUCAGAAAGUGC, CUAGAUCUUCAGAAAGUGCU, AGACCUCCUACUUUCUGCAC, Synthego) that cut sequences flanking the stop codon.

The *Fcrls-2A-Cre* knock-in donor DNA template was generated by synthesizing the LHA, Cre, and RHA fragments using PCR (Phusion polymerase). Primers used to create the fragments are shown in Table 4 (5' to 3' orientation).

Table 4: Primers used to create the Fcrls-2A-Cre donor template

Template DNA	Primer name	Primer sequence (5' to 3')
Genomic DNA	Fcrls-LHA-F	gcggccgcacgcgtttaattaagtgtacccaaagtgcgtttggtg
Genomic DNA	Fcrls-LHA-R	acgtctccagcctgcttcagcaggctgaagttagtagcgaaagtgctgggtaagactgtg
PL450-Ires-Cre	Fcrls-2A-Cre-F	gctgaagcaggctggagacgtggaggagaaccctggacctatggccaatttactgaccgt
PL450-Ires-Cre	Fclrs-2A-Cre-R	atggtctctggtctctagatctctaatcgccatcttccagca
Genomic DNA	Fcrls-RHA-F	agatctagagaccagagaccatc
Genomic DNA	Fcrls-RHA-R	agaggttgattatcgataagcttgatatcggacgggaagatgagtgaacttac

The pAAV-P2A-EGFP plasmid was digested with XbaI and EcoRI (New England Biolabs) and the three fragments (LHA, P2A-Cre, RHA) were inserted by Gibson cloning (HiFi Assembly Mix, New England Biolabs) using the four-fragment protocol. Positive clones were isolated, DNA

prepared, and the PAM site of the 3'most sgRNA was mutated using site-directed mutagenesis. Resulting plasmids were purified and sequenced.

For *Fcrls-2A-Cre* mice, mixtures for injection of zygotes were prepared freshly on the morning of the day of injection. Briefly, water to a final volume of 100 µl was mixed with final concentrations of 10 mM TrisHcl buffer, 0.61 µM of each of the three crRNA (1.83 µM total), 2.44 µM tracrRNA (sequence proprietary to Synthego) and heated to 95 °C for 5 min. Heated mixtures were cooled to room temperature for 10 min and 30 ng/µl EnGen Cas9 protein (New England Biolabs) was added. Mixtures were incubated at 37 °C for 15 min to form Cas9 to crRNA-tracrRNA complexes. Final concentrations of 10 ng/µl donor DNA and 10 ng/µl recombinant RAD51 protein were added. Mixtures were kept on ice until use, when they were incubated at 37 °C for 15 min followed by centrifugation at 10.000 rpm for 1 min to prevent clogging of the micropipette.

Injection of mixtures was carried out using standardized protocols of the transgenics facility in zygotes obtained from pure C57BL/B6J mice (JAX).

To generate *Fcer1g loxP (Fx)* knock-in mice, a donor DNA template containing part of intron 1, exons 2 and 3, intron 2, and part of intron 3 was synthesized. LoxP sites were inserted at the guide RNA cut sites in intron 1 and intron 3 and loxP sequences were flanked by 1.5 kb homology arms. These templates were injected into fertilized mouse oocytes together with two crRNAs (CAUGUGACAUUCCUCAGUGU, UGAAAAGAGAGCUGCCGGGU, Synthego) that cut sequences in intron 1 and intron 3, flanking exon 2 and 3.

The *Fcer1g-loxP* knock-in donor DNA template was generated by creating five fragments for Golden Gate assembly using PCR (Phusion polymerase) to create the fragments and BbsI to

insert the fragments into pAAV-hSyn-EGFP. Primers used to create the fragments are shown in Table 5. The DNA sequences for the custom loxP gblocks are as follows.

Custom 5' loxP gblock (loxP in lower case):

AGTGAACTCCAATGGGTCCTTGAGGTAGACCAAGTGCTCAATGATGCCAGAGGAAC
CACAATACTGAAAAGAGAGCTGCCGataacttcgtatagcatacattatacgaagttatGGTGGGTAGAG
AGGGAAGTCTATAGTAAACCTAAGTCCTAGTACAG

Custom 3' loxP gblock (loxP in lower case):

TGGTCCTAAAATCTAATTGAAGCCATGTGACATTCCTCAGataacttcgtatagcatacattatacgaa
gttatTGTGGGCTTAGAACTCCCCAGACAAGGTCAAAAAGGGAAAACCCCTGCTAACA
AAGGGAGTCTCCCACGTTGC

Table 5: Primers used to create the Fcrls-2A-Cre donor template

Template DNA	Primer ID	5' to 3' sequence
Genomic DNA	Insert #1 FWD	cccaaagaagacgtttccggtctgtgccaccatgcc
Genomic DNA	Insert #1 REV	cccaaagaagacgttggcatcattgagcacttggtc
Custom 5' loxP gblock (IDT)	Insert #2 FWD	cccaaagaagacaggccagaggaaccacaatact
Custom 5' loxP gblock (IDT)	Insert #2 REV	cccaaagaagacagtgctgtactaggacttaggtttact
Genomic DNA	Insert #3 FWD	cccaaagaagacacagcagaaccctccatgcttc
Genomic DNA	Insert #3 REV	cccaaagaagacaccactgaggaatgtcacatggc
Custom 3' loxP gblock (IDT)	Insert #4 FWD	cccaaagaagacgaagtggtcctaaaatctaattgaagc
Custom 3' loxP gblock (IDT)	Insert #4 REV	cccaaagaagacgatcaacgtgggagactccct
Genomic DNA	Insert #5 FWD	cccaaagaagactcttgaccaagtccagaggctat
Genomic DNA	Insert #5 REV	cccaaagaagactccaggcttccactaggatattgtcacg

The pAAV-P2A-EGFP plasmid was mixed with purified PCR products and assembled via Golden Gate cloning (BbsI enzyme, New England Biolabs). Bacteria were transformed and grown out overnight. Positive clones were isolated, DNA purified and sequenced.

For *Fcer1g loxP (Fx)* mice, mixtures for injection of zygotes were prepared freshly on the morning of the day of injection. Briefly, water to a final volume of 100 µl was mixed with final concentrations of 10 mM TrisHcl buffer, 0.61 µM of each of the two crRNA (1.22 µM total), 1.63 µM tracrRNA (sequence proprietary to Synthego) and heated to 95 °C for 5 min. Heated mixtures were cooled to room temperature for 10 min and 30 ng/µl EnGen Cas9 protein (New England Biolabs) was added. Mixtures were incubated at 37 °C for 15 min to form Cas9 to crRNA-tracrRNA complexes. Final concentrations of 10 ng/µl donor DNA and 10 ng/µl recombinant RAD51 protein were added. Mixtures were kept on ice until use, when they were incubated at 37 °C for 15 min followed by centrifugation at 10.000 rpm for 1 min to prevent clogging of the micropipette.

Injection of mixtures was carried out using standardized protocols of the transgenics facility in zygotes obtained from pure C57BL/B6J mice (JAX).

Genetic analysis and genotyping of *Tmem119* mice and Ai14

Founder mice were genetically examined by amplifying sequences spanning the 5' and 3' junction and including the entire inserted transgene. Specifically, high quality DNA was obtained from ear punches using a tissue DNA extraction kit according to the manufacturer's instructions (Macherey-Nagel). One amplicon spanning approximately 1.5 kb of these sequences was generated using Q5 polymerase with primers 5'ofLHA-F (GCCTCTGTCACTTAAGTTGG) and P2A-R (GCTTCAGCAGGCTGAAGTTA). A second amplicon of about 2.5-3.5 kb was generated using primers Tmem-LHA-P2A-F (CAGTGTCGGAAGCGGAGCTA) and 3'ofRHA-R (GAAAGAGGAAGCTAGAAGGG). Both amplicons were purified and then sequenced using

primers spanning the entire length using Sanger sequencing (Genewiz). Trace files were aligned to *in silico* assemblies and analyzed using Snapgene.

To genotype mice, ear tissue was prepared using an alkaline buffer (25 mM NaOH, 0.2 mM Na_2EDTA, pH=12) at 95 °C for 30 min. The lysed tissue solution was neutralized using an acidic buffer (40 mM TrisHcl, pH=5). PCR using primers WT-F GTCAGGAGGAGGCCCAGGAA, EGFP-F CTGCTGCCCGACAACCACTA, CreERT2-F ACCGCCTACATGCGCCCACT, and Common-R GTTTCCTGGGGTGCACCAGA yielded products of 400 bp for the wildtype allele and 320 bp for the EGFP or CreERT2 allele.

Ai14(RCL-tdT) mice were obtained from JAX (Stock 007914) and maintained in house. Homozygous Ai14 mice were bred to heterozygous *Tmem119-CreERT2* mice to generate offspring for the analysis. Ai14 mice were genotyped according to the protocol provided by JAX.

Genetic analysis of *Fcrls-P2A-Cre* mice

Founder mice were genetically examined by amplifying sequences spanning the 5' and 3' junction and including the entire inserted transgene. Specifically, high quality DNA was obtained from ear punches using a tissue DNA extraction kit according to the manufacturer's instructions (Macherey-Nagel). Amplicons spanning these sequences were generated using Phusion polymerase using primers for a 5' fragment (ggagctgcttaagagtatgcac, ggcaaattttggtgtacggtc), and a 3' fragment (gtcatgaactatatccgtaacctgg, tctggtagtacatcatactgattaagac) that are unique to the knock-in allele. PCR products were purified and sequenced for positive founders. For genotyping of mice from F1 and later generations, a simplified protocol was employed using three primers (agacgatttgggatggtttg, tggctggaccaatgtaaatattg, acagctgaagtctggaagtc) that yield a wildtype band of 284 bp and a Cre band of 194 bp.

Genetic analysis of *Fcer1g Fx* mice

Founder mice were genetically examined by amplifying sequences spanning the 5' and 3' junction and including the entire inserted transgene. Specifically, high quality DNA was obtained from ear punches using a tissue DNA extraction kit according to the manufacturer's instructions (Macherey-Nagel). Amplicons spanning sequences unique to the knock-in were generated using Phusion polymerase using primers for a 5' fragment (TGAAACTCCCTATTTAGCTGAG, GGAGTGGGACAGGAAGCATG) and a 3' fragment (CCTTGGTTTCCTGGTCCTCC, GTTCTGCTGTACTAGGACTT). PCR was purified and sequenced to verify correct knock-in. For examination of exon 1 to exon 5, a separate PCR was run (GCTCCTTTTGGTGGAACAAGCAG and CTCTCTAAGGCCCTTCTTGCTCC), yielding a 5.4 kb product. For genotyping of mice from F1 and later generations, a simplified PCR protocol was devised using three primers (TGTGACATTCCTCAGTGGTCCTAAAATC, CATGTGACATTCCTCAGTGTGGG, and CTCACCATTTTCCTTCCTACCCAG) that result in a 379 bp product for the loxP allele and a 308 bp product for the wildtype allele.

RNA isolation and quantitative PCR (qPCR)

For *Tmem119* knock-in mice, brain hemispheres from adult *Tmem119-EGFP*$^{+/-}$ mice were dissected and snap-frozen in liquid nitrogen. Highly pure RNA was isolated using an RNeasy purification kit (Qiagen) following the manufacturer's instructions. Equal amounts of RNA (1.5 µg per sample) were reverse transcribed using an iScript Advanced cDNA synthesis kit (Bio-Rad). Resulting cDNA was diluted 1:50 in ultrapure water. qPCR was carried out using SsOAdvanced Universal SYBR Green Supermix (Bio-Rad) on a CFX96 realtime system. Primers used were

exon-spanning whenever possible and of the following sequences: Tmem119-F CCTTCACCCAGAGCTGGTTC, Tmem119-R GGCTACATCCTCCAGGAAGG, GAPDH-F GCCTTCCGTGTTCCTACC, GAPDH-R CCTCAGTGTAGCCCAAGATG, b-actin-F CTAAGGCCAACCGTGAAAAG, b-actin-R ACCAGAGGCATACAGGGACA. Differential gene expression analysis was performed using built-in software for the Bio-Rad CFX96 realtime system.

For microglia and OPCs, 50.000 cells were sorted directly into 350 µl RLT Plus buffer containing 143 mM 2-Mercaptoethanol. RNA was isolated using the RNeasy Micro kit (Qiagen) according to the manufacturers specifications resulting in 12-13 µl RNA at 1-2 ng/µl. RNA (exactly 2 ng) was reverse transcribed using the iScript Advanced low input kit (Bio-Rad). cDNA was diluted 1:6 in nuclease free water. qPCR was run with 0.25 µM of each primer and 5 µl of diluted cDNA as input using the SsOAdvanced Universal SYBR Green Supermix (Bio-Rad) on a CFX96 realtime system. Primer sequences are shown in Table 6.

Table 6:

Fcer1g-qF	cttaccctactctactgtcgactcaa
Fcer1g-qR	aggcccgtgtagacagcat
Lilrb4-qF	tctacacccactgaagatggac
Lilrb4-qR	ctggtatccgatgaggatgag
Lgals1-qF	ctcaaagttcggggagaggt
Lgals1-qR	cattgaagcgaggattgaagt
Lgals3-qF	cgggtggagcactaatcagg
Lgals3-qR	cggatatccttgagggtttg
Itgax-qF	agcctcaagacaggacatcg
Itgax-qR	tgaatcctggaggggatct
Gpnmb-RT-F-snap	ggaaggactcctgggaaggag
Gpnmb-RT-R-snap	cctgcagttcttctcatagacg
SPP1-RT-F	gaggaaaccagccaaggac
SPP1-RT-R	tgccagaatcagtcactttca
IGF-1Wlo-F	ccgaggggcttttacttcaacaa

IGF1-Wlo-R	cggaagcaacactcatccaca
Actin_qF	ctaaggccaaccgtgaaaag
Actin_qR	accagaggcatacagggaca
GAPDH-qF	gccttccgtgttcctacc
GAPDH-qR	cctcagtgtagcccaagatg
Ywhaz-qF	cttcctgcagccagaagaat
Yhwaz-qR	ctccctgctcagtgacagact

Tamoxifen administration

Tamoxifen (Sigma, T5648) was dissolved in corn oil at 20 mg/ml under agitation for several hours in the dark and kept at room temperature for 2–3 days. Using needles from Harvard Apparatus (52-4025), separately housed adult animals were fed via oral gavage for 3 days. Needles were rinsed between days and syringes were replaced. At time of administration, the mice weighted approximately 19-26 g and received 250-400 µl of the 20 mg/ml tamoxifen solution, corresponding to 0.2 mg per g body weight. Postnatal day 2 mice weighing approximately 2 g received 5 µl of the 20 mg/ml solution, corresponding to 50 µg per g body weight per day for three consecutive days. The health of the mice was monitored daily. At least 7 days week after the last dose, mice were sacrificed by transcardiac perfusion.

Immunofluorescence staining and imaging

Adult mice were deeply anesthetized and perfused with 25 ml phosphate buffered saline (PBS) followed by 25 ml 4% paraformaldehyde (PFA) in PBS. Early postnatal mice (P3) were perfused with 8 ml PBS and 8 ml PFA. Brains were surgically removed and postfixed in the fixative at 4 °C for 24 h. Fixed brain were washed in PBS once and sliced into 100 µm-thick sagittal slices using a Leica VT1000S. Slices were washed twice in PBS, permeabilized in 1.2%

TX100 in PBS for 15 min, washed twice in PBS, and subject to incubation in blocking solution (5% normal goat serum, 2% bovine serum albumin, 0.2% TX100 in PBS). Blocked sections were incubated with primary antibodies for IBA1 (1:500, Synaptic Systems, 234006), GFP (1:1000, Invitrogen, A11122, 1:500, Aves Labs, GFP-1020), TMEM119 (1:1000, Abcam, ab209064), Olig2 (1:1000, Millipore, AB9610), NeuN (1:1000, Millipore, MAB377), GFAP (1:1000, Sigma, G9269), MBP (1:1000, AB5864), OLIG2 (1:1000, AB9610; Millipore and 1:1000, ABE1024, Millipore), APC/CC1 (1:500; catalog no. OP80; Calbiochem), FCER1G (1:1000, 06-727, Millipore), CNP (1:2000, 35504, Synaptic Systems), IgG (31188, Thermofisher), MAG (9043S, Cell Signaling Technologies), or CD163 (1:200, Abcam, ab182422, antigen retrieval required) for 24 h at 4 °C. Primary antibody incubation was followed by three washes in PBS and incubation with species-matched and Alexa fluorophore-conjugated secondary antibodies raised in goat (Invitrogen, 1:1000) for 2 h. DAPI (1:10.000) was included in a washing step or secondary antibody incubation. Slices were washed three times in PBS and mounted and coverslipped using vectashield H-1000 mounting medium.

For immunostaining of CD163, an antigen retrieval step was included. Briefly, vibratome slices were washed twice in PBS, incubated in a retrieval buffer (10 mM Sodium citrate, pH 8.5) for 5 min, followed by incubation in the retrieval buffer at 80 °C for 30 min. Sections were cooled to room temperature and washed twice in PBS. Blocking and immunostaining were then carried out as described above.

For imaging, slides were scanned on an Olympus Fluoview FV1000 fixed stage confocal microscope (high power magnifications) or Olympus BX61 epifluorescence microscope (sagittal section montage) using built-in software. For co-expression analysis in the *Tmem119-EGFP* line,

maximum projections of 4 z-stacks from three 20X high-power fields (approximately 100 cells per region) were counted manually.

For microglia morphology analysis, z-stacks were acquired at 20X magnification with 2X digital zoom and 1.2 μm step size. Images were imported as stacks into Neurolucida software. Cell bodies in the middle of the stacks with complete process arbors were selected and manually traced. Raw trace files were imported into Neurolucida explorer software and convex hull area, number of processes and total process length were determined using the convex hull analysis and branched structure analysis functions. Rendered traces were exported as monochrome vector graphics. Cell body areas were separately determined in FIJI using the polygon tool.

For studies of protein expression in embryonic brain, timed matings were set up by pairing Fcrls-Cre male mice with Ai14 female mice. Males were removed the morning after the mating was set up, which was considered day 0.5. Females were examined for pregnancy twelve days later and pregnant Ai14 females were euthanized. Uteri and embryos were dissected in ice-cold HBSS and embryos were fixed by immersion in 4% PFA overnight. Embryos were embedded in 2% Agarose and sliced at 100 μm using a Leica VT1000S. Slices were washed twice in PBS and stained against IBA1 as described above.

For studies of protein expression in peripheral organs, postnatal day 7 mice were perfused with PBS and 4% PFA and organs were harvested and postfixed in 4% PFA overnight. Organs were cryopreserved in 30% sucrose PBS, embedded in OCT, sliced at 20 μm, and stained on-slide in analogy to the protocol described for free-floating slices above.

Cell suspension preparation

Microglia and blood monocytes for single cell suspensions for flow cytometry were prepared as follows. Mice were deeply anesthetized with isofluorane and transcardially perfused with ice-cold HBSS. During perfusion, for adult mice, 2 ml of whole blood was collected from the right atrium into tubes containing 40 µl of 10% (w/v) EDTA. The 2 ml of whole blood were added to 40 ml of red blood cell lysis buffer (Abcam, ab204733) and incubated for 10 min at room temperature to lyse red blood cells. The suspension containing lysed RBCs and white blood cells was spun down at 300 g for 5 min at 4 °C, resuspended in 10 ml ice-cold HBSS, and pelleted again at 300 g for 5 min at 4 °C. WBCs were resuspended in 500 µl ice-cold FACS buffer (HBSS, 0.5% BSA, 1 mM EDTA) and subject to staining. In parallel with the WBC enrichment, brains were rapidly dissected into 2 ml ice-cold HBSS and cerebella and brainstem were removed. Brains were minced into small pieces and transferred to a dounce-homogenizer containing 5 ml ice-cold HBSS with 20 µg/ml DNase I (Worthington, DPRF, LS006343). Tissue chunks were homogenized with 7 loose and 15 tight strokes (for adult mice: 15 loose and 15 tight strokes) and the homogenate was transferred to a 50 ml falcon tube through a pre-wet 70 µm strainer. The strainer was rinsed with HBSS to top off the volume of each sample to 10 ml. Filtered homogenates were transferred to 15 ml falcon tubes and spun at 300 g for 5 min at 4 °C. For adult mice, supernatants were carefully removed, and pellets resuspended in 10 ml of ice-cold 40% Percoll in HBSS. Samples were spun at 500 g for 30 min at 4 °C with full acceleration and deceleration. Myelin and debris from the supernatant were carefully removed and pellets resuspended in 10 ml ice-cold HBSS. Following another spin at 300 g for 5 min at 4 °C, the supernatant was removed and the microglial pellet resuspended in 1 ml FACS buffer (0.5% BSA HBSS, 1 mM EDTA). For neonatal mice, Percoll centrifugation was not performed and washed cell pellets used directly.

For *Fcer1g* expression analysis in microglia and OPCs, cells were purified from postnatal day 8 mice using gentleMACS™ Octo Dissociator with Heaters (Miltinyi Biotec), gentleMACS™ C Tubes, and the Neural Tissue Dissociation Kit (P) following the manufacturer's protocol for isolating OPCs.

Staining for flow cytometry

Suspensions of white blood cells and microglia were transferred to 2 ml Eppendorf microcentrifuge tubes, and a small fraction of sample was removed for single-color controls. To stain dead cells, live/dead violet (1:500 to 1:1000, Thermofisher, L34955) was added and incubated for 5 min on ice. Tubes with live/dead-stained cells were topped off to 2 ml with FACS buffer (0.5% BSA HBSS, 1 mM EDTA) and spun down at 300 g for 5 min at 4 °C. Pellets were resuspended and incubated with 1:200 Mouse Fc Block (BD, 2.4G2, 553142) on ice for 15 min. Samples were incubated with 1:200 rat anti CD45-APC/Cy7 (Biolegend, 103115) and rat anti Cd11b-PE/Cy5 (Biolegend, 101209) at 4 °C. Tubes were topped off to 2 ml with ice-cold FACS buffer and microglia pelleted at 300 g for 5 min at 4 °C. Supernatants were removed and microglia resuspended in 500 µl. Resuspended microglia were filtered through corning strainer polystyrene tubes (Corning, 352235). Flow cytometry data was acquired on Aria II, Fortessa HTS, LSRII HTS, and Sony Symphony, and analyzed using Flowjo.

For microglia and OPC analysis, microglia were stained with Ly6G/GR1-FITC, CD45-APC/eFluor780, PDGFRa-APC (135907, Biolegend), CD11b-PE (101207, Biolegend), and DAPI for live/dead staining. Cells were sorted on Aria II (BD).

For white blood cell analysis in *Fcrls-P2A-Cre* mice, cells isolated as described above and stained with primary antibodies. Antibodies were chosen as previously reported (Masuda et al.,

2020) and directed against CD11b (M1/70, BioLegend), CD45 (30-F11, ThermoFisher Scientific), Ly6C (AL-21, BD Biosciences), Ly6G (1A8, BD Biosciences), CD115 (AFS98, ThermoFisher Scientific), CD11c (N418, ThermoFisher Scientific), MHC class II (M5/114.15.2, ThermoFisher Scientific), CD3e (eBio500A2, ThermoFisher Scientific) for 45 min at 4 °C. After washing, cells were washed and resuspended in buffer containing 3% BSA.

Protein expression analysis using immunoblotting

Immunoblotting was used for IgG detection in developing brains and myelin protein expression analysis. For IgG expression and myelin protein analysis in the brain, mice were deeply anesthetized and perfused with ice-cold PBS. Brains were dissected, split along the midline and clipped at the cerebellum to obtain hemispheres and cerebella, which were snap frozen in liquid nitrogen. Frozen hemispheres and cerebella were dounced in RIPA buffer (including Roche complete protease inhibitor) using a 5 ml tissue grinder (Wheaton# 358005) and power homogenizer at 900 rpm for 30-40 strokes. Homogenates were briefly sonicated (10% power, 10 pulses, 30% ON-70% OFF) and split into several tubes. For spinal cord samples spinal cords were dissected and snap frozen in liquid nitrogen. Snap frozen samples were supplemented with 400 µl RIPA buffer (containing protease inhibitors) and sonicated to homogenize (10% power, 40 pulses, 30% ON-70% OFF). Both for brain and spinal cord samples, separate homogenate tubes for each sample were mixed with equal amounts of 2x Laemmli buffer with or without 2-Mercaptoethanol. Samples with 2-Mercaptoethanol were boiled at 95 °C for 5 min and cooled to room temperature. Samples without 2-Mercaptoethanol were incubated at room temperature for 5 minutes. Sample volumes corresponding to about 25 µg were loaded onto 4-15% Mini-PROTEAN TGX gels (Bio-Rad) and run at 100V for 10 min, followed by 200V for 40 min. The proteins were then transferred

onto Whatman Protran nitrocellulose membranes (0.2 μm pore size, BA83, Sigma-Aldrich) using a tank blot system (Mini Trans-Blot Cell, Bio-Rad) at 100 V at 4 °C for 60 min. The membranes were blocked with 5% dry milk PBS for 1 h. Subsequently, the membranes were incubated with primary antibodies for MBP (1:1000, AB5864), CNP (1:2000, 35504, Synaptic Systems), IgG (31188, Thermofisher), MAG (9043S, Cell Signaling Technologies), GAPDH (1:1000, 6C5, Santa Cruz), PSD95 (ab18258, Abcam), beta-actin (A5441, Sigma), or PLP (E9V1N, Cell Signaling), diluted in blocking buffer at 4 °C overnight. Following primary antibody incubation, the membranes were washed three times for 5 min per wash using TBST buffer (0.05 % Tween-20). Secondary antibodies including goat-anti-mouse IRDye680 (Li-COR Biosciences), donkey-anti-rabbit IRDye 800CW (Li-COR Biosciences) or goat-anti-rat IRDye 800CW (Li-COR Biosciences), diluted in 1:1 TBST (0.05 % Tween-20): Odyssey Blocking Buffer (Li-COR Biosciences) were incubated with the membrane for 2 h at room temperature. Following three rounds of washing with TBST, the membranes were scanned using an Odyssey CLx infrared imaging system (Li- COR Biosciences). Specific bands were then quantified with the contrast-independent, automatic background subtraction rectangular ROI tool of the built-in Software Image Studio 3.1 (Li-COR Biosciences) and normalized to a beta-actin or GAPDH loading control for each lane and each blot. The values obtained were normalized to control expression.

Fluorescence in-situ hybridization using RNAscope

For in-situ study of transcript expression in studies of Fcer1g cell-type specific expression and numbers of Spp1-expressing microglia, RNAscope was used (ACD) following the manufacturers protocol. Briefly, postnatal day 7 mice were deeply anesthetized and decapitated. Brains were dissected, dry-blotted with a kim wipe, moved through OCT to achieve tight coating

and immersed in OCT-containing peel-away tissue molds. Tissue molds were placed in a bath of dry ice and isopentane until the blocks were completely frozen. Frozen blocks were stored at -80 °C until cryo-sectioning. Prior to sectioning, brains were equilibrated to -12 °C to −16 °C in a cryostat for 30 to 60 min. Brains were coronally sectioned at 16 µm using the cryostat and mounted onto 4 serial Superfrost Plus slides (25 x 75 mm, Fisherbrand) covering the corpus callosum (64 µm between slices on a slide, 2-3 slides per brain). Slides were air-dried in an open box on dry ice at prior to storage at −80 °C. The ACD RNAscope kit standard protocol was amended such that protease digestion was with Protease Plus:PBS (1:1) for 30 min at room temperature. Probes for *Spp1* (435191-C2), *Fcrls* (441231), *Gpnmb* (489511-C3), *Olig2* (447091-C3), and *Fcer1g* (414721-C2) were from ACD. To detect axon-tract associated microglia and count Spp1-positive cells, the AMP-ALT-A combination of fluorophores was used. For analysis of *Spp1*-expressing microglia, all slices on a given slide (containing 8 slice) were stained. With the experimenter blinded, 5 consecutive slices containing a representative region of 320 µm, representing 2.79 mm to 2.91 mm in the postnatal mouse brain atlas, were imaged. Images were taken such that all cells in the corpus callosum and neuroepithelium are captured. Images were counted with the experimenter blinded and the number of *Spp1*-positive cells summed up for each animal for this comparable representative region.

MyelTracer Code Accessibility

The code/software described in the paper is freely available online at https://github.com/HarrisonAllen/MyelTracer . The code is available as Extended Data.

MyelTracer Software development

Outline extraction of axons is performed using an implementation of OpenCV in Python. The processing is done as follows: First, the color space of the image is converted from RGB to grayscale, so that all pixels have a scalar magnitude between 0 and 255.

cvtColor(src, COLOR_BGR2GRAY)

Then, a bilateral filter is applied to the source image to reduce noise and smooth edges.

bilateralFilter(src, d=9, sigmaColor=75, sigmaSpace=75)

A binary thresholding filter converts pixel values below the user defined threshold, *t*, to black, and those above *t* to white.

threshold(src, thresh=t, maxval=255, type=THRESH_BINARY)

Lines drawn by the user are then applied to the thresholded image using the *polylines* function.

Contours are extracted as the boundaries between the black and white pixels of the thresholded image.

findContours(src, mode=RETR_TREE, method=CHAIN_APPROX_SIMPLE)

Contours with fewer than five vertices are filtered out using the *len* function as well as contours that don't fall within the user-defined area constraints, *Min Size* and *Max Size*, calculated using the *contourArea* function.

Once selected, contours for each feature—axon, inner myelin sheath, and outer myelin sheath—are grouped together by checking if the features nest within one another using *pointPolygonTest*.

Exported data are written in a plain-text csv document for compatibility with most spreadsheet softwares. The exported features are organized by the order in which the user selected the axon feature. Area is calculated using *contourArea*, perimeter is calculated using *arcLength*, diameter is calculated using $2 \cdot \sqrt{area/\pi}$, and *g*-ratio is calculated using $\sqrt{innerMyelinArea/OuterMyelinArea}$.

The extraction software is wrapped in a custom-designed *PyQt5* GUI, and both Windows and MacOS installers are generated using the *fman Build System* (fbs). MyelTracer has been tested and proven to work on Windows 10 and MacOS Catalina 10.15.

Quantification of *g*-ratio

To compare manually quantified *g*-ratio and those quantified with MyelTracer, three images for each region of interest were analyzed manually and using MyelTracer. Each image was analyzed first with MyelTracer, which automatically numbered every quantified axon. For manual *g*-ratio quantification, the same axons were manually numbered and then traced using ImageJ. To compare the control and Gtf2i-knockout group, raw images were obtained from Barak and coworkers (Barak et al., 2019), blinded of their genotypes and quantified using MyelTracer. To test MyelTracer's ability to quantify g-ratios in remyelinating tissues, raw images of the optic nerve from control animals and animals 28 days post injury with Montelukast and Pexidartinib treatment were obtained from Wang and coworkers (Wang et al., 2020). For each experiment comparing manual tracing with MyelTracer, several micrographs were obtained from preparations

of two to three mice per anatomic region. Within these micrographs, at least 100-300 axons were analyzed depending on the anatomical region. For testing MyelTracer's capability to detect a hypomyelination phenotype in a Williams Syndrome model, several micrographs from three mice per genotype with a total of 332 and 455 axons were analyzed for control and Gtf2i fl/fl; Nex-Cre mice, respectively. For optic nerve, sciatic nerve, and corpus callosum, three different researchers recorded image quantification times. Numbers denoting measured axons in representative images were enlarged for easier visualization. MyelTracer was run on a MacBook Pro (2.8 GHz, 16 GB RAM, Intel Iris Plus Graphics 655 1536 MB and macOS Catalina Version 10.15.2.), Windows 10 (Intel Core i5-7300HQ CPU 2.50GHz, 8GB RAM, NVIDIA GeForce GTX 1050 Ti) and MacBook Air (Intel Core i5 1.3 GHz CPU, 4GB RAM, Intel HD Graphics 5000, macOS Catalina Version 10.15.2).

RNA sequencing

RNA sequencing was performed on RNA isolated from 50.000 sorted microglia per sample. RNA quality was confirmed using a Bioanalyzer 2100. High-quality full-length cDNA was generated using the ultra-low input SMARTseq v4 kit (Takara) and cDNA libraries were sequenced using HI-Seq (Illumina) with 18 samples pooled and run on two lanes (single-end). RNA-seq data was aligned and summarized using STAR version 2.5.3a (Dobin et al., 2013), RSEM version 1.3.0 (Li and Dewey, 2011), samtools/1.5 (Li et al., 2009) and the gencode version VM15 annotation of the mm10 GRCm38 primary mouse genome assembly. Sorted and indexed alignments were visualized with IGV version 2.5.0 (Robinson et al., 2011). Differential expression analysis was done with R version 3.4.4 and DESeq2 version 1.18.1 (Anders and Huber, 2010; Love et al., 2014) and differentially expressed genes were defined as those having an absolute log2

fold change greater than 1 and an adjusted p-value less than 0.05. Data parsing and clustering was done using Tibco Spotfire Analyst 7.6.1. Mouse genes were mapped to human orthologs using Mouse Genome Informatics (http://www.informatics.jax.org/) orthology report and preranked Gene Set Enrichment Analysis (Mootha et al., 2003) was done using javaGSEA version 2.3.0_beta_2 with msigDb version 6.2 (Subramanian et al., 2005) gene sets. Individual differentially expresses genes were also examined in sorted outputs from DESeq2.

Statistical analysis

Quantitative data from the qPCR, immunofluorescence, electron microscopy, and microglia morphology experiments were analyzed using GraphPad prism. Flow cytometry data was analyzed using FlowJo.

References

Aguzzi A, Zhu C (2017) Microglia in prion diseases. The Journal of clinical investigation 127:3230–3239.

Anders S, Huber W (2010) Differential expression analysis for sequence count data. Nature Precedings:1–1.

Barak B, Zhang Z, Liu Y, Nir A, Trangle SS, Ennis M, Levandowski KM, Wang D, Quast K, Boulting GL (2019) Neuronal deletion of Gtf2i, associated with Williams syndrome, causes behavioral and myelin alterations rescuable by a remyelinating drug. Nature neuroscience 22:700–708.

Beck KD, Powell-Braxtont L, Widmer H-R, Valverde J, Hefti F (1995) Igf1 gene disruption results in reduced brain size, CNS hypomyelination, and loss of hippocampal granule and striatal parvalbumin-containing neurons. Neuron 14:717–730.

Bégin S, Dupont-Therrien O, Bélanger E, Daradich A, Laffray S, De Koninck Y, Côté DC (2014) Automated method for the segmentation and morphometry of nerve fibers in large-scale CARS images of spinal cord tissue. Biomedical optics express 5:4145.

Bennett ML, Bennett FC, Liddelow SA, Ajami B, Zamanian JL, Fernhoff NB, Mulinyawe SB, Bohlen CJ, Adil A, Tucker A (2016) New tools for studying microglia in the mouse and human CNS. Proceedings of the National Academy of Sciences 113:E1738–E1746.

Brandsma AM, Hogarth PM, Nimmerjahn F, Leusen JH (2016) Clarifying the confusion between cytokine and Fc receptor “common gamma chain.” Immunity 45:225–226.

Braniste V, Al-Asmakh M, Kowal C, Anuar F, Abbaspour A, Tóth M, Korecka A, Bakocevic N, Ng LG, Kundu P (2014) The gut microbiota influences blood-brain barrier permeability in mice. Science translational medicine 6:263ra158-263ra158.

Brenner M, Johnson AB, Boespflug-Tanguy O, Rodriguez D, Goldman JE, Messing A (2001) Mutations in GFAP, encoding glial fibrillary acidic protein, are associated with Alexander disease. Nature genetics 27:117–120.

Butovsky O, Jedrychowski MP, Moore CS, Cialic R, Lanser AJ, Gabriely G, Koeglsperger T, Dake B, Wu PM, Doykan CE (2014) Identification of a unique TGF-β–dependent molecular and functional signature in microglia. Nature neuroscience 17:131–143.

Buttgereit A, Lelios I, Yu X, Vrohlings M, Krakoski NR, Gautier EL, Nishinakamura R, Becher B, Greter M (2016) Sall1 is a transcriptional regulator defining microglia identity and function. Nature immunology 17:1397–1406.

Cammer W, Norton WT (1976) Disc gel electrophoresis of myelin proteins: new observations on development of the intermediate proteins (DM-20). Brain research 109:643–648.

Chen S-K, Tvrdik P, Peden E, Cho S, Wu S, Spangrude G, Capecchi MR (2010) Hematopoietic origin of pathological grooming in Hoxb8 mutant mice. Cell 141:775–785.

Chesik D, De Keyser J, Wilczak N (2008) Insulin-like growth factor system regulates oligodendroglial cell behavior: therapeutic potential in CNS. Journal of molecular neuroscience 35:81–90.

Choi GB, Yim YS, Wong H, Kim S, Kim H, Kim SV, Hoeffer CA, Littman DR, Huh JR (2016) The maternal interleukin-17a pathway in mice promotes autism-like phenotypes in offspring. Science 351:933–939.

Clausen B, Burkhardt C, Reith W, Renkawitz R, Förster I (1999) Conditional gene targeting in macrophages and granulocytes using LysMcre mice. Transgenic research 8:265–277.

Clynes R, Ravetch JV (1995) Cytotoxic antibodies trigger inflammation through Fc receptors. Immunity 3:21–26.

Culemann S, Grüneboom A, Nicolás-Ávila JÁ, Weidner D, Lämmle KF, Rothe T, Quintana JA, Kirchner P, Krljanac B, Eberhardt M (2019) Locally renewing resident synovial macrophages provide a protective barrier for the joint. Nature 572:670–675.

Davalos D, Grutzendler J, Yang G, Kim JV, Zuo Y, Jung S, Littman DR, Dustin ML, Gan W-B (2005) ATP mediates rapid microglial response to local brain injury in vivo. Nature neuroscience 8:752–758.

De S, Van Deren D, Peden E, Hockin M, Boulet A, Titen S, Capecchi MR (2018) Two distinct ontogenies confer heterogeneity to mouse brain microglia. Development 145:dev152306.

Decimo I, Fumagalli G, Berton V, Krampera M, Bifari F (2012) Meninges: from protective membrane to stem cell niche. American journal of stem cells 1:92.

Dobin A, Davis CA, Schlesinger F, Drenkow J, Zaleski C, Jha S, Batut P, Chaisson M, Gingeras TR (2013) STAR: ultrafast universal RNA-seq aligner. Bioinformatics 29:15–21.

Duncan ID, Marik RL, Broman AT, Heidari M (2017) Thin myelin sheaths as the hallmark of remyelination persist over time and preserve axon function. Proceedings of the National Academy of Sciences 114:E9685–E9691.

Duncan ID, Radcliff AB (2016) Inherited and acquired disorders of myelin: the underlying myelin pathology. Experimental neurology 283:452–475.

Emery B (2010) Regulation of oligodendrocyte differentiation and myelination. Science 330:779–782.

Fairén A, Smith-Fernández A, Martí E, DeDiego I, De la Rosa EJ (1992) A transient immunoglobulin-like reactivity in the developing cerebral cortex of rodents. NeuroReport 3:881–884.

Ferron M, Vacher J (2005) Targeted expression of Cre recombinase in macrophages and osteoclasts in transgenic mice. Genesis 41:138–145.

Finkelman FD, Holmes J, Katona IM, Urban Jr JF, Beckmann MP, Park LS, Schooley KA, Coffman RL, Mosmann TR, Paul WE (1990) Lymphokine control of in vivo immunoglobulin isotype selection. Annual review of immunology 8:303–333.

Foran DR, Peterson AC (1992) Myelin acquisition in the central nervous system of the mouse revealed by an MBP-Lac Z transgene. Journal of Neuroscience 12:4890–4897.

Franklin RJM, ffrench-Constant C (2008) Remyelination in the CNS: from biology to therapy. Nature Reviews Neuroscience 9:839–855.

Garbern J (2007) Pelizaeus-Merzbacher disease: genetic and cellular pathogenesis. Cellular and Molecular Life Sciences 64:50–65.

Georgiades P, Ogilvy S, Duval H, Licence DR, Charnock-Jones DS, Smith SK, Print CG (2002) VavCre transgenic mice: a tool for mutagenesis in hematopoietic and endothelial lineages. genesis 34:251–256.

Geren BB, Raskind J (1953) Development of the fine structure of the myelin sheath in sciatic nerves of chick embryos. Proceedings of the National Academy of Sciences of the United States of America 39:880.

Gibson EM, Purger D, Mount CW, Goldstein AK, Lin GL, Wood LS, Inema I, Miller SE, Bieri G, Zuchero JB (2014) Neuronal activity promotes oligodendrogenesis and adaptive myelination in the mammalian brain. Science 344.

Giera S, Luo R, Ying Y, Ackerman SD, Jeong S-J, Stoveken HM, Folts CJ, Welsh CA, Tall GG, Stevens B (2018) Microglial transglutaminase-2 drives myelination and myelin repair via GPR56/ADGRG1 in oligodendrocyte precursor cells. Elife 7:e33385.

Ginhoux F, Greter M, Leboeuf M, Nandi S, See P, Gokhan S, Mehler MF, Conway SJ, Ng LG, Stanley ER (2010) Fate mapping analysis reveals that adult microglia derive from primitive macrophages. Science 330:841–845.

Gitlin D, Koch C (1968) On the mechanisms of maternofetal transfer of human albumin and γG globulin in the mouse. The Journal of clinical investigation 47:1204–1209.

Goebbels S, Oltrogge JH, Kemper R, Heilmann I, Bormuth I, Wolfer S, Wichert SP, Möbius W, Liu X, Lappe-Siefke C (2010) Elevated phosphatidylinositol 3, 4, 5-trisphosphate in glia triggers cell-autonomous membrane wrapping and myelination. Journal of Neuroscience 30:8953–8964.

Goldmann T, Wieghofer P, Jordão MJC, Prutek F, Hagemeyer N, Frenzel K, Amann L, Staszewski O, Kierdorf K, Krueger M (2016) Origin, fate and dynamics of macrophages at central nervous system interfaces. Nature immunology 17:797–805.

Goldmann T, Wieghofer P, Müller PF, Wolf Y, Varol D, Yona S, Brendecke SM, Kierdorf K, Staszewski O, Datta M (2013) A new type of microglia gene targeting shows TAK1 to be pivotal in CNS autoimmune inflammation. Nature neuroscience 16:1618–1626.

Gong S, Kus L, Heintz N (2010) Rapid bacterial artificial chromosome modification for large-scale mouse transgenesis. Nature protocols 5:1678–1696.

Grier MD, Carson RP, Lagrange AH (2015) Of mothers and myelin: Aberrant myelination phenotypes in mouse model of Angelman syndrome are dependent on maternal and dietary influences. Behavioural brain research 291:260–267.

Grüneboom A, Hawwari I, Weidner D, Culemann S, Müller S, Henneberg S, Brenzel A, Merz S, Bornemann L, Zec K (2019) A network of trans-cortical capillaries as mainstay for blood circulation in long bones. Nature metabolism 1:236–250.

Hagemeyer N, Hanft K-M, Akriditou M-A, Unger N, Park ES, Stanley ER, Staszewski O, Dimou L, Prinz M (2017) Microglia contribute to normal myelinogenesis and to oligodendrocyte progenitor maintenance during adulthood. Acta neuropathologica 134:441–458.

Haimon Z, Volaski A, Orthgiess J, Boura-Halfon S, Varol D, Shemer A, Yona S, Zuckerman B, David E, Chappell-Maor L (2018) Re-evaluating microglia expression profiles using RiboTag and cell isolation strategies. Nature immunology 19:636–644.

Hammond TR, Dufort C, Dissing-Olesen L, Giera S, Young A, Wysoker A, Walker AJ, Gergits F, Segel M, Nemesh J (2019) Single-cell RNA sequencing of microglia throughout the mouse lifespan and in the injured brain reveals complex cell-state changes. Immunity 50:253–271.

Hammond TR, Gadea A, Dupree J, Kerninon C, Nait-Oumesmar B, Aguirre A, Gallo V (2014) Astrocyte-derived endothelin-1 inhibits remyelination through notch activation. Neuron 81:588–602.

Harauz G, Boggs JM (2013) Myelin management by the 18.5-kDa and 21.5-kDa classic myelin basic protein isoforms. Journal of neurochemistry 125:334–361.

Hazama G, Yasuhara O, Morita H, Aimi Y, Tooyama I, Kimura H (2005) Mouse brain IgG-like immunoreactivity: Strain-specific occurrence in microglia and biochemical identification of IgG. Journal of Comparative Neurology 492:234–249.

Henderson AP, Barnett MH, Parratt JD, Prineas JW (2009) Multiple sclerosis: distribution of inflammatory cells in newly forming lesions. Annals of Neurology: Official Journal of the American Neurological Association and the Child Neurology Society 66:739–753.

Hirasawa T, Ohsawa K, Imai Y, Ondo Y, Akazawa C, Uchino S, Kohsaka S (2005) Visualization of microglia in living tissues using Iba1-EGFP transgenic mice. Journal of neuroscience research 81:357–362.

Holt P, Jones C (2000) The development of the immune system during pregnancy and early life. Allergy 55:688–697.

Hughes EG, Appel B (2016) The cell biology of CNS myelination. Current opinion in neurobiology 39:93–100.

Hughes EG, Orthmann-Murphy JL, Langseth AJ, Bergles DE (2018) Myelin remodeling through experience-dependent oligodendrogenesis in the adult somatosensory cortex. Nature neuroscience 21:696–706.

Innocenti G, Clarke S, Koppel H (1983) Transitory macrophages in the white matter of the developing visual cortex. II. Development and relations with axonal pathways. Developmental Brain Research 11:55–66.

Itagaki S, McGeer P, Akiyama H, Zhu S, Selkoe D (1989) Relationship of microglia and astrocytes to amyloid deposits of Alzheimer disease. Journal of neuroimmunology 24:173–182.

Janjic P, Petrovski K, Dolgoski B, Smiley J, Zdravkovski P, Pavlovski G, Jakjovski Z, Davceva N, Poposka V, Stankov A (2019) Measurement-oriented deep-learning workflow for improved segmentation of myelin and axons in high-resolution images of human cerebral white matter. Journal of neuroscience methods 326:108373.

Kaiser T, Feng G (2019) Tmem119-EGFP and Tmem119-CreERT2 transgenic mice for labeling and manipulating microglia. eneuro 6.

Keren-Shaul H, Spinrad A, Weiner A, Matcovitch-Natan O, Dvir-Szternfeld R, Ulland TK, David E, Baruch K, Lara-Astaiso D, Toth B (2017) A unique microglia type associated with restricting development of Alzheimer's disease. Cell 169:1276–1290.

Kikusui T, Kiyokawa Y, Mori Y (2007) Deprivation of mother–pup interaction by early weaning alters myelin formation in male, but not female, ICR mice. Brain research 1133:115–122.

Kim J-S, Kolesnikov M, Peled-Hajaj S, Scheyltjens I, Xia Y, Trzebanski S, Haimon Z, Shemer A, Lubart A, Van Hove H (2021) A binary Cre transgenic approach dissects microglia and CNS border-associated macrophages. Immunity 54:176–190.

Kim W-K, Alvarez X, Fisher J, Bronfin B, Westmoreland S, McLaurin J, Williams K (2006) CD163 identifies perivascular macrophages in normal and viral encephalitic brains and potential precursors to perivascular macrophages in blood. The American journal of pathology 168:822–834.

Kisanuki YY, Hammer RE, Miyazaki J, Williams SC, Richardson JA, Yanagisawa M (2001) Tie2-Cre transgenic mice: a new model for endothelial cell-lineage analysis in vivo. Developmental biology 230:230–242.

Kleinberger G, Yamanishi Y, Suárez-Calvet M, Czirr E, Lohmann E, Cuyvers E, Struyfs H, Pettkus N, Wenninger-Weinzierl A, Mazaheri F (2014) TREM2 mutations implicated in

neurodegeneration impair cell surface transport and phagocytosis. Science translational medicine 6:243ra86-243ra86.

Koppel H, Innocenti G (1983) Is there a genuine exuberancy of callosal projections in development? A quantitative electron microscopic study in the cat. Neuroscience Letters 41:33–40.

Kowal C, Athanassiou A, Chen H, Diamond B (2015) Maternal antibodies and developing blood–brain barrier. Immunologic research 63:18–25.

Krajewski KM, Lewis RA, Fuerst DR, Turansky C, Hinderer SR, Garbern J, Kamholz J, Shy ME (2000) Neurological dysfunction and axonal degeneration in Charcot–Marie–Tooth disease type 1A. Brain 123:1516–1527.

LaMantia A, Rakic P (1990) Axon overproduction and elimination in the corpus callosum of the developing rhesus monkey. Journal of Neuroscience 10:2156–2175.

Lawson LJ, Perry VH, Dri P, Gordon S (1990) Heterogeneity in the distribution and morphology of microglia in the normal adult mouse brain. Neuroscience 39:151–170.

Lee S, Varvel NH, Konerth ME, Xu G, Cardona AE, Ransohoff RM, Lamb BT (2010) CX3CR1 deficiency alters microglial activation and reduces beta-amyloid deposition in two Alzheimer's disease mouse models. The American journal of pathology 177:2549–2562.

Li B, Dewey CN (2011) RSEM: accurate transcript quantification from RNA-Seq data with or without a reference genome. BMC bioinformatics 12:1–16.

Li H, Handsaker B, Wysoker A, Fennell T, Ruan J, Homer N, Marth G, Abecasis G, Durbin R (2009) The sequence alignment/map format and SAMtools. Bioinformatics 25:2078–2079.

Li Q, Cheng Z, Zhou L, Darmanis S, Neff NF, Okamoto J, Gulati G, Bennett ML, Sun LO, Clarke LE (2019) Developmental heterogeneity of microglia and brain myeloid cells revealed by deep single-cell RNA sequencing. Neuron 101:207–223.

Liedtke W, Edelmann W, Bieri PL, Chiu F-C, Cowan NJ, Kucherlapati R, Raine CS (1996) GFAP is necessary for the integrity of CNS white matter architecture and long-term maintenance of myelination. Neuron 17:607–615.

Lin W, Popko B (2009) Endoplasmic reticulum stress in disorders of myelinating cells. Nature Neuroscience 12:379–385.

Liu X, Nemeth DP, McKim DB, Zhu L, DiSabato DJ, Berdysz O, Gorantla G, Oliver B, Witcher KG, Wang Y (2019a) Cell-type-specific interleukin 1 receptor 1 signaling in the brain regulates distinct neuroimmune activities. Immunity 50:317–333.

Liu Y, Given KS, Dickson EL, Owens GP, Macklin WB, Bennett JL (2019b) Concentration-dependent effects of CSF1R inhibitors on oligodendrocyte progenitor cells ex vivo and in vivo. Experimental neurology 318:32–41.

Love MI, Huber W, Anders S (2014) Moderated estimation of fold change and dispersion for RNA-seq data with DESeq2. Genome biology 15:1–21.

Luo J, Elwood F, Britschgi M, Villeda S, Zhang H, Ding Z, Zhu L, Alabsi H, Getachew R, Narasimhan R (2013) Colony-stimulating factor 1 receptor (CSF1R) signaling in injured neurons facilitates protection and survival. Journal of Experimental Medicine 210:157–172.

Madisen L, Zwingman TA, Sunkin SM, Oh SW, Zariwala HA, Gu H, Ng LL, Palmiter RD, Hawrylycz MJ, Jones AR (2010) A robust and high-throughput Cre reporting and characterization system for the whole mouse brain. Nature neuroscience 13:133–140.

Marques S, Zeisel A, Codeluppi S, van Bruggen D, Falcão AM, Xiao L, Li H, Häring M, Hochgerner H, Romanov RA (2016) Oligodendrocyte heterogeneity in the mouse juvenile and adult central nervous system. Science 352:1326–1329.

Mass E, Ballesteros I, Farlik M, Halbritter F, Günther P, Crozet L, Jacome-Galarza CE, Händler K, Klughammer J, Kobayashi Y (2016) Specification of tissue-resident macrophages during organogenesis. Science 353.

Masuda T, Amann L, Sankowski R, Staszewski O, Lenz M, Snaidero N, Jordão MJC, Böttcher C, Kierdorf K, Jung S (2020) Novel Hexb-based tools for studying microglia in the CNS. Nature immunology 21:802–815.

Mathisen PM, Pease S, Garvey J, Hood L, Readhead C (1993) Identification of an embryonic isoform of myelin basic protein that is expressed widely in the mouse embryo. Proceedings of the National Academy of Sciences 90:10125–10129.

Mathys H, Adaikkan C, Gao F, Young JZ, Manet E, Hemberg M, De Jager PL, Ransohoff RM, Regev A, Tsai L-H (2017) Temporal tracking of microglia activation in neurodegeneration at single-cell resolution. Cell reports 21:366–380.

Mayoral SR, Chan JR (2016) The environment rules: spatiotemporal regulation of oligodendrocyte differentiation. Current opinion in neurobiology 39:47–52.

McGowan PO, Hope TA, Meck WH, Kelsoe G, Williams CL (2011) Impaired social recognition memory in recombination activating gene 1-deficient mice. Brain Res 1383:187–195.

McKenzie IA, Ohayon D, Li H, De Faria JP, Emery B, Tohyama K, Richardson WD (2014) Motor skill learning requires active central myelination. science 346:318–322.

McKinsey GL, Lizama CO, Keown-Lang AE, Niu A, Santander N, Larpthaveesarp A, Chee E, Gonzalez FF, Arnold TD (2020) A new genetic strategy for targeting microglia in development and disease. Elife 9:e54590.

Mildner A, Huang H, Radke J, Stenzel W, Priller J (2017) P2Y12 receptor is expressed on human microglia under physiological conditions throughout development and is sensitive to neuroinflammatory diseases. Glia 65:375–387.

Miron VE, Boyd A, Zhao J-W, Yuen TJ, Ruckh JM, Shadrach JL, van Wijngaarden P, Wagers AJ, Williams A, Franklin RJ (2013) M2 microglia and macrophages drive oligodendrocyte differentiation during CNS remyelination. Nature neuroscience 16:1211–1218.

Mootha VK, Lindgren CM, Eriksson K-F, Subramanian A, Sihag S, Lehar J, Puigserver P, Carlsson E, Ridderstråle M, Laurila E (2003) PGC-1α-responsive genes involved in oxidative phosphorylation are coordinately downregulated in human diabetes. Nature genetics 34:267–273.

More HL, Chen J, Gibson E, Donelan JM, Beg MF (2011) A semi-automated method for identifying and measuring myelinated nerve fibers in scanning electron microscope images. Journal of Neuroscience Methods 201:149–158.

Morphis LG, Gitlin D (1970) Maturation of the maternofoetal transport system for human γ-globulin in the mouse. Nature 228:573–573.

Muldoon LL, Alvarez JI, Begley DJ, Boado RJ, Del Zoppo GJ, Doolittle ND, Engelhardt B, Hallenbeck JM, Lonser RR, Ohlfest JR (2013) Immunologic privilege in the central nervous system and the blood–brain barrier. Journal of Cerebral Blood Flow & Metabolism 33:13–21.

Nakahara J, Tan-Takeuchi K, Seiwa C, Gotoh M, Kaifu T, Ujike A, Inui M, Yagi T, Ogawa M, Aiso S (2003) Signaling via immunoglobulin Fc receptors induces oligodendrocyte precursor cell differentiation. Developmental cell 4:841–852.

Nave K-A (2010) Myelination and support of axonal integrity by glia. Nature 468:244–252.

Nimmerjahn F, Ravetch JV (2005) Divergent immunoglobulin g subclass activity through selective Fc receptor binding. Science 310:1510–1512.

Nimmerjahn F, Ravetch JV (2008) Fcγ receptors as regulators of immune responses. Nature Reviews Immunology 8:34–47.

Nimmerjahn F, Ravetch JV (2010) Antibody-mediated modulation of immune responses. Immunological reviews 236:265–275.

O'Loughlin E, Madore C, Lassmann H, Butovsky O (2018) Microglial phenotypes and functions in multiple sclerosis. Cold Spring Harbor perspectives in medicine 8:a028993.

Ono M, Kikusui T, Sasaki N, Ichikawa M, Mori Y, Murakami-Murofushi K (2008) Early weaning induces anxiety and precocious myelination in the anterior part of the basolateral amygdala of male Balb/c mice. Neuroscience 156:1103–1110.

Orthgiess J, Gericke M, Immig K, Schulz A, Hirrlinger J, Bechmann I, Eilers J (2016) Neurons exhibit Lyz2 promoter activity in vivo: Implications for using LysM-Cre mice in myeloid cell research. European journal of immunology 46:1529–1532.

Paloneva J, Kestilä M, Wu J, Salminen A, Böhling T, Ruotsalainen V, Hakola P, Bakker AB, Phillips JH, Pekkarinen P (2000) Loss-of-function mutations in TYROBP (DAP12) result in a presenile dementia with bone cysts. Nature genetics 25:357–361.

Paloneva J, Manninen T, Christman G, Hovanes K, Mandelin J, Adolfsson R, Bianchin M, Bird T, Miranda R, Salmaggi A (2002) Mutations in two genes encoding different subunits of a receptor signaling complex result in an identical disease phenotype. The American Journal of Human Genetics 71:656–662.

Paolicelli RC, Bolasco G, Pagani F, Maggi L, Scianni M, Panzanelli P, Giustetto M, Ferreira TA, Guiducci E, Dumas L (2011) Synaptic pruning by microglia is necessary for normal brain development. science 333:1456–1458.

Parkhurst CN, Yang G, Ninan I, Savas JN, Yates III JR, Lafaille JJ, Hempstead BL, Littman DR, Gan W-B (2013) Microglia promote learning-dependent synapse formation through brain-derived neurotrophic factor. Cell 155:1596–1609.

Penttila I, Flesch I, McCue A, Powell BC, Zhou F, Read L, Zola H (2003) Maternal milk regulation of cell infiltration and interleukin 18 in the intestine of suckling rat pups. Gut 52:1579–1586.

Perdiguero EG, Klapproth K, Schulz C, Busch K, Azzoni E, Crozet L, Garner H, Trouillet C, De Bruijn MF, Geissmann F (2015) Tissue-resident macrophages originate from yolk-sac-derived erythro-myeloid progenitors. Nature 518:547–551.

Phan BN et al. (2020) A myelin-related transcriptomic profile is shared by Pitt–Hopkins syndrome models and human autism spectrum disorder. Nature Neuroscience 23:375–385.

Plein A, Fantin A, Denti L, Pollard JW, Ruhrberg C (2018) Erythro-myeloid progenitors contribute endothelial cells to blood vessels. Nature 562:223–228.

Poliani PL, Wang Y, Fontana E, Robinette ML, Yamanishi Y, Gilfillan S, Colonna M (2015) TREM2 sustains microglial expansion during aging and response to demyelination. The Journal of clinical investigation 125:2161–2170.

Pont-Lezica L, Beumer W, Colasse S, Drexhage H, Versnel M, Bessis A (2014) Microglia shape corpus callosum axon tract fasciculation: functional impact of prenatal inflammation. European Journal of Neuroscience 39:1551–1557.

Prinz M, Priller J (2014) Microglia and brain macrophages in the molecular age: from origin to neuropsychiatric disease. Nature Reviews Neuroscience 15:300–312.

Rademakers R, Baker M, Nicholson AM, Rutherford NJ, Finch N, Soto-Ortolaza A, Lash J, Wider C, Wojtas A, DeJesus-Hernandez M (2012) Mutations in the colony stimulating factor 1 receptor (CSF1R) gene cause hereditary diffuse leukoencephalopathy with spheroids. Nature genetics 44:200–205.

Ransohoff RM (2016) How neuroinflammation contributes to neurodegeneration. Science 353:777–783.

Ravanelli AM, Appel B (2015) Motor neurons and oligodendrocytes arise from distinct cell lineages by progenitor recruitment. Genes & Development 29:2504–2515.

Ravetch JV, Bolland S (2001) Igg fc receptors. Annual review of immunology 19:275–290.

Ritzel RM, Patel AR, Grenier JM, Crapser J, Verma R, Jellison ER, McCullough LD (2015) Functional differences between microglia and monocytes after ischemic stroke. Journal of neuroinflammation 12:1–12.

Robinson JT, Thorvaldsdóttir H, Winckler W, Guttman M, Lander ES, Getz G, Mesirov JP (2011) Integrative genomics viewer. Nature biotechnology 29:24–26.

Rogers JT, Morganti JM, Bachstetter AD, Hudson CE, Peters MM, Grimmig BA, Weeber EJ, Bickford PC, Gemma C (2011) CX3CR1 deficiency leads to impairment of hippocampal cognitive function and synaptic plasticity. Journal of Neuroscience 31:16241–16250.

Rojo R et al. (2019) Deletion of a Csf1r enhancer selectively impacts CSF1R expression and development of tissue macrophage populations. Nature Communications 10:3215.

Roopenian DC, Akilesh S (2007) FcRn: the neonatal Fc receptor comes of age. Nature reviews immunology 7:715–725.

Rushton WAH (1951) A theory of the effects of fibre size in medullated nerve. J Physiol 115:101–122.

Salzer JL (2015) Schwann cell myelination. Cold Spring Harbor perspectives in biology 7:a020529.

Samokhvalov IM, Samokhvalova NI, Nishikawa S (2007) Cell tracing shows the contribution of the yolk sac to adult haematopoiesis. Nature 446:1056–1061.

Sander S, Ouvrier R, McLeod J, Nicholson G, Pollard J (2000) Clinical syndromes associated with tomacula or myelin swellings in sural nerve biopsies. Journal of Neurology, Neurosurgery & Psychiatry 68:483–488.

Sasmono RT, Oceandy D, Pollard JW, Tong W, Pavli P, Wainwright BJ, Ostrowski MC, Himes SR, Hume DA (2003) A macrophage colony-stimulating factor receptor–green fluorescent protein transgene is expressed throughout the mononuclear phagocyte system of the mouse. Blood, The Journal of the American Society of Hematology 101:1155–1163.

Satoh J, Kino Y, Asahina N, Takitani M, Miyoshi J, Ishida T, Saito Y (2016) TMEM119 marks a subset of microglia in the human brain. Neuropathology 36:39–49.

Sato-Hashimoto M et al. (2019) Microglial SIRPα regulates the emergence of CD11c+ microglia and demyelination damage in white matter Bergles DE, Zoghbi HY, Calabresi PA, Molofsky A, eds. eLife 8:e42025.

Saunders A, Macosko EZ, Wysoker A, Goldman M, Krienen FM, de Rivera H, Bien E, Baum M, Bortolin L, Wang S (2018) Molecular diversity and specializations among the cells of the adult mouse brain. Cell 174:1015–1030.

Schafer DP, Lehrman EK, Kautzman AG, Koyama R, Mardinly AR, Yamasaki R, Ransohoff RM, Greenberg ME, Barres BA, Stevens B (2012) Microglia sculpt postnatal neural circuits in an activity and complement-dependent manner. Neuron 74:691–705.

Schwab I, Nimmerjahn F (2013) Intravenous immunoglobulin therapy: how does IgG modulate the immune system? Nature Reviews Immunology 13:176–189.

Shang DS, Yang YM, Zhang H, Tian L, Jiang JS, Dong YB, Zhang K, Li B, Zhao WD, Fang WG (2016) Intracerebral GM-CSF contributes to transendothelial monocyte migration in APP/PS1 Alzheimer's disease mice. Journal of Cerebral Blood Flow & Metabolism 36:1978–1991.

Sherman DL, Brophy PJ (2005) Mechanisms of axon ensheathment and myelin growth. Nature Reviews Neuroscience 6:683–690.

Shiota C, Miura M, Mikoshiba K (1989) Developmental profile and differential localization of mRNAs of myelin proteins (MBP and PLP) in oligodendrocytes in the brain and in culture. Developmental Brain Research 45:83–94.

Sierra A, Encinas JM, Deudero JJ, Chancey JH, Enikolopov G, Overstreet-Wadiche LS, Tsirka SE, Maletic-Savatic M (2010) Microglia shape adult hippocampal neurogenesis through apoptosis-coupled phagocytosis. Cell stem cell 7:483–495.

Simons M, Trotter J (2007) Wrapping it up: the cell biology of myelination. Current opinion in neurobiology 17:533–540.

Spangenberg E, Severson PL, Hohsfield LA, Crapser J, Zhang J, Burton EA, Zhang Y, Spevak W, Lin J, Phan NY (2019) Sustained microglial depletion with CSF1R inhibitor impairs parenchymal plaque development in an Alzheimer's disease model. Nature communications 10:1–21.

Stadelmann C, Timmler S, Barrantes-Freer A, Simons M (2019) Myelin in the central nervous system: structure, function, and pathology. Physiological reviews 99:1381–1431.

Stevens B, Allen NJ, Vazquez LE, Howell GR, Christopherson KS, Nouri N, Micheva KD, Mehalow AK, Huberman AD, Stafford B (2007) The classical complement cascade mediates CNS synapse elimination. Cell 131:1164–1178.

Subramanian A, Tamayo P, Mootha VK, Mukherjee S, Ebert BL, Gillette MA, Paulovich A, Pomeroy SL, Golub TR, Lander ES (2005) Gene set enrichment analysis: a knowledge-based approach for interpreting genome-wide expression profiles. Proceedings of the National Academy of Sciences 102:15545–15550.

Sun LO, Mulinyawe SB, Collins HY, Ibrahim A, Li Q, Simon DJ, Tessier-Lavigne M, Barres BA (2018) Spatiotemporal control of CNS myelination by oligodendrocyte programmed cell death through the TFEB-PUMA axis. Cell 175:1811–1826.

Tang Y, Harrington A, Yang X, Friesel RE, Liaw L (2010) The contribution of the Tie2+ lineage to primitive and definitive hematopoietic cells. Genesis 48:563–567.

Thion MS, Ginhoux F, Garel S (2018a) Microglia and early brain development: An intimate journey. Science 362:185–189.

Thion MS, Low D, Silvin A, Chen J, Grisel P, Schulte-Schrepping J, Blecher R, Ulas T, Squarzoni P, Hoeffel G (2018b) Microbiome influences prenatal and adult microglia in a sex-specific manner. Cell 172:500–516.

Trapp BD, Nave K-A (2008) Multiple sclerosis: an immune or neurodegenerative disorder? Annu Rev Neurosci 31:247–269.

Trapp BD, Stys PK (2009) Virtual hypoxia and chronic necrosis of demyelinated axons in multiple sclerosis. The Lancet Neurology 8:280–291.

Ueno M, Fujita Y, Tanaka T, Nakamura Y, Kikuta J, Ishii M, Yamashita T (2013) Layer V cortical neurons require microglial support for survival during postnatal development. Nature neuroscience 16:543–551.

Upender M, Dunn J, Wilson S, Naegele J (1997) Immunoglobulin molecules are present in early-generated neuronal populations in the rat cerebral cortex and retina. Journal of Comparative Neurology 384:271–282.

Vanlandewijck M, He L, Mäe MA, Andrae J, Ando K, Del Gaudio F, Nahar K, Lebouvier T, Laviña B, Gouveia L (2018) A molecular atlas of cell types and zonation in the brain vasculature. Nature 554:475–480.

Vidarsson G, Dekkers G, Rispens T (2014) IgG subclasses and allotypes: from structure to effector functions. Frontiers in immunology 5:520.

Vincze A, Mázló M, Seress L, Komoly S, Ábrahám H (2008) A correlative light and electron microscopic study of postnatal myelination in the murine corpus callosum. International Journal of Developmental Neuroscience 26:575–584.

Wang J, He X, Meng H, Li Y, Dmitriev P, Tian F, Page JC, Lu QR, He Z (2020) Robust myelination of regenerated axons induced by combined manipulations of GPR17 and microglia. Neuron 108:876–886.

Wang Y, Cella M, Mallinson K, Ulrich JD, Young KL, Robinette ML, Gilfillan S, Krishnan GM, Sudhakar S, Zinselmeyer BH (2015) TREM2 lipid sensing sustains the microglial response in an Alzheimer's disease model. Cell 160:1061–1071.

Wegiel J, Kaczmarski W, Flory M, Martinez-Cerdeno V, Wisniewski T, Nowicki K, Kuchna I, Wegiel J (2018) Deficit of corpus callosum axons, reduced axon diameter and decreased area are markers of abnormal development of interhemispheric connections in autistic subjects. Acta Neuropathologica Communications 6:143.

Weiner JA, Chun J (1997) Maternally derived immunoglobulin light chain is present in the fetal mammalian CNS. Journal of Neuroscience 17:3148–3156.

Weinhard L, Di Bartolomei G, Bolasco G, Machado P, Schieber NL, Neniskyte U, Exiga M, Vadisiute A, Raggioli A, Schertel A (2018) Microglia remodel synapses by presynaptic trogocytosis and spine head filopodia induction. Nature communications 9:1–14.

Wieghofer P, Prinz M (2016) Genetic manipulation of microglia during brain development and disease. Biochimica et Biophysica Acta (BBA)-Molecular Basis of Disease 1862:299–309.

Wlodarczyk A, Holtman IR, Krueger M, Yogev N, Bruttger J, Khorooshi R, Benmamar-Badel A, de Boer-Bergsma JJ, Martin NA, Karram K (2017) A novel microglial subset plays a key role in myelinogenesis in developing brain. The EMBO journal 36:3292–3308.

Wlodarczyk A, Martin N, Owens T (2014) IGF1 producing CD11c+ microglia emerge during postnatal neurodevelopment. Journal of Neuroimmunology 275:93.

Wong K, Noubade R, Manzanillo P, Ota N, Foreman O, Hackney JA, Friedman BA, Pappu R, Scearce-Levie K, Ouyang W (2017) Mice deficient in NRROS show abnormal microglial development and neurological disorders. Nature immunology 18:633–641.

Yin X, Crawford TO, Griffin JW, Tu P, Lee VM-Y, Li C, Roder J, Trapp BD (1998) Myelin-associated glycoprotein is a myelin signal that modulates the caliber of myelinated axons. Journal of Neuroscience 18:1953–1962.

Yona S, Kim K-W, Wolf Y, Mildner A, Varol D, Breker M, Strauss-Ayali D, Viukov S, Guilliams M, Misharin A (2013) Fate mapping reveals origins and dynamics of monocytes and tissue macrophages under homeostasis. Immunity 38:79–91.

Zaimi A, Duval T, Gasecka A, Côté D, Stikov N, Cohen-Adad J (2016) AxonSeg: open source software for axon and myelin segmentation and morphometric analysis. Frontiers in neuroinformatics 10:37.

Zaimi A, Wabartha M, Herman V, Antonsanti P-L, Perone CS, Cohen-Adad J (2018) AxonDeepSeg: automatic axon and myelin segmentation from microscopy data using convolutional neural networks. Scientific reports 8:1–11.

Zhang Y, Chen K, Sloan SA, Bennett ML, Scholze AR, O'Keeffe S, Phatnani HP, Guarnieri P, Caneda C, Ruderisch N, Deng S, Liddelow SA, Zhang C, Daneman R, Maniatis T, Barres BA, Wu JQ (2014) An RNA-Sequencing Transcriptome and Splicing Database of Glia, Neurons, and Vascular Cells of the Cerebral Cortex. J Neurosci 34:11929.

Zhao C, Dong C, Frah M, Deng Y, Marie C, Zhang F, Xu L, Ma Z, Dong X, Lin Y (2018) Dual requirement of CHD8 for chromatin landscape establishment and histone methyltransferase recruitment to promote CNS myelination and repair. Developmental cell 45:753–768.

Zhao X-F, Alam MM, Liao Y, Huang T, Mathur R, Zhu X, Huang Y (2019) Targeting microglia using Cx3cr1-Cre lines: revisiting the specificity. eneuro 6.

Zonouzi M, Scafidi J, Li P, McEllin B, Edwards J, Dupree JL, Harvey L, Sun D, Hübner CA, Cull-Candy SG (2015) GABAergic regulation of cerebellar NG2 cell development is altered in perinatal white matter injury. Nature neuroscience 18:674–682.